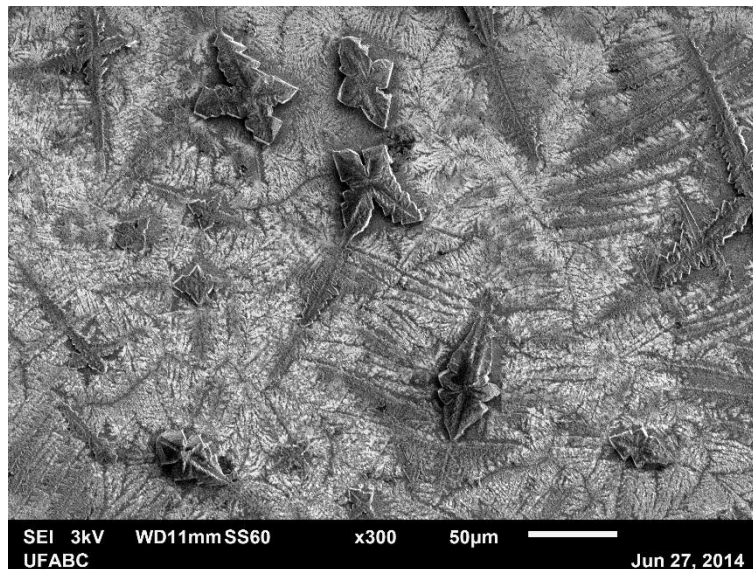


# Journal of Energy Challenges and Mechanics

ISSN 2056-9386

<http://www.nscj.co.uk/JECM/>

Volume 1, Issue 2  
October 2014



Featured article:

## **Cytochrome c as an electron acceptor of nanostructured titania and hematite semiconductors**

*Juliana C. Araújo-Chaves<sup>1</sup>, Aryane Tofanello<sup>1</sup>, César H. Yokomizo<sup>1,2</sup>, Waldemir M. Carvalho-Jr<sup>1</sup>, Flavio L. Souza<sup>1</sup> and Iseli L. Nantes<sup>1\*</sup>*

<sup>1</sup>Laboratory of Nanostructures for Biology and Advanced Materials, Centro de Ciências Naturais e Humanas, Universidade Federal do ABC, Av dos Estados, 5001, Santo André-SP, Brazil

<sup>2</sup>INFAR, Departamento de Bioquímica, Universidade Federal de São Paulo, Rua 3 de Maio, 100, São Paulo-SP, Brazil.

Journal of Energy Challenges and Mechanics, volume 1, pages 86-94.



North Sea Conference & Journal LTD  
2 Charlestown Walk, Cove Bay, AB12 3EZ, Aberdeen, Scotland, United Kingdom  
<http://www.nscj.co.uk/JECM/> | [jecm@nscj.co.uk](mailto:jecm@nscj.co.uk) | +44(0)1224 875635



TABLE OF CONTENTS

pages

ECM Series Interview: Prof. George Crabtree, Director of the Joint Center for Energy Storage Research, Argonne National Laboratory. – Dr. Henry Tan, University of Aberdeen ([video](#))

[Article 1](#): Evolution of stress–strain state in structured rock specimens under loading until failure 56-61

*V. N. Oparin, O. M. Usol'tseva<sup>\*</sup>, V. N. Semenov, and P. A. Tsoi*  
*N.A. Chinakal Institute of Mining, Siberian Branch, Russian Academy of Sciences, Krasnyi pr. 54, Novosibirsk, 630091 Russia*

[Article 2](#): The use of power DC-DC converters and gyrator structures for energy processing in photovoltaic solar facilities 62-68

*Herminio Martínez-García*  
*Barcelona College of Industrial Engineering (EUETIB), Consorci Escola Industrial de Barcelona (CEIB), Department of Electronics Department, Technical University of Catalonia (UPC) - BarcelonaTech, c/ Comte de Urgell, 187, 08036, Barcelona, Spain*

[Article 3](#): Operation of intelligent wind power unit 69-73

*Ahmed Mohamed Galal<sup>1</sup>, Toshiaki Kanemoto<sup>2\*</sup>, Kazumasa Makita<sup>3</sup> and Yusuke Taneo<sup>3</sup>*

<sup>1</sup>*Faculty of Engineering, Mansoura University, Mansoura, Egypt*

<sup>2</sup>*Faculty of Engineering, Kyushu Institute of Technology, Kitakyushu 804-8550, Japan*

<sup>3</sup>*Graduate School of Engineering, Kyushu Institute of Technology, Kitakyushu 804-8550, Japan*

[Article 4](#): Stress analysis of NPP steam generator and main factors affecting safety 74-80

*Hao Qian<sup>\*</sup>, Xingyun Liang, Kefeng Zhang, Kai Zhang, Yongcheng Xie, Xiaoyao Shen*

*Department of Component Research and Design, Shanghai Nuclear Engineering Research and Design Institute, Shanghai 200233, China*

[Article 5](#): The US shale energy boom and the price of fossil energy 81-85

*Paavo Suni*

*The Research Institute of the Finnish Economy, ETLA, Lönnrotinkatu 4 B 00120 Helsinki, Finland*



[Article 6](#): Cytochrome c as an electron acceptor of nanostructured titania and hematite semiconductors 86-94

*Juliana C. Araújo-Chaves<sup>1</sup>, Aryane Tofanello<sup>1</sup>, César H. Yokomizo<sup>1,2</sup>, Waldemir M. Carvalho-Jr<sup>1</sup>, Flavio L. Souza<sup>1</sup> and Iseli L. Nantes<sup>1\*</sup>*

<sup>1</sup>Laboratory of Nanostructures for Biology and Advanced Materials, Centro de Ciências Naturais e Humanas, Universidade Federal do ABC, Av dos Estados, 5001, Santo André-SP, Brazil

<sup>2</sup>INFAR, Departamento de Bioquímica, Universidade Federal de São Paulo, Rua 3 de Maio, 100, São Paulo-SP, Brazil.

[Article 7](#): Design and development of proton exchange membrane fuel cell using open pore cellular foam as flow plate material 95-102

*A. Baroutaji<sup>1\*</sup>, J. G. Carton<sup>1</sup>, J. Stokes<sup>1</sup>, A. G. Olabi<sup>2</sup>*

<sup>1</sup>Manufacturing and Mechanical Engineering, Dublin City University, Dublin 9, Ireland

<sup>2</sup>Faculty of Science & Technology, University of the West of Scotland, Paisley, Scotland

[Article 8](#): Strategic orientation for the ocean energy market roll-out: Coherent technology learning by system dynamics modelling of trans-organisational expert knowledge 103-112

*Ralf Bucher<sup>1\*</sup>, Ian Bryden<sup>2</sup>*

<sup>1</sup>University of Edinburgh, Institute for Energy Systems, Mayfield Road, Edinburgh, EH9 3JL, UK

<sup>2</sup>University of the Highlands and Islands, Ness Walk, Inverness, IV3 5SQ, UK



# Evolution of stress–strain state in structured rock specimens under loading until failure

## 结构化岩石样品加载失效前的应力—应变状态演变

V. N. Oparin, O. M. Usol'tseva, V. N. Semenov, and P. A. Tsoi

*N.A. Chinakal Institute of Mining, Siberian Branch, Russian Academy of Sciences, Krasnyi pr. 54, Novosibirsk, 630091 Russia*

*usoltseva57@mail.ru*

Accepted for publication on 22th July 2014

**Abstract** - The comprehensive experimental studies into the change in the stress–strain state of rock specimens subjected to uniaxial loading until failure using automated digital speckle photography analysis shows that when stress reaches 50% of the limit strength of the specimens, low-frequency micro-deformation processes begin in the specimens under slow (quasi-static) stiff loading. The amplitude of the deformation-wave processes depends on the level of the pre-set macro-loading. Wave packets are plotted for averaged microstrains obtained in sandstone and marble specimens under uniaxial compression.

In the elements of the scanned specimen surface in the region with the incipient crack, the microstrain rate amplitudes are a few times higher than in the undamaged surface region of the same specimen.

**Keywords** – Rock mass, Hierarchical block structure, Laboratory experiment, Speckle photography method, Microstrains, Deformation-wave processes.

### I. INTRODUCTION

At the current stage, nonlinear geomechanics researchers place great emphasis on quantitative description of hierarchy of blocks in structure of rock masses [1]. This is important for delineation of clusters of structural blocks in the areas of nucleation of disastrous events and characterization of kinematics and dynamics of elastic energy accumulation and relaxation in such zones [2, 3].

Discovery of pendulum waves [4–6] transferred by structural blocks of different hierarchical levels in high-stress rock masses inspired a new theoretical research trend called geomechanical thermodynamics [7]. This research trend is directly associated with interpretation of transformation mechanism of potential (elastic) energy at nucleation sites of disastrous events (earthquakes, rockbursts, coal and gas outbursts) into kinetic energy of their fractals in clusters [1].

Based on that, it becomes possible to obtain an energy estimate of threshold values of deformation in check areas of rock masses or engineer constructions, when the threshold elevation will end up with destruction events in the high stress concentration zones in rocks.

The aim of this study was to analyze distribution and development of stress–stress state in structured rock specimens subject to uniaxial loading to failure. Specific attention was paid to possible oscillating motion of structural elements of the rock specimens under constraints (pre-set stresses at the boundaries of the specimens) and the kinetic energy fractals [8].

### II. EXPERIMENTAL PROCEDURE AND MEASUREMENT EQUIPMENT

The experimental research used Instron-8802 servohydraulic testing machine for loading at the pre-set force and displacement and for the continuous recording of the load and the mobile grip displacement. Microstrains were recorded using automated digital speckle photography analyzer ALMEC-tv. The task is to interpret optical images of surface microrelief of a loaded specimen. The specimen surface is placed in the coherent radiation beam to obtain a speckle-picture. The speckles are “tight” to the corresponding points of the surface and reposition together with these points when the specimen is deformed. The displacements are recorded by frame-to-frame photography. All the parameters were recorded in real time, at frequency of 27 frames per second and spatial resolution not less than 1  $\mu\text{m}$ . The processing output is the coordinates and displacements of the specimen surface points and timing, which allows calculating strain tensor components [3].

The uniaxial stiff compression used prismatic specimens of sandstone, marble and sylvinitite, at the mobile grip displacement rate of 0.02–0.2 mm/min. Figure 1 illustrates testing of a marble specimen subjected to compression along long axis x at the grip displacement rate of 0.2 mm/min. the experiment lasted for 70 s. Ultimate strength of the specimen was 50.1 MPa, ultimate strain along x, measured by the machine cross beam unit displacement, was 0.059. Figure 2 shows the curves of the specimen stress and macrostrain and the specimen stress and time.

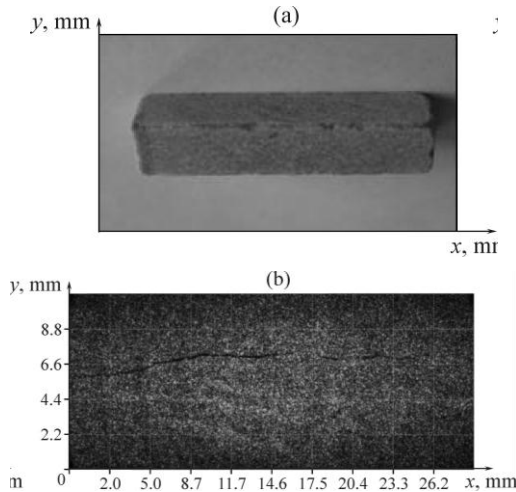


Fig. 1. (a) Marble specimen 47×11×10 mm and (b) its speckle-photography after fracture.

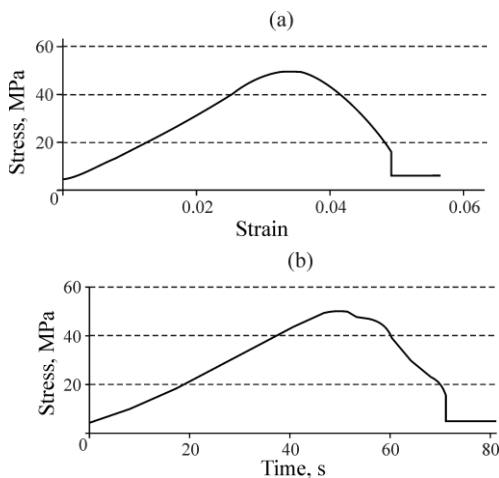


Fig. 2. (a) The curve of stresses and strain in the marble specimen in the direction of x and (b) the stress and time curve.

Concurrently with recording of microstrains on the specimen surface, measurement of vectors of microdisplacements at the surface points was carried out using ALMEC-tv. Having processed the results, we obtained a square grid of the surface displacements for the subsequent plotting of the strain tensor components.

### III. EXPERIMENTAL DATA ANALYSIS

The experimental data analysis showed nonuniformity of plastic strain, starting from the onset of the rock specimen compression. In spite of the compression being uniaxial, at the constant rate of displacement of grips, the spatial–time field of the microstrains contain both shortening and elongation areas as seen in the scans of the specimen surface.

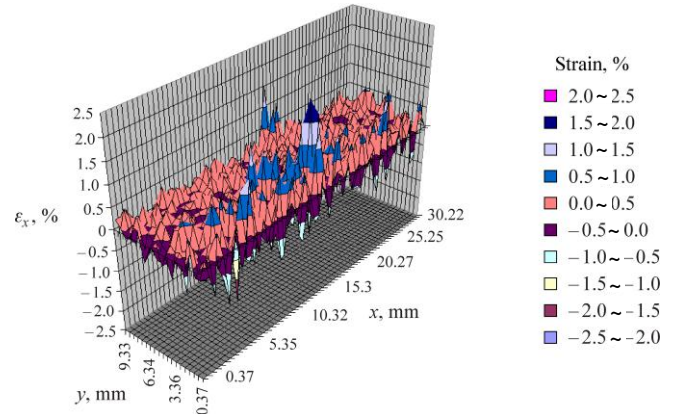


Fig. 3. Microstrains  $\epsilon_x$  of the specimen surface at the moment of 30 s in the stress–time curve in Fig. 2.

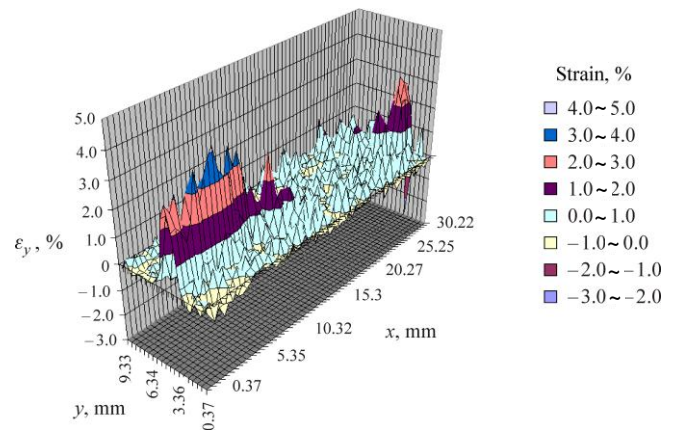


Fig. 4. Microstrains  $\epsilon_y$  of the specimen surface at the moment of 30 s in the stress–time curve in Fig. 2.

Figure 3 and 4 show 3D diagrams, where the axes x and y are the specimen surface coordinates longitudinally and crosswise, and the z axis shows the microstrains at the fit point of the scanned surface. Figures 3 and 4 not only display the sign-alternating behavior of internal microstrain of the tested rock specimens but possible causes of the deformation, largely different from that is expected in the frames of the continuum mechanics. It is seen that apparent periods of oscillating strains fit with mineralogical and structural heterogeneities of the specimens (from fractions to a few millimeters in size). The level of the recorded strain (absolute values) is comparable with the geomechanical invariant  $\mu_{\Delta}(\delta)$  [9]:

$$\mu_{\Delta}(\delta) = \frac{\delta_i}{\Delta_i} = \theta \cdot 10^{-2}, \theta \in \frac{1}{2} \sim 2, \forall i \quad (1)$$

where  $\delta_i$ —average width of joints of the structural rock-mass blocks with diameters  $\Delta_i$  ( $i$ —hierarchy level).

#### IV. STADIALITY OF MICRO- AND MACRO-DEFORMATION OF ROCK SPECIMENS UNDER UNIAXIAL LOADING UNTIL FAILURE AND LOW-FREQUENCY DEFORMATION-WAVE PROCESSES

“Stadiality” of deformation is a conventional notion, considering patterns of the rock mass stress and strain curves (e.g., Fig. 2). “Stages” are as a rule marked by “breakpoints” or noticeable change of the slope of the  $\sigma - \varepsilon$  curve branches. Is it possible to find the other, objective methods to distinguish between deformation stages, for instance, with the help of dynamic–kinematic characteristics of local deformation-wave processes?

To answer the question above, we covered the load-exposed surface with a cross-hatch of rectangles (see Fig. 5) and calculated average microstrains for them in the directions of  $x$  and  $y$  (lengthwise and crosswise the specimen, respectively). Dimensions of the rectangles were chosen so that displacements at each point and averaged displacements differed not more than by 20–25%.

Figure 6 shows a fragment of variation in the averaged micro-strain. The time dependence of the longitudinal microstrain included compression and tension–compression. In Fig. 6, microstrains fluctuate around zero. It is seen that when macro-loading of the specimen reaches 25–30% of the uniaxial compression strength, inside the specimen a complex microdeformation-wave process begins.

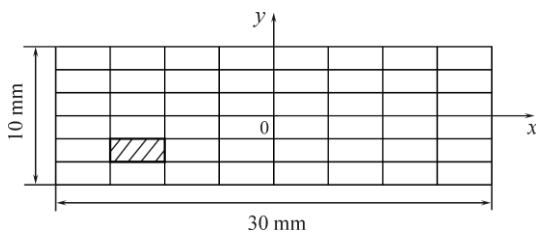


Fig. 5. Cross-hatch layout of the load-exposed surface of the test specimen: surface element (fragment) 3.5×1 mm is hatched.

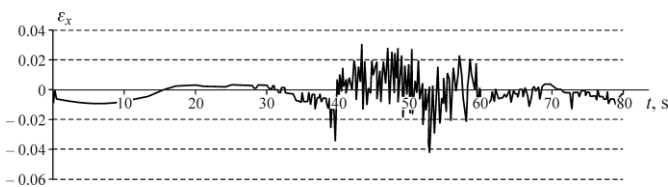


Fig. 6. Averaged microstrain  $\varepsilon_x$  of the surface element in longitudinal direction  $x$ .

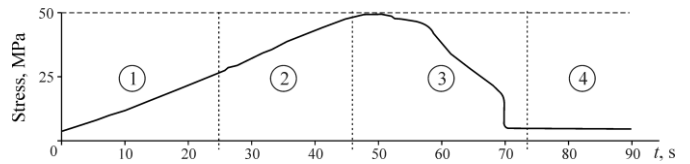


Fig. 7. “Stadiality” (stages 1–4) of the stress and loading time curve.

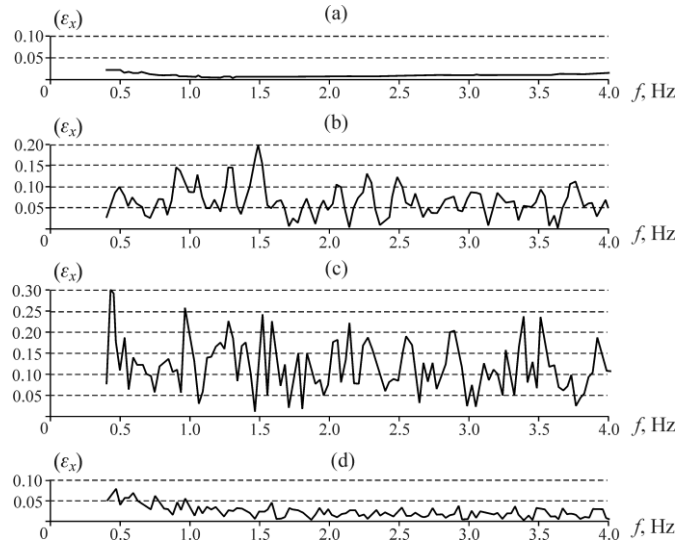


Fig. 8. Amplitude–frequency characteristic for the longitudinal microstrain  $\varepsilon_x$  by deformation stages: (a) stage 1; (b) stage 2; (c) stage 3; (d) stage 4.

The process of loading is conditionally split into four stages (Fig. 7): stage 1 and stage 2 are the load increase branch (stage 1 duration is to 0.5 of the peak load, stage 2 last up to the peak load); stage 3 is the post-peak branch; stage 4 is the residual strength branch. For each stage and for each surface element, we obtained deformation-wave packets by the averaged microstrains  $\varepsilon_x$  and  $\varepsilon_y$  and plotted the related amplitude–frequency characteristics from the Fourier transforms.

Figure 8 shows the amplitude–frequency characteristics for  $\varepsilon_x$ :

- at elastic deformation stage 1, under load under  $0.5\sigma^v$  ( $\sigma^v$ —peak load), microstrain does not fluctuate;
- at stage 2, under the load increase from  $0.5\sigma^v$  to the uniaxial compression strength of the specimen, microstrain oscillation starts, amplitudes of the oscillations grow and reach maximum values at post-peak loading stage 3;
- at residual strength stage 4, microstrain oscillation amplitudes decrease sharply (3–5 times) as against the previous two stages of deformation.

We performed checking calculation of frequencies based on the maximum values of deformation-wave amplitudes at the pre-failure and post-peak loading stages. Figure 9 shows the amplitude–frequency characteristics for the microstrain  $\varepsilon_x$  at deformation stage 2 for two different surface elements of a marble specimen. At the pre-failure stage, these frequencies

have values 0.9–1.1, 1.5, 2.3, 2.85, 3.75 Hz. The amplitude–frequency characteristics of  $\epsilon_x$  at stage 3 are shown in Fig. 10; the frequencies to correspond to the maximum amplitudes are 0.45; 1; 1.6–1.7; 2.5–2.6; 2.9; 3.2; 3.5 Hz. Comparing the frequency ranges for stage 2 (0.9–3.75 Hz) and stage 3 (0.48–3.5 Hz), it is seen that the amplitude–frequency characteristics of the deformation-wave packets displace toward the lower-frequency range at stage 3. This complies with structure of wave packets of the EME recorded at the stage of rock failure [8].

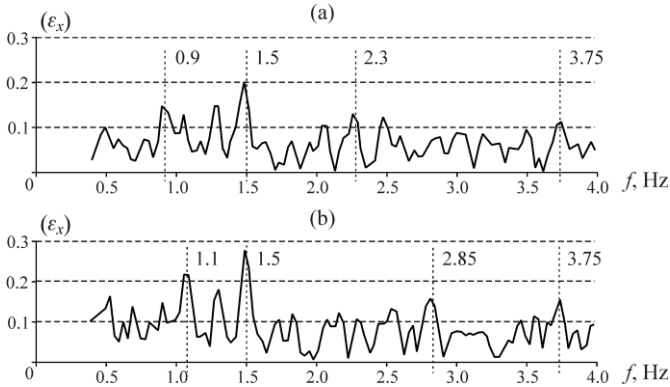


Fig. 9. Amplitude–frequency characteristics of the microstrain  $\epsilon_x$  at deformation stage 2 for different surface elements (a) and (b) of marble specimen.

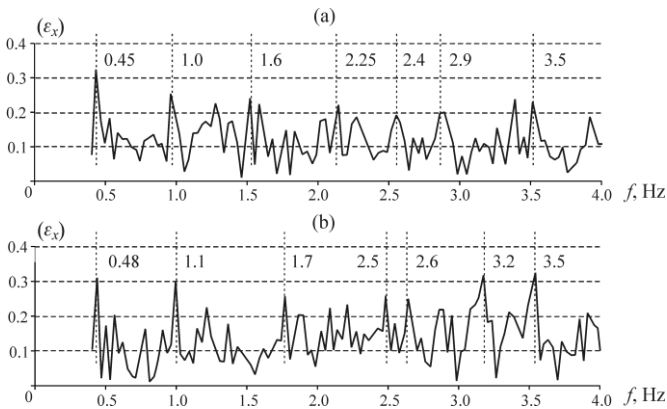


Fig. 10. Amplitude–frequency characteristics of the microstrain  $\epsilon_x$  at deformation stage 3 for different surface elements (a) and (b) of marble specimen.

**V. MICROSTRAIN RATE AT THE PRE-PEAK LOADING STAGE**

We performed comparative calculations for two different regions on the scanned surface of the test specimen: region 1 is the region where crack originated and region 2 is the undamaged material (refer to Fig. 11). Each of regions 1 and 2 was divided into 120 elements 0.5×0.5 mm in dimension. For the elements, time dependences of the transverse strain  $\epsilon_y$  were plotted. The microstrain rate estimation used approximation and smoothing of the experimental dependences  $\epsilon_y(t)$  for the mentioned

elements within time interval 0 to 40 s. The trends of the  $\epsilon_y - t$  curves were calculated as the 6th order polynomials at the approximation accuracy 0.86–0.97. The functions of microstrain rates and time,  $\epsilon'_y(t)$ , were calculated as the derivatives of the  $\epsilon_y - t$  trends.

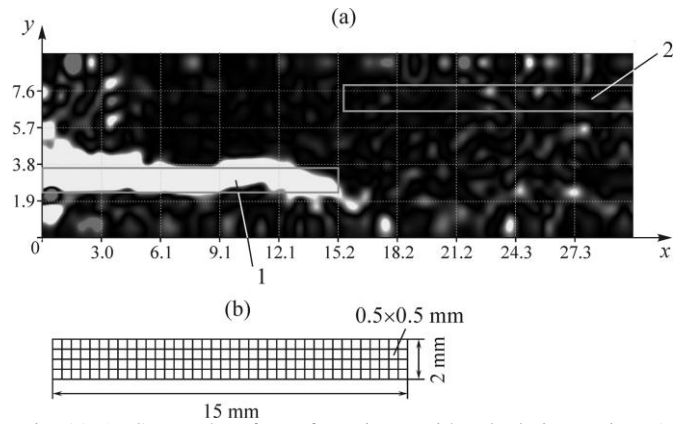


Fig. 11. (a) Scanned surface of specimen with calculation regions 1 and 2 and (b) parameters of the calculation regions.

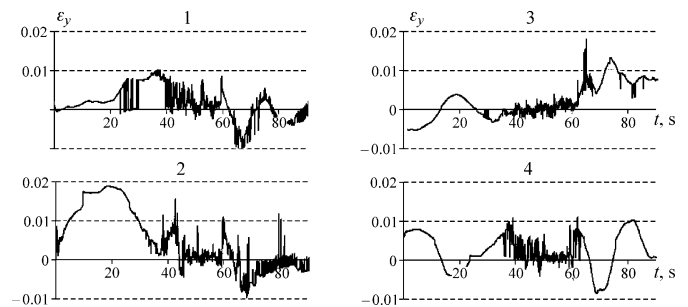


Fig. 12. Curves of the transverse microstrain  $\epsilon_y$  and time for the elements 0.5×0.5 mm in size in region 1 (where crack will originate later): 1, 2, 3, 4—arbitrary elements in the region.

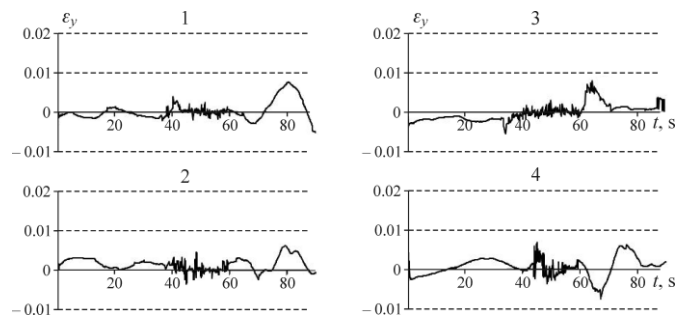


Fig. 13. Curves of the transverse microstrain  $\epsilon_y$  and time for the elements 0.5×0.5 mm in size in region 2 (undamaged).

Figures 12 and 13 show the representative curves of the transverse strains  $\epsilon_y$  and time for arbitrary elements 0.5×0.5 mm in regions 1 and 2, respectively. In Fig. 12, 13 in the interval 0–40 s (which corresponds to the load ~42 MPa or 0.83 of the peak load), there are no high-frequency oscillations of the microstrains.

Figures 14 shows the curves of the transverse microstrain rate and time for elements 1, 2, 3, 4, 0.5×0.5 mm in size in region 1, where crack originated and region 2 is the undamaged material. As follows from Fig. 14, the amplitudes of the microstrain rates are a few times higher in the elements of the region with incipient crack than in the undamaged region (regions 1 and 2, respectively). Sometimes, the rate grows under the higher loading.

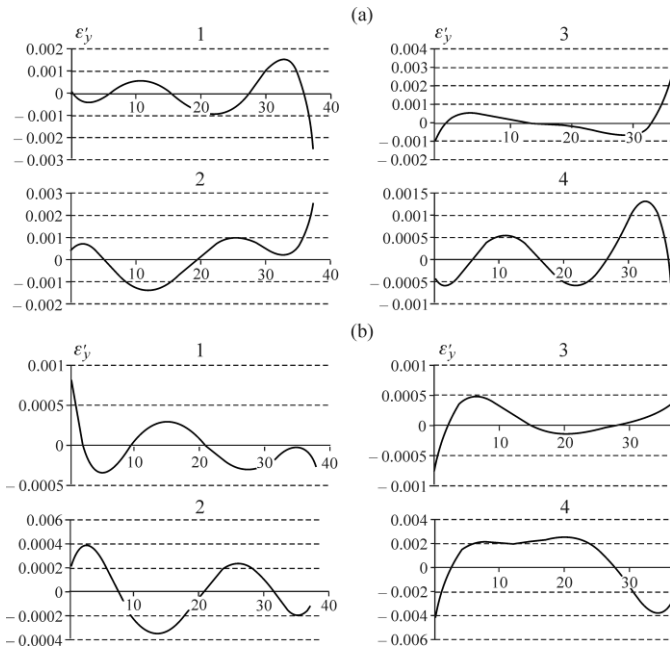


Fig. 14. The curves of the transverse microstrain rate and time for elements 1, 2, 3, 4 0.5×0.5 mm in size in (a) region 1 and (b) region 2.

## VI. CONCLUSION

The detailed studies into the micro-level stress–strain state distribution and propagation over acting faces of rock specimens subject to uniaxial loading until failure, using automated digital speckle photography analyzer ALMEC-tv, have shown that:

- under uniaxial stiff loading of prismatic sandstone, marble and sylvinitic specimens on the Instron-8802 servohydraulic testing machine at the mobile grip displacement rate 0.02–0.2 mm/min, at a certain level of stressing, low-frequency micro-deformation processes originate in the specimens due to slow (quasi-static) force;
- the amplitude of that deformation-wave processes greatly depends on the micro-loading stage:
  - at the elastic deformation stage, under the specimen stress lower than half ultimate strength of the specimen, there are no oscillations of microstrains;
  - at the nonlinearly elastic deformation stage, under stress varied from 0.5 to 1 ultimate strength of the specimens, the amplitudes of microstrains grow, including the descending stage 3; the oscillation frequency  $f = 0.5 - 4$  Hz;

—at the residual strength stage, the amplitudes of the microstrains drop abruptly (3–5 times) as against stages 2 and 3;

- in the elements of the scanned specimen surface in the region with the incipient crack, the microstrain rate amplitudes  $\epsilon'_y$  are a few times higher than in the undamaged surface region of the same specimen. Sometimes, deformation rate greatly grows with increase in the load.

In conclusion, it has been experimentally proved that under certain loading of rock specimens, the oscillations of fractals or other structural inhomogeneities begin much earlier than the ultimate uniaxial compression strength is reached. The authors think, the deformation-wave processes inside rocks and rock masses are tightly connected with the seismic and electromagnetic emissions, that are associated as well. Rock masses may be where displacement of fracture edges is “electromagnetically” connected with the pendulum deformation-wave processes [1, 8]. assessed as “capacitors” with intrinsic structural hierarchy, where displacement of fracture edges is “electromagnetically” connected with the pendulum deformation-wave processes [1, 8].

## VII. ACKNOWLEDGMENTS

The work was supported by partly the Russian Academy of Sciences, project ONZ-RAN 3.1, grant no. 12-05-01057. The equipment is kindly provided by the Shared Geomechanical, Geophysical and Geodynamic Measurement Center of the Siberian Branch of the Russian Academy of Sciences.

## REFERENCES

- [1] V.N. Oparin and A.S. Tanaino. Canonical Scale of Hierarchy Presentation in Science on Rocks (Kanonicheskaya shkala ierarkhicheskikh predstavlenii v gornom porodovedenii), Novosibirsk: Nauka, 2011.
- [2] V.N. Oparin, A.D. Sashurin, A.V. Leont'ev. Modern Geodynamics of the Outer Crust of Earth. Sources, Parameters, Impact (Sovremennaya geodinamika massiva gornykh porod verkhnei chasti litosfery: istoki, parametry, vozdeistvie na ob'ekty nedropol'zovaniya), Novosibirsk: SO RAN, 2008.
- [3] O.M. Usoltseva, L.A. Nazarova, P.A. Tsoi, L.A. Nazarov, and V.N. Semenov. “Genesis and Evolution of Discontinuities in Geomaterials: Theory and a Laboratory Experiment”, *Journal of Mining Science*, vol. 49, no. 1, pp. 1–7, 2013.
- [4] V.N. Oparin. “Scientific Discoveries in Geomechanics at the Turn of a Century and Their Application Outlook”, *Proc. Int. Conf. Geodynamics and Stress State of the Earth's Interior*, Novosibirsk: IGD SO RAN, 2008.
- [5] V.V. Adushkin and V.N. Oparin. “From the Alternating-Sign Explosion Response of Rocks to the Pendulum Waves in Stressed Geomedia. Part I”, *Journal of Mining Science*, vol. 48, no. 2, pp. 203–222, 2012.

- [6] V.V. Adushkin and V.N. Oparin. “From the Alternating-Sign Explosion Response of Rocks to the Pendulum Waves in Stressed Geomedia. Part II”, *Journal of Mining Science*, vol. 49, no. 2, pp. 175–209, 2013.
- [7] V.N. Oparin. “Pendulum Waves and “Geomechanical Temperature”, *Proc. 2nd Russia–China Conf. Nonlinear Geomechanical–Geodynamic Processes in Deep Mining*, Novosibirsk: IGD SO RAN, 2012.
- [8] V.N. Oparin, G.N. Yakovitskaya, A.G. Vostretsov, V.M. Seryakov, and A.V. Krivetsky. “Mechanical–Electromagnetic Transformations in Rocks on Failure”, *Journal of Mining Science*, vol. 49, no. 3, pp. 343–356, 2013.
- [9] M.V. Kurlenya, V.N. Oparin, and A.A. Eremenko. Relation of Linear Block Dimensions of Rock to Crack Opening in the Structural Hierarchy of Masses, *Journal of Mining Science*, vol. 29, no. 3, pp. 197–203, 1993.
- [10] V.N. Oparin A.P., Tapsiev, V.I. Vostrikov al. “On Possible Causes of Increase in Seismic Activity of Mine Fields in the Oktyabrsky and Taimyrsky Mines of the Norilsk Deposit in 2003. Part I: Seismic Regime”, *Journal of Mining Science*, vol. 40, no. 4, pp. 321–338, 2004.
- [11] Oparin, V.N., Kozyrev, A.A., Sashurin, A.D., et al. Earth Crust Destruction and Self-Organization in the Areas Exposed to Heavy Impact of Mining (Destruktsiya zemnoi kory i protsessy samoorganizatsii v oblastiakh sil'nogo tekhnogenogo vozdeistviya), Novosibirsk: SO RAN, 2012.
- [12] Kurlenya, M.V., Oparin, V.N., and Eremenko, A.A., “Mine Seismic Data Scanning Method”, *Reports of Academy of Sciences*, Vol . 333, no. 6, pp. 784–787, 1993.



# The use of power DC-DC converters and gyrator structures for energy processing in photovoltaic solar facilities

## 功率 DC-DC 转换器和回转器结构用于光伏太阳能设施中的能源加工

Herminio Martínez-García

*Barcelona College of Industrial Engineering (EUETIB), Consorci Escola Industrial de Barcelona (CEIB), Department of Electronics Department, Technical University of Catalonia (UPC) - BarcelonaTech, c/ Comte de Urgell, 187, 08036, Barcelona, Spain*

*herminio.martinez@upc.edu*

Accepted for publication on 28th August 2014

**Abstract** - This article provides a classification of high efficiency switching power-gyrator structures and their use as cells for energy processing in photovoltaic solar facilities. Having into account the properties of these topologies presented in the article, their inclusion in solar facilities allows increasing the performance of the whole installation. Thus, the design, simulation, and implementation of a *G*-type power gyrator are carried out throughout the text. In addition, in order to obtain the maximum power from the photovoltaic solar panel, a maximum power point tracking (MPPT) is mandatory in the energy processing path. Therefore, the practical implementation carried out includes a control loop of the power gyrator in order to track the aforementioned maximum power point of the photovoltaic solar panel.

**Keywords** – DC-DC power converters, Power gyrators, Photovoltaic solar panels, Maximum power point tracking (MPPT).

### I. INTRODUCTION

In general, photovoltaic subsystem –panel o module set– (generation subsystem) does not provide the same nominal voltage that the required by the output load or battery (consume subsystem). Thus, in order to “adapt” both generator and load voltages, providing at the same time *high efficiency* in this link, the use of a DC/DC power switching converter is mandatory.

As a consequence, switching converters are widely used in photovoltaic generating systems as an interface or link between, on the one hand, the photovoltaic subsystem (panel o

module set), and, on the other hand, the load and/or battery. In addition, it can allow the follow-up of the maximum power point (MPP) of the photovoltaic system in order to obtain the maximum energy that this system can provide.

Therefore, the main task of DC-DC converter in this kind of operation is to condition the energy generated by the array of panel following a specific control strategy [1]. Notice that the DC/DC conversion process implies, in turn, an associated effect of impedance transformation. In fact, the input impedance shows a dependence on a number of parameters such as load resistance, duty cycle of the switching converter, etc.

In this sense, converters are quite similar to “classic” transformers when they are used as impedance adaptors, except that in converters the adaptation parameter is not the turns ratio between the secondary and primary ones, but the duty cycle that controls the energy transfer. This duty cycle, as it is well known, can be governed electronically.

In addition to the use of the aforementioned switching power DC/DC converters, a maximum power point tracking (MPPT) is also highly recommended in the energy processing path in order to obtain the maximum power from the photovoltaic solar panel. Therefore, normally, practical implementations include a control loop of the converter in order to track the aforementioned maximum power point of the photovoltaic solar panel. This maximum power point can be achieved thanks to the control of the switching converter duty cycle. This effect, which is the basis of MPPT systems,

also shows an odd property: Certain input impedance values can be either reached or not, depending on the type of converter used, which significantly affects the performance of the photovoltaic system [1].

In DC/DC switching converters we have relation between average values of the **input and output voltages** via the duty cycle (or between average values of the input and output currents), providing, at the same time, high efficiency. Therefore, we can say that they behave as **high efficiency voltage-controlled voltage source (VCVS)**, or current-controlled current source (CCCS).

Unlike “classic” DC/DC power converters, in power gyrators we have a relation between average values of the **input voltage** and **output current** (or **input current** and **output voltage**), also providing, at the same time, high efficiency. Therefore, the key of this kind of converter is to obtain **high-efficiency voltage-controlled current source (VCCS)** or **current-controlled voltage source (CCVS)**.

The arrival of the switching semiconductor devices in the decade of the 1950s carried out the appearance of switching converters and switching power supply systems. The major development of DC-DC converters took place at the beginning of the decade of 1960s, when switching semiconductors were feasible and affordable devices, being applied in the aerospace industry as one of their first uses.

On the other hand, the initial concept of *gyrator* is referred to networks with certain interesting properties. They are attractive for the synthesis of inductive elements with properties nearer to the ideality than their counterparts of wound core. The concept of *gyrator* was introduced firstly by Tellegen in his paper ‘*The gyrator, a new electric network element*’ published in 1948 [2], in which mention is made for a network with unique properties, and was considered as a new electrical network element added to those already known.

The treatment of the subject by Tellegen is rather theoretical and does not venture into the practical design of these elements, although formally founded their behavior and some of its properties. The term ‘*gyrator*’ is, since then, used to call this kind of network, of which one of the first was introduced by the same Tellegen for a toroidal ferromagnetic core wound at one end, and separated by a dielectric segment at the other. The introduction of the gyrator circuit concept in power processing (high-efficiency switching-mode power gyrators) is due to Singer, who presented a particular gyrator in the circuits named POPI (*power output=power input*), describing the ideal behavior of a particular *switching power converter* structure [3]. In 2005 it was shown that the gyrator circuits were unstable, and calculated the stable conditions necessary for its possible implementation [4], [5].

The article is organized as follows: In Section 2 an introduction to gyrator circuits and their classification are carried out; Section 3 explains the use of power gyrators for energy processing in solar energy facilities, together with the use of a MPPT subsystem; Section 4 deals with the design and implementation of a particular power gyrator implementation for the energy processing from a photovoltaic solar panel and

its main simulation and experimental results. The article concludes with the main conclusions in Section 5.

## II. POWER GYRATOR CONCEPT

The concept of power gyrator introduced in [3] relates to a general sort of circuits named POPI, describing the ideal behavior of a switched-mode power converter. In general two big groups of power gyrators can be found: *G*-type and *R*-type gyrators.

### A. G-Type Gyrator

A power gyrator type *G* (Figure 1) is defined as a switching converter which satisfies equations (1) and with the characteristic that *the input current and output current are not pulsed*.

$$i_1 = gv_2 ; i_2 = gv_1 , \quad (1)$$

where the parameter *g* is the conductance of the gyrator. The *G*-type power gyrator with controlled output current behaves like a current source in its output port.

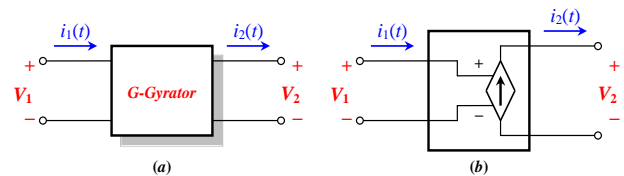


Fig. 1. *G*-type power gyrator: (a) Basic block, and (b) equivalent circuit.

The general idea of a *G*-type power gyrator is to achieve a controlled dependent current source that depends on the input voltage and a gain factor *g*. If the parameter *g* is adjustable, a VCCS (voltage-controlled output current source) can be obtained.

The two-port *G*-type power gyrators that can be found are of fourth order, that is, the buck with input filter (BIF), the boost converter with output filter (BOF), the Čuk converter and the Čuk isolated converter, as illustrated, respectively, in figure 2.

In the present work, a BIF *G*-type gyrator is used in order to validate the use of power gyrators for energy processing in photovoltaic solar facilities.

### B. BIF Gyrator

The BIF *G*-type gyrator is a DC/DC switching converter, in particular a buck regulator with input filter. The BIF structure depicted in Figure 2 is an unstable system; therefore, its implementation may not be viable. In [5] it is demonstrated the need of including a damping network to get the system to reach stability and how to calculate it. The proposed circuit, including the proposed stability network, is shown in Figure 3.

The analysis of the BIF *G*-type gyrator controlled by means of a sliding control loop shows that the system must meet a series of inequalities or conditions to obtain the necessary stability of the circuit; in particular [5], [6]:

$$R_d C_d < \frac{C_1 + C_d}{g^2 R} \tag{2}$$

$$R_d C_d > g^2 R L_1 \tag{3}$$

$$g^2 R R_d^2 C_d^2 + g^2 R L_1 (C_1 + C_d) < (g^4 R^2 L_1 + C_d) R_d D_d \tag{4}$$

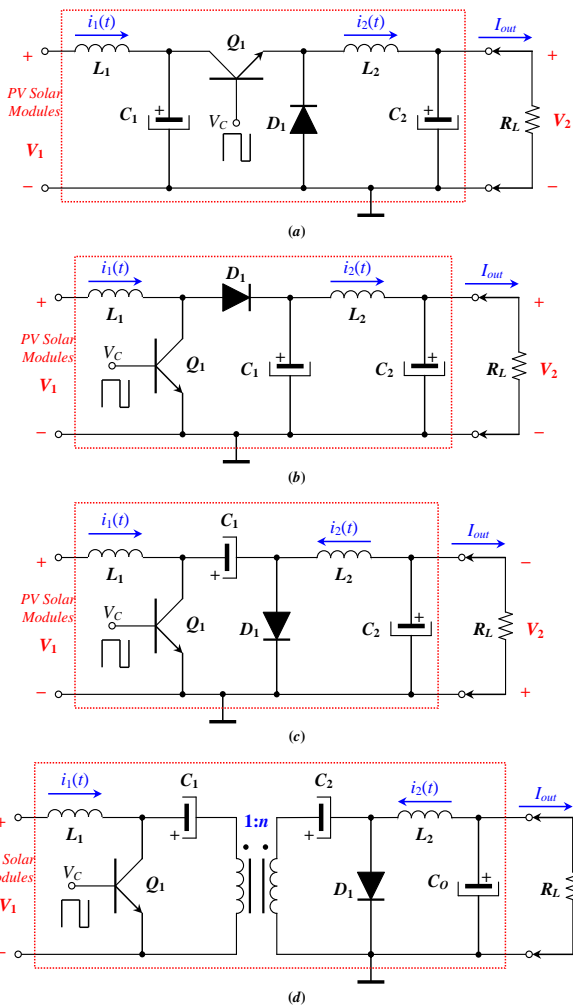


Fig. 2. Classification of *G*-type power gyrators: (a) Buck with input filter (BIF), (b) boost with output filter (BOF), (c) Ćuk converter, and (d) Ćuk isolated.

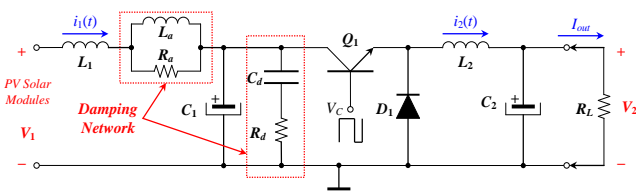


Fig. 3. Buck with input filter (BIF) gyrator with damping network.

C. R-Type Gyrator

A power *R*-type gyrator is defined as a switching converter with a switch topology characterized by (5):

$$v_1 = r i_2 ; v_2 = r i_1 , \tag{5}$$

where *r* is the resistance implemented by the gyrator.

The simpler *R*-type power gyrators are shown in Figure 4. These converters are the boost with output filter (BOF) converter, the Ćuk converter, and Ćuk converter with galvanic isolation.

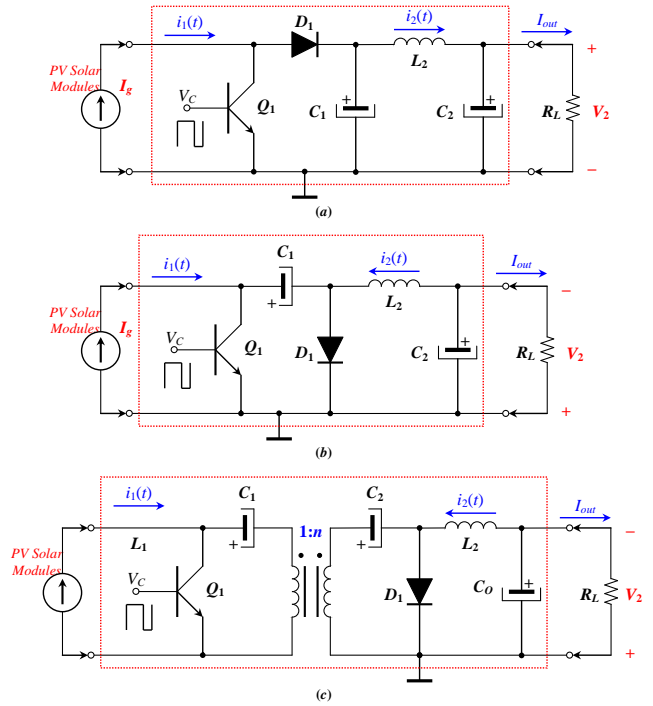


Fig. 4. Classification of *R*-type gyrators: (a) Boost with output filter (BOF), (b) Ćuk converter, and (c) Ćuk isolated.

From these different structures, the more used is the first one (the BOF converter).

III. POWER GYRATOR FOR THE ENERGY ACQUISITION OF A PHOTOVOLTAIC PANEL

In this section, in order to demonstrate the feasibility of developing power gyrator structures for solar energy applications, the design and implementation of a BIF *G*-type power gyrator are carried out. The objective is to process the energy provided by a photovoltaic panel. The panel used for the implementation of the application is supplied by the company BP. This is a panel that consists of 36 high-efficiency photovoltaic polycrystalline cells, providing a maximum power of 10 W, an open circuit voltage (*V<sub>OC</sub>*) of 21 V, and a short-circuit current (*I<sub>SC</sub>*) of 0.65 A. Regarding the battery, that acts as the output load, it must be noted that the typical value of series resistance is 0.11 Ω. This, together with the panel, will establish the design specifications of the implemented power gyrator. The initial design specifications are presented in Table I.

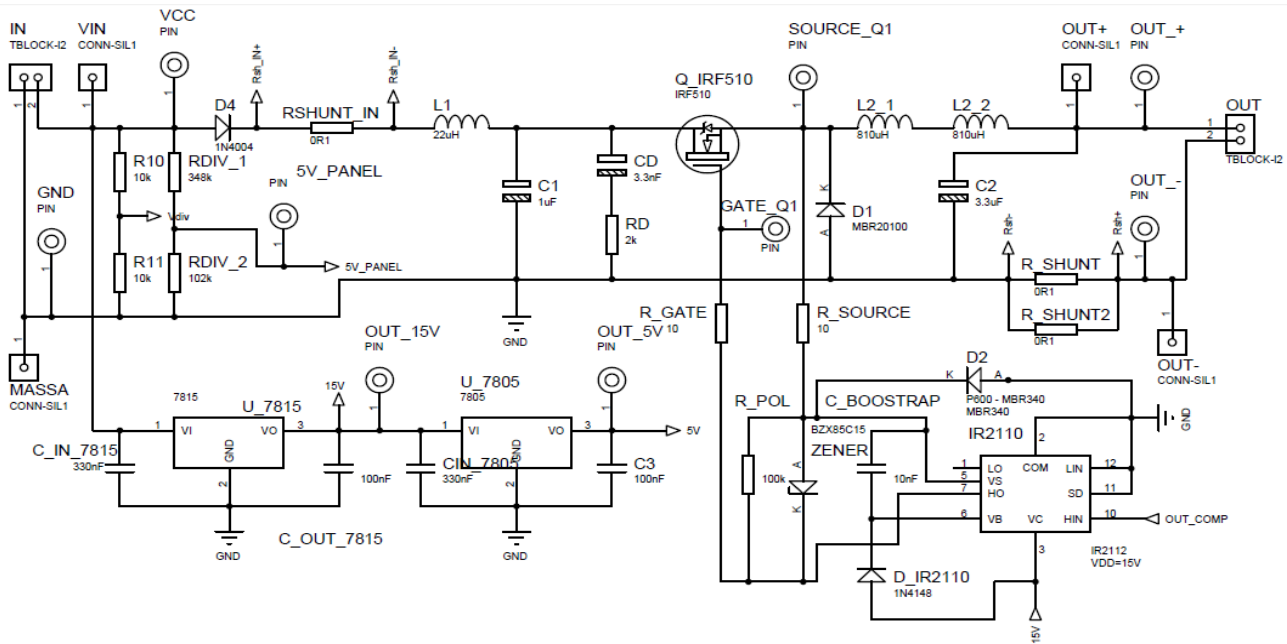


Fig. 5. Schematics of the implemented BIF *G*-type gyrator.

TABLE I. INITIAL DESIGN SPECIFICATIONS

$V_{in}=20\text{ V}$	$V_{out}=12\text{ V}$
$I_{in}=0,6\text{ A}$	$I_{out}=1\text{ A}$
$\Delta I_{out}=5\%$	$\Delta V_{out}=0,5\%$
	$R_L=0,11\ \Omega$

The design of the power gyrator is divided into two parts: On the one hand, the calculation of the components of the buck regulator, and, on the other, the other elements of the whole power gyrator structure, such as the filter input and the network stability.

A. Component Design of the Buck Converter

Assuming that, as design specifications, the converter operates in continuous conduction mode (CCM), that it has a nominal input voltage of 20 V, and is desired an output voltage equal to 12 V and a maximum load current of 1 A, the nominal duty cycle converter should be 60%. Once obtained the duty cycle, the values of the required inductance and capacitor can be obtained, setting an output current ripple equal to 5%, an output voltage ripple of 0.5%, and a switching frequency equal to 50 kHz. With these design specifications, an inductance of 1.64 mH is used, obtaining an output current ripple of 5.85%.

Finally, the standard value for the capacitor is  $C=3.3\ \mu\text{F}$ , achieving a ripple voltage equal to 0.37%, which is perfectly suited to the level required for the voltage ripple at the converter output terminals.

B. Component Design of the BIF Power Gyrator

As already mentioned, a *G*-type power gyrator has a variable *g*, an LC input filter, and a stable network whose parameters should be calculated to obtain the appropriate values for the provided initial conditions. To obtain *g*, the

above assumed initial conditions for currents and voltages at the converter input and output terminals are used, set  $g=0.050$ .

Calculating the input filter, it carries out to a standardized value of 22 µH for the inductance, and a value of 1 µF for the capacitor. As discussed above, *G*-type power gyrator structures require a stability network for ensuring their proper performance. This stability is achieved by a capacitor connected in series with a resistor, resulting in a 3.3 nF capacitor ( $C_d$ ) and a resistance  $R_d=2\text{ k}\Omega$ . These values are necessary in order to determine the stability network. In order to ensure the stability of the system, whose equations are determined by expressions (2), (3) and (4), these three expressions should be fulfilled with the obtained component values for this particular BIF *G*-type gyrator.

On the other hand, the necessary control law (in this case a sliding control) for the proper operation of the *G*-type gyrator should be established. Basically, this analog controller consists of a current sensing system comprising a shunt resistance of 50 mΩ, a difference amplifier, a multiplier (an AD633 from Analog Devices) for the product of the input voltage established by the parameter *g*, and a comparator with some hysteresis to fix the switching frequency.

Finally, the use of a PIC microcontroller (in this case, a Microchip’s PIC18F1220) achieves the tracking of the PV-panel MPP. In the case carried out in this article, the MPPT algorithm implemented has been the well-known perturb and observation (P&O) [1]. Notice that, for this tracking, it is necessary a second current and voltage sensing, in order to measure and introduce them to the PIC microcontroller. The output of the PIC responsible for providing the value for the parameter *g* should be an analog value; however, the PIC can only offer at its output binary states (5 V or 0 V). To overcome this problem, an RC filter is

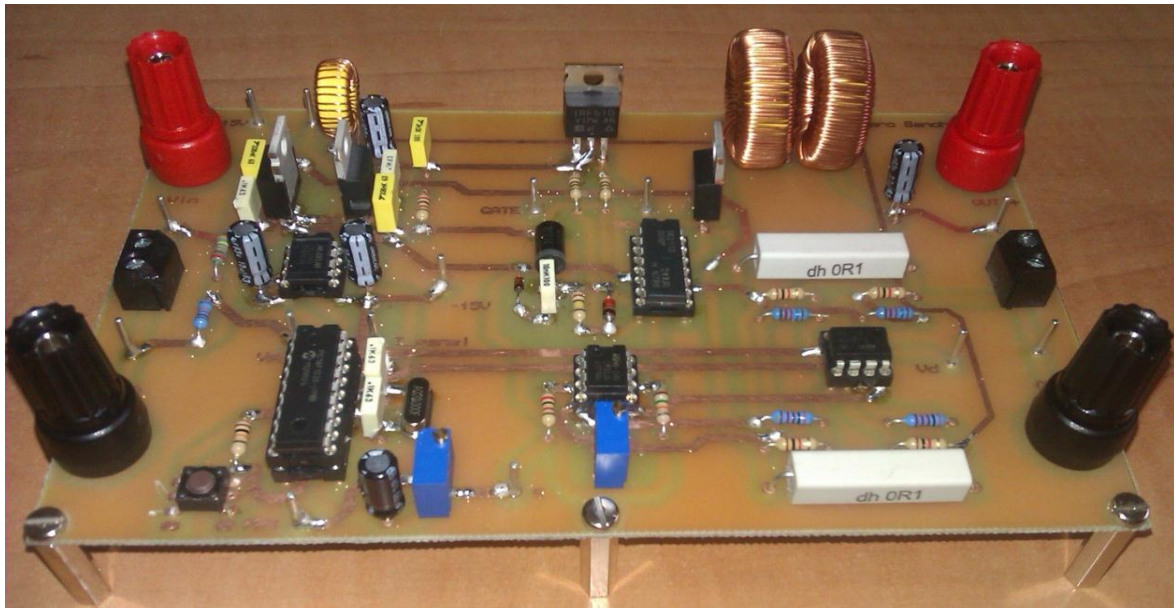


Fig. 6. Experimental efficiency of the *G*-type power gyrator for different values of the input current.

added, in order to filter the switching frequency of the output voltage and provide an average voltage that controls the power gyrator.

#### IV. IMPLEMENTATION, SIMULATION AND EXPERIMENTAL RESULTS OF THE FINAL IMPLEMENTED *G*-TYPE GYRATOR PROTOTYPE

Figure 5 shows the complete schematic of the converter BIF carried out in this work. In order to corroborate the proper operation of the designed and implemented BIF *G*-type gyrator, it has been powered by a solar panel. Therefore, the value of its parameter *g* is not fixed or manually adjustable, but the PIC microcontroller will be in charge of making the perturbation algorithm and monitoring to adjust the parameter *g* in order to always assure (independently of the irradiance conditions) the maximum power of the solar panel (MPPT). The final characteristics obtained from the implemented system are: Minimum input voltage equal to 18 V and nominal 20 V; and, output current adjustable between 1 A and 2.5 A, regardless of the value of the load connected, as long as the product of the output current and the load resistance is lower than the input voltage. Finally, figure 6 shows a photograph of the complete implementation performed.

For an input of 18 V, a reference voltage  $V_g$  whose value forces an input current of 1.9 A, and an output 4.7-Ω load, an output voltage and current equal to 11.8 V and 2.4 A, respectively, are obtained. For the prototype of the *G*-type power gyrator held for processing power of the photovoltaic panel, different lighting conditions for the solar panel were used by means of different points of light. After verifying their behavior as *G*-type power gyrator, an experimental analysis of the efficiency was carried out for different values of input current (setting the value *g*), and maintaining the value of the load equal to 4.7 Ω (Table II). The experimental efficiency of

the *G*-type power gyrator, for different input currents, is shown in Figure 7.

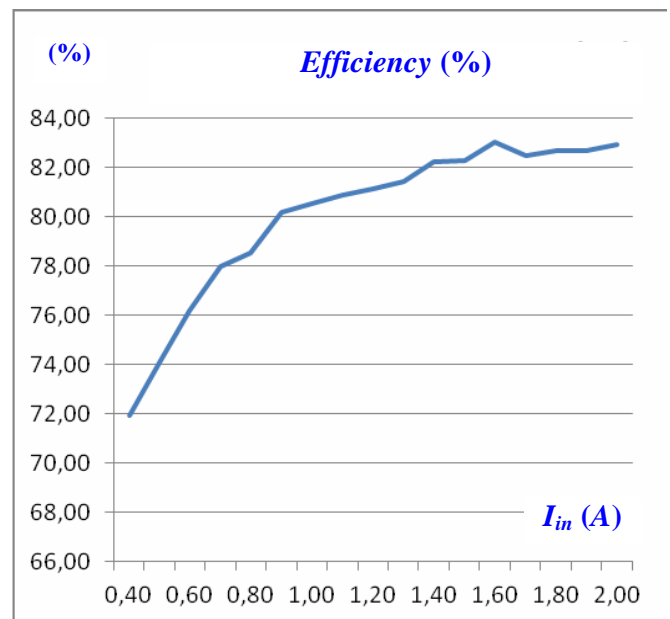


Fig. 7. Experimental efficiency of the *G*-type power gyrator for different values of the input current.

This graph shows how, as the *G*-type power gyrator works closer to the optimum point ( $I_{in}=2 A$ ), the performance and efficiency are enhanced. Note that the efficiency of the gyrator is determined by the value of the load, and that, for a given output current value, different output voltages can be obtained. Finally, in figure 8, we can appreciate output current response when the reference voltage that adjusts the parameter *g* has an increasing step from 25 mV to 50 mV at  $t=25 ms$ , and when the input voltage suffers a new increasing step from 20 V to 22 V at  $t=50 ms$ . In both cases, notice that the output current is modified according to equation (1).

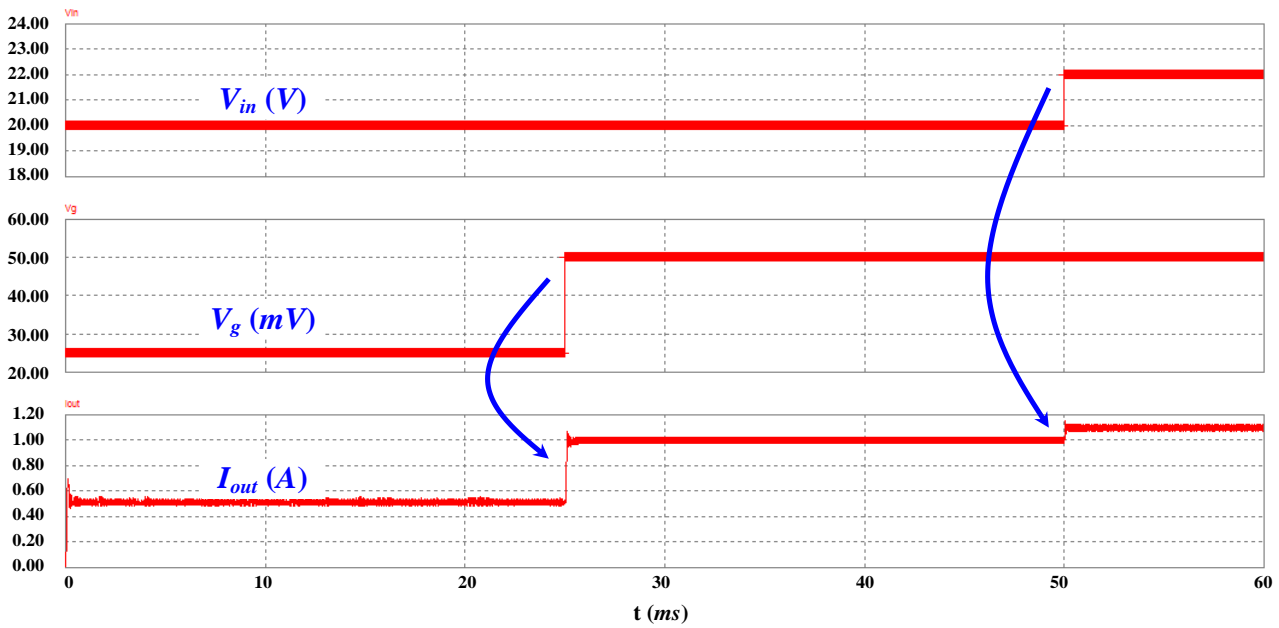


Fig. 8. Simulation results of the implemented G-type power gyrator.

TABLE II. EXPERIMENTAL RESULTS TO OBTAIN THE EFFICIENCY OF THE G-TYPE POWER GYRATOR IMPLEMENTED

$I_{in}$ (A)	$V_{out}$ (V)	$I_{out}$ (A)	$P_{in}$ (W)	$P_{out}$ (W)	$\eta$ (%)
0.40	5.03	1.03	7.20	5.18	71.96
0.50	5.70	1.17	9.00	6.67	74.10
0.60	6.33	1.30	10.80	8.23	76.19
0.70	6.92	1.42	12.60	9.83	77.99
0.80	7.44	1.52	14.40	11.31	78.53
0.90	7.97	1.63	16.20	12.99	80.19
1.00	8.43	1.72	18.00	14.50	80.55
1.10	8.85	1.81	19.80	16.02	80.90
1.20	9.27	1.89	21.60	17.52	81.11
1.30	9.67	1.97	23.40	19.05	81.41
1.40	10.06	2.06	25.20	20.72	82.24
1.50	10.43	2.13	27.00	22.22	82.28
1.60	10.82	2.21	28.80	23.91	83.03
1.70	11.12	2.27	30.60	25.24	82.49
1.80	11.45	2.34	32.40	26.79	82.69
1.90	11.78	2.40	34.20	28.27	82.67
2.00	12.09	2.47	36.00	29.86	82.95

### V. CONCLUSIONS

This paper has provided, on the one hand, a classification of high efficiency switching power-gyrator structures and, on the other, the validity of their use as cells for energy processing in photovoltaic solar installations. In particular, having into account the properties of these topologies presented in the article, their inclusion in solar facilities allows increasing the performance of the whole installation. The design, simulation and implementation of a G-type power gyrator are carried out

throughout the article, including a sliding control implemented by means an analog controller.

In addition to the use of the aforementioned switching power gyrator, a maximum power point tracking (MPPT) is mandatory in the energy processing path in order to obtain the maximum power from the photovoltaic solar panel. Therefore, the practical implementation carried out includes a control loop of the power gyrator in order to track the aforementioned maximum power point of the photovoltaic solar panel. In the presented design, this MPPT circuit has been implemented by means of a PIC microcontroller, a Microchip’s PIC18F1220, that achieves the tracking of the PV-panel MPP. In the case carried out in this article, the MPPT algorithm implemented has been the aforementioned perturb and observation (P&O).

### ACKNOWLEDGMENT

This work has been partially funded by project TEC2010-15765/MIC from the Spanish *Ministerio de Ciencia e Innovación* (MICINN) funds.

### REFERENCES

- [1] J.M. Enrique, E. Durán, M. Sidrach-de-Cardona, and J.M. Andújar. “Theoretical Assessment of the Maximum Power Point Tracking Efficiency of Photovoltaic Facilities with Different Converter Topologies”, *Solar Energy*, Vol. 81 (n. 1), pp. 31-38, Jan. 2007.
- [2] D. H. Tellegen. “The Gyrator, a New Electric Network Element”, *Philips Research Reports*, Vol. 3, pp. 81-101, Apr. 1948.
- [3] S. Singer, and R. W. Erickson. “Canonical Modeling of Power Processing Circuits Based on the POPI Concept”, *IEEE Transactions on Power Electronics*, Vol. 7 (n. 1), pp. 37-43, Jan. 1992.

- [4] A. Cid-Pastor, L. Martínez-Salamero, C. Alonso, J. Calvente, and G. Schweitz. "Synthesis of PWM-Based Power Gyration", *Proceedings of the IEEE International Symposium on Industrial Electronics (ISIE 2005)*, Vol. 3, pp. 1013-1018, 20-23 Jun. 2005.
- [5] A. Cid-Pastor, L. Martínez-Salamero, C. Alonso, B. Estibals, J. Alzieu, G. Schweitz, and D. Shmilovitz. "Analysis and Design of Power Gyration in Sliding-Mode Operation", *Proceedings of the IEE Electric Power Applications*, Vol. 152 (n. 4), pp. 821-826, 8 Jul. 2005.
- [6] A. Cid-Pastor, L. Martínez-Salamero, C. Alonso, A. El Aroudi, and H. Valderrama-Blavi. "Power Distribution Based on Gyration", *IEEE Transactions on Power Electronics*, Vol. 24 (n. 12), pp. 2907-2909, Dec. 2009.



# Operation of intelligent wind power unit

## 智能風力發電機器的工作

Ahmed Mohamed Galal<sup>1</sup>, Toshiaki Kanemoto<sup>2\*</sup>, Kazumasa Makita<sup>3</sup> and Yusuke Taneo<sup>3</sup>

<sup>1</sup>Faculty of Engineering, Mansoura University, Mansoura, Egypt

<sup>2</sup>Faculty of Engineering, Kyushu Institute of Technology, Kitakyushu 804-8550, Japan

<sup>3</sup>Graduate School of Engineering, Kyushu Institute of Technology, Kitakyushu 804-8550, Japan

kanemoto@mech.kyutech.ac.jp

Accepted for publication on 22<sup>th</sup> July 2014

**Abstract** – The Intelligent Wind Power Unit is composed of a large-sized front wind rotor, a small-sized rear wind rotor and a peculiar generator with double rotational armatures without the traditional stator. The superior operation of the tandem wind rotors has been verified and the desirable profile of the rotors has been presented in previous papers. In this paper, the blade setting angle is adjusted, not only to get a maximum efficiency at lower wind velocity but also to keep the output constant at the rated operation in the laboratory experiments. The model unit with the double rotational armature type doubly-fed induction generator is also provided for the natural wind circumstance, and the output performance is adjusted well with the exciting voltage and the frequency of the secondary circuit in the generator.

**Keywords** – Wind turbine, Tandem wind rotors, Generator.

### I. INTRODUCTION

Wind power is one of significantly promising resources for sustainable/renewable energies that may play a very important role in electric power generation at the 21st century. Wind turbines have been developed/improved to increase the output, and have been positively/effectively provided for the grid system. The authors have also invented a superior wind power unit, "Intelligent Wind Power Unit", as shown in Fig.1 [1][2]. The unit is composed of a large-sized front wind rotor, a small-sized rear wind rotor and a peculiar generator with double rotational armatures without the traditional stator. The front and the rear wind rotors drive the inner and the outer rotational armatures, respectively. Rotational speeds and directions of both wind rotors/armatures are automatically adjusted pretty well in response to wind circumstances.

The idea of tandem wind rotors has been proposed before [3]-[9], but not only the profiles but also the operations of the experiments on tandem wind rotors quite differ from those surveyed above. That is, the rotational directions and speeds of both wind rotors/armatures are automatically adjusted in

response to the wind velocity. Both wind rotors start to rotate at low wind velocity, namely the cut-in wind velocity, but the rear wind rotor counter-rotates against the front wind rotor. The rear wind rotor reaches the maximum rotational speed at the rated wind velocity. With more increase of the wind velocity, the rotational speed of the rear wind rotor decreases gradually, stops and then begins to rotate at the same direction of the front wind rotor, so as to coincide with the larger rotational torque of the front wind rotor.

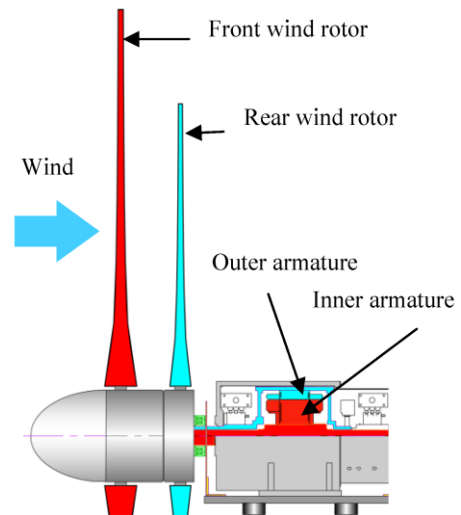


Fig. 1 Profile of Intelligent Wind Power Unit

Such superior operations of the tandem wind rotors have been verified experimentally and the desirable profiles of the wind rotors have been proposed [10]-[12]. Continuously, in this paper, the blade setting angle is adjusted, not only to get a maximum efficiency at lower wind velocity but also to keep

the output constant at the rated operation in the laboratory experiments. The model unit equipped with the double rotational armature type doubly-fed induction generator is also provided for the natural wind circumstance.

## II. ADJUSTMENT OF BLADE SETTING ANGLE EXPERIMENTS IN A WIND TUNNEL

The model tandem wind rotors were set, perpendicularly to the wind direction, at the outlet of the wind tunnel with nozzle diameter of 800 mm. The front and the rear wind rotors connected directly and respectively to the isolated motors controlled by the inverter with the regenerative braking system, in place of the peculiar generator. The diameter of the front wind rotor is  $d_F = 500$  mm with three blades, and the rear wind rotor is  $d_R = 420$  mm with five blades. The axial distance between the twist center of the front and the rear blade is  $l = 40$  mm. The diameter ration and the number of blades have been optimized at the laboratory researches [11] [13].

In the experiments, the rotational torques of the front and the rear wind rotors were counter-balanced by the rotational speed control in place of the double rotational armatures. The output is evaluated without the mechanical losses of bearings and pulley systems. The Reynolds number estimated with the relative velocity component and the chord length at the blade tip is  $Re = 5.8 \times 10^4 - 1.8 \times 10^5$ , which may be less than  $Re$  for prototypes but is in close to the turbulent flow because the higher fluctuation  $V'$  with  $RMS(V')/V = 3.6\%$  ( $V_{max}/V = 11\%$ ,  $V$ : the wind velocity) at the nozzle outlet promotes the transition from the laminar to the turbulent flows on the blade surfaces.

### OPTIMIZATION OF FRONT BLADE PROFILE

Previous research has suggested that the front wind rotor, at the smaller radius, had better not to absorb the wind energy but better to give away enough wind energy to the rear wind rotor [12]. That is, the front wind rotor never generates the swirling velocity component at the smaller radius while the coming flow is in axial direction.

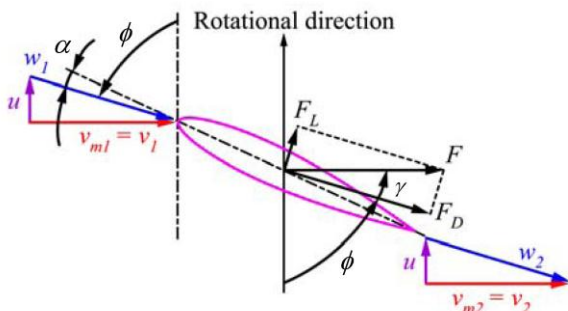


Fig. 2 Flow condition around the front wind rotor at the smaller radius

Figure 2 shows the velocity triangles around the front blade at the smaller radius, where  $v$ ,  $u$ ,  $w$  and  $v_m$  are the absolute, the rotational, the relative, and the axial velocity components (subscripts 1 and 2 mean the inlet and the outlet). The resultant force  $F$  must be in the axial direction and has no tangential

component. Equation (1) gives the lift-drag ratio  $\varepsilon$  and Equation (2) gives the relative flow angle  $\phi$ , while Equation (3) gives the angle  $\gamma$  between the drag force  $F_D$  and  $F$ .

$$\varepsilon = F_L / F_D = u / v_{m1} = r\omega / v_{m1} \quad (1)$$

$$\phi = \tan^{-1}(v_{m1} / r\omega) = \tan^{-1}(F_D / F_L) \quad (2)$$

$$\gamma = \tan^{-1}(F_L / F_D) = \tan^{-1}\varepsilon \quad (3)$$

The blade must twist in the radial direction so as to satisfy  $\phi + \gamma = 90$  degrees while  $F$  is in the axial direction, and to make  $F_D$ , which decelerates the axial velocity, as small as possible.

Front Blade H shown in Fig. 3(a) was designed on the basis of the above advanced technology at the tip speed ratio  $\lambda_F =$  (blade tip speed)/ $V = 4.5$  and formed with NACA0015 symmetric airfoil [15] at the smaller radius ( $0.2 < R < 0.46$ ,  $R$ : the dimensionless radius divided by  $d_F/2$ ). The blade at the larger radius ( $0.54 < R$ ) has MEL002 airfoil [14] with the desirable angle of attack to get fruitful wind energy. Rear Blade G shown in Fig. 3(b) was formed tentatively with MEL002 airfoil [14] and was twisted to have the desirable angle of attack, taking account of the flow discharged from the front wind rotor. The tandem wind rotors designed just above (TWR HG) takes the maximum output coefficient of  $C_P = P/(\rho AV^3/2) = 0.35$  at the relative tip speed ratio  $\lambda_T = 6.3$ , where  $P$  is the output and  $A$  is the swept area of the front wind rotor.

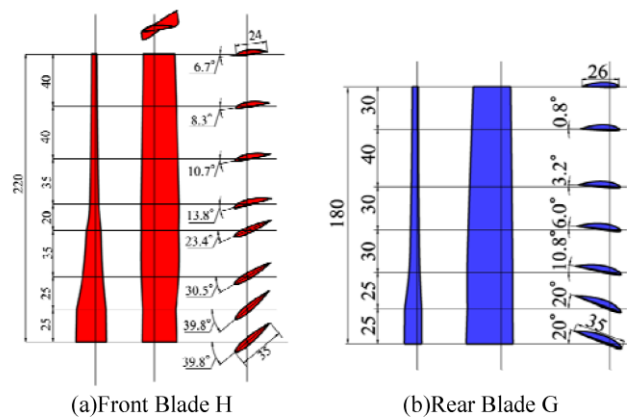


Fig. 3 Blade profiles for the tandem wind rotors

### PERFORMANCE AGAINST WIND VELOCITY

It may be possible to adjust the blade setting angle of the rear wind rotor,  $\beta_R$ , because the rotor is connected to the outer shaft as shown in Fig. 1, which can be easily equipped with a pitch control mechanism of the blade. Figure 4 shows the performance against the wind velocity, while  $\beta_R$  is adjusted to get a maximum efficiency under  $V = 10$  m/s and get a constant output  $P_T$  at the rated operation in keeping the blade setting angle of the front wind rotor  $\beta_F = 5$  degrees, where the angles are measured between the blade chord and the rotational directions at the blade tip. It is necessary to adjust the blade setting angle  $\beta_R$  for aerodynamically keeping the output constant at the rated operation. The relative rotational speed  $N_T = N_F - N_R$  decreases at the wind velocity  $V$  faster than 10 m/s,

as the increase of  $V$  accompanies the increase of the rotational torque.

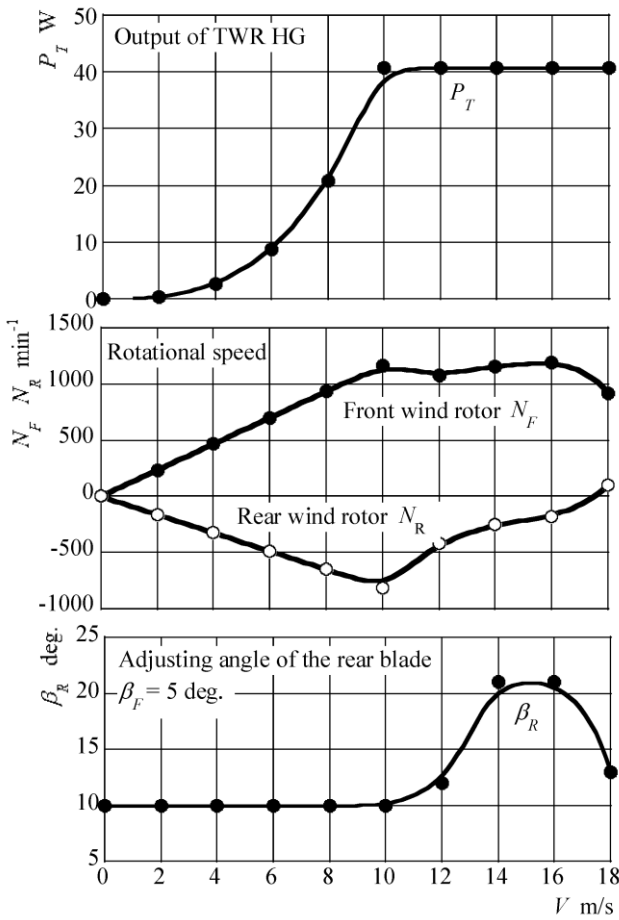


Fig. 4 Performance of the model unit in the wind tunnel

### III. OPERATION IN NATURAL WIND PREPARATION OF THE MODEL UNIT

The upwind type unit shown in Fig. 5 was prepared for the field tests. The front wind rotor has the diameter of  $d_F = 2000$  mm and is composed of three blades. The rear wind rotor has the diameter of  $d_R = 1640$  mm and is composed of five blades. The axial distance between both wind rotors is  $l = 160$  mm. These dimensions have also been optimized in previous papers [11][13]. The blade profiles of the front and the rear wind rotors are shown in Fig. 6, where these are designed on the basis of the advanced technology described above. The aerofoil sections of the blades are almost similar to those in Fig. 3, but the front blade at the smaller radius is formed with cambered aerofoil without load.

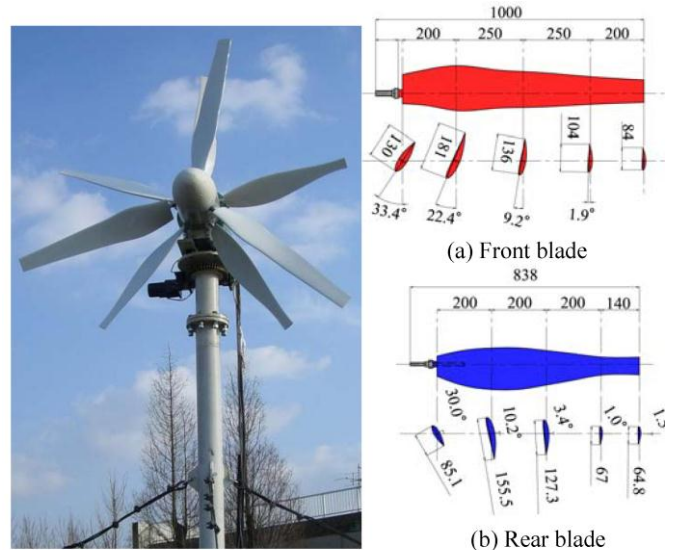


Fig. 5 Model unit

Fig. 6 Blade profiles

The above tandem wind rotors counter-drive the inner and the outer armatures in the doubly-fed induction generator (3-phase, 8-poles, [16]). The generator is composed of the primary circuit in the outer armature which induces the active power  $P_1$ , corresponding  $P_T$  in Fig. 3, and the secondary circuit in the inner armature which consume the reactive power for rotating the excited magnetic field. The rated output of the generator is 1.2 kW with the induced frequency  $f_1 = 60$  Hz and the induced voltage  $E_1 = 200$  V from the primary circuit while the relative rotational speed between the double rotational armatures is  $N_T = 900 \text{ min}^{-1}$ . The induced frequency  $f_1$  is determined with the rotational speed  $N_T$  and the exciting frequency  $f_2$  at the secondary circuit. The exciting voltage  $E_2$  at the secondary circuit, however, must be adjusted carefully in response to  $N_T$ , namely the wind velocity  $V$ , to keep  $E_1$  and  $f_1$  constant in the turbulent flow.

The model unit prepared above was installed on the tower of 2.4 m height which is set at the top roof of the building of 8 m height in the campus as shown in Fig. 5. The wind velocity was measured by the supersonic anemometer which is in front of the front wind rotor at the shaft centre and can detect the three dimensional flow directions.

#### WIND CIRCUMSTANCES AT THE TEST SITE

The test site has tall trees at the northern side and buildings at the southern side. These obstacles affect doubtlessly the wind circumstances from the north and the south. The wind rotor when facing the wind from the west side has comparatively better circumstance but may be poor for the power generation. Most of the time, the wind velocity is slower than 11 m/s while 3 m/s gives the highest apparent ratio with about 70 % appearance in 2~5 m/s, which may represent the wind circumstances at an urban area in Japan.

#### PERFORMANCE CONTROL AT NATURAL WIND

Figure 7 shows a small example for the rotational speed of the front and the rear wind rotors,  $N_F, N_R$ , the active output  $P_1$ ,

the induced voltage  $E_1$ , and the induced electrical current  $I_1$  from the primary circuit against the wind velocity  $V$ , while the bulb load  $P_{bulb} = 600$  W, namely the electrical resistance as the power consumption, and the exciting voltage  $E_2 = 60$  V, the exciting frequency  $f_2 = 50$  Hz at the secondary circuit. The experimental date accumulated during the test was averaged each one minute and the white circles in the figure represent the performances averaged each 0.5 m/s band [17]. The output  $P_1$  and the rotational speeds  $N_F, N_R$  are widely distributed even at the same wind velocity, because the small-sized wind rotors are sensitive to the turbulent/velocity fluctuation and/or wind direction in the natural wind. The front and the rear wind rotor start counter-rotating at slow wind speed and these speeds increase with the increase of the wind velocity. The induced voltage  $E_1$  is in proportion to the relative rotational speed  $N_T = N_F - N_R$ , and  $P_1 = \text{square-root}(3)E_1I_1$ , where  $I_1$  is the induced electrical current.

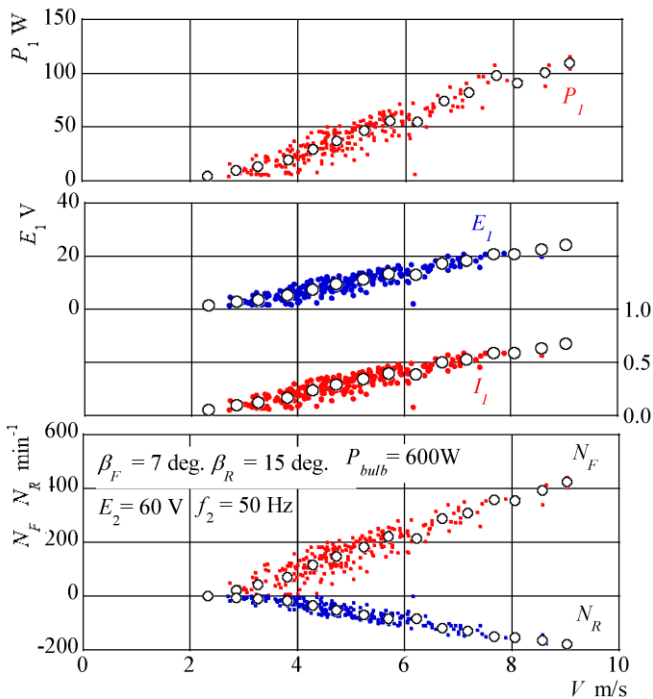


Fig. 7 Example of the performance at the natural wind

Figure 8 shows just a small sample for how to adjust the exciting voltage  $E_2$ , the exciting frequency  $f_2$  and the blade setting angle of the rear wind rotor  $\beta_R$ , to keep the active output  $P_1$  constant at the rated operation, while the induced voltage  $E_1 = 50$  V and the induced frequency  $f_1 = 60$  Hz. The output and the power quality can be guaranteed well with the reasonable adjustments of  $E_2$  and  $f_2$  at the secondary circuit and  $\beta_R$ . The wind power station can provide the net output  $P_N$  for the grid system, where  $P_N = P_1 - \text{square-root}(3)E_2I_2$  where  $I_2$  is the electric current in the secondary circuit.

The rotational direction of the rear wind rotor does not change from the counter-rotation, at the comparatively slower wind velocity in Figs. 7 and 8.

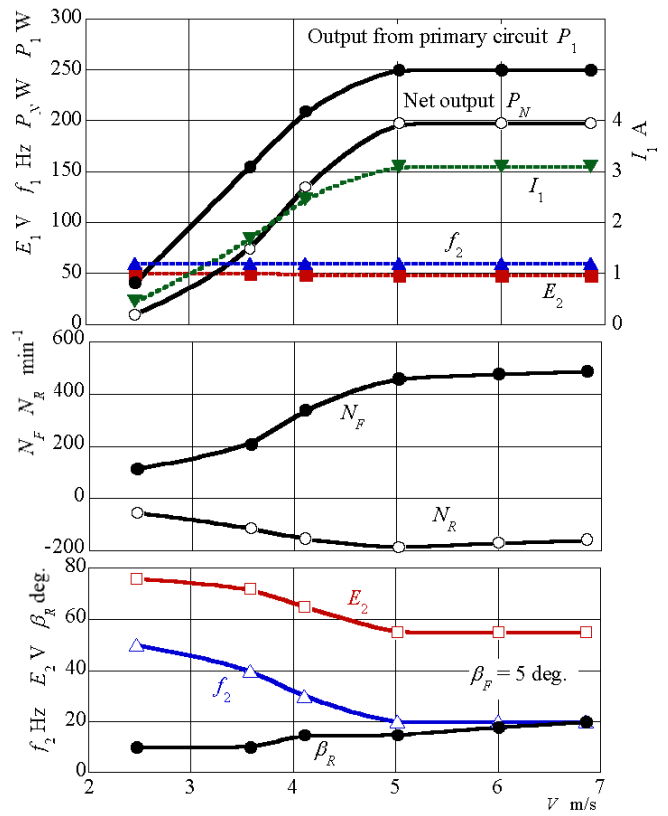


Fig. 8 Guarantee of the output and the power quality

IV. CONCLUDIG REMARKS

The blade setting angle of the rear wind rotor was adjusted, not only to get a maximum efficiency at lower wind velocity but also to keep the output constant at the rated operation in the laboratory experiments. The model unit with the double rotational armature type doubly-fed induction generator was also exposed in the natural wind circumstance. The output and the power quality from the primary circuit can be guaranteed well with the adjustment of the exciting voltage and frequency at the secondary circuit and the blade setting angle of the rear wind rotor.

REFERENCES

[1] T. Kanemoto, Ahmed Mohamed Galal, Y. Inada and Y. Konno, "Intelligent Wind Turbine Generator with Tandem Rotors Applicable to Offshore Wind Farm", *Proceedings of the 15th International Offshore and Polar Engineering Conference and Exhibition*, 1, Seoul, Korea, pp.457-462, 2005.

[2] T. Kanemoto and Ahmed Mohamed Galal, "Development of Intelligent Wind Turbine Generator with Tandem Wind Rotors and Double Rotational Armatures (1st Report, Superior Operation of Tandem Wind Rotors)", *JSME International Journal, Series B*, 49, No.2, pp.363-368, 2006.

- [3] A. Sper. David, "Wind Turbine Technology", *ASME Press*: New York, p. 93, 1994.
- [4] <http://www.kowintec.com/English/intro/info.htm>
- [5] I. Ushiyama, T. Shimota and Y Miura, "An Experimental Study of the Two Staged Wind Turbines," *Proceedings of World Renewable Energy Conference*; 909-912, 1996.
- [6] T. J. Jang & H. K. Heo, "Study on the development of wind power system using mutually opposite rotation of dual rotors", *Proc. of the Renewable Energy 2008*, CD-ROM O-WE-015, 2008.
- [7] K. Appa, "Counter rotating wind turbine system" *Energy Innovations Small Grant (EISG) Program Technical Report*, 2002.
- [8] S. N. Jung, T. S. No & K. W. Ryu, "Aerodynamic Performance prediction of 30kW counter-rotating wind turbine system" *Renewable Energy*, Vol. 30, No. 5, pp. 631-644, 2005.
- [9] W. Z. Shen, V. A. K. Zakkam, J. N. Sørensen & K. Appa, "Analysis of Counter-Rotating Wind Turbines", *Journal of Physics: Conference Series*, 75 012003(9pp), 2007.
- [10] K. Kubo and T. Kanemoto, "Performances and Acoustic Noise of Intelligent Wind Power Unit", *Renewable Energy & Power Quality Journal*, No.9, 445, 2011.
- [11] Edited by T. Wei, "Wind Power Generation and Wind Turbine Design", *WIT Press*, pp. 333-360, 2010.
- [12] Y. Usui, K. Kubo, and T. Kanemoto, "Intelligent Wind Power Unit with Tandem Wind Rotors and Double Rotational Armatures (Optimization of Blade Profiles in Front Wind Rotor)", *Journal of Energy and Power Engineering*, Vol. 6, No. 11, pp.1791-1799, 2012.
- [13] K. Kubo and T. Kanemoto, "Development of Intelligent Wind Turbine Unit with Tandem Wind Rotors and Double Rotational Armatures (2nd Report, Characteristics of tandem wind rotors)", *JSME International Journal*, Ser. B, Vol. 3, No. 3, pp. 370-378, 2008.
- [14] Performance and geometry of airfoil supply system, online at: <http://riodb.ibase.aist.go.jp/db060/index.html>
- [15] R.E. Sheldahl, P.C. Klimas, Aerodynamic characteristics of seven symmetrical airfoil sections through 180-degree angle of attack for use in aerodynamic analysis of vertical axis wind turbines, *Technical report of Sandia National Laboratory*, 27-40, 1981.
- [16] T. Kanemoto, Ahmed Mohamed Galal, K. Ikeda, H. Mitarai, and K. Kubo, "Intelligent Wind Turbine Generator with Tandem Rotors Applicable to Offshore Wind Farm (Characteristics of Peculiar Generator, and Performance of Three Dimensional Blades)", *Proceedings of the 17th International Offshore and Polar Engineering Conference*, Lisbon, Portugal, pp.363-368, 2007.
- [17] IEC 61400-12-1: Power Performance Measurements of Electricity Producing Wind Turbines.



# Stress analysis of NPP steam generator and main factors affecting safety

## 核电站蒸汽发生器应力分析及影响安全的主要因素

Hao Qian\* (钱浩), Xingyun Liang (梁星筠), Kefeng Zhang (张可丰),  
Kai Zhang (张锴), Yongcheng Xie (谢永诚), Xiaoyao Shen (沈小要)

Department of Component Research and Design, Shanghai Nuclear Engineering Research and Design Institute, Shanghai  
200233, China

[qianhao@snerdi.com.cn](mailto:qianhao@snerdi.com.cn)

Accepted for publication on 28 August 2014

**Abstract** - The steam generator (SG) serves as the primary means of removing the heat generated within the reactor core and is part of the reactor coolant system (RCS) pressure boundary in nuclear power plant (NPP). SGs are heat exchangers used to convert water into steam by the heat produced in the nuclear reactor core and deliver the steam to drive turbines to generate electricity. The main components of SGs are Equipment Safety Class 1 or Class 2, Seismic Design Category I and ASME B&PVC III NB components, whose structure integrity affects the safety of NPP directly. The stress analysis of SGs is performed under various loads by finite element models, such as seismic analysis, fatigue analysis, fracture analysis, flow-induced vibration (FIV) analysis, wear analysis, and so on. The results demonstrate that the stress combination and evaluation under each service level meet the requirement of the ASME B&PVC III.

In addition, the main factors affecting structure integrity and safe operation of SGs are summarized and proposed with the weak parts of SGs. For example, the environmental temperature of various conditions affects the fracture analysis results significantly. The seismic analysis results are sensitive to the stiffness of SGs' supports and the structure setting of anti-vibration bars (AVBs). Moreover, more than ten thousands of tubes, which are the key and weak components and are located between the primary and secondary coolant loops of NPP, are susceptible to flow induced vibration, wear, corrosion and seismic damage. These comments are expected to be significant for future analysis and design.

**Keywords** - nuclear power plant, steam generator, stress analysis, safety

**摘要** - 蒸汽发生器是排出反应堆堆芯热量的主要设备, 是核电站反应堆冷却剂系统压力边界的一部分。蒸汽发生器通过传热管将反应堆冷却剂从堆芯获得的热量传递给二次侧介质转化为蒸汽, 送入汽轮机发电。蒸汽发生器的主要部件为核安

全 1 级或 2 级、抗震 I 类、规范等级 ASME B&PVC III NB 部件, 其结构完整性直接影响核电站的安全性。本文对蒸汽发生器通过有限元建模方式对其进行了各种载荷下的应力分析, 包括抗震分析、疲劳分析、断裂分析、流致振动和磨损分析等。分析结果表明, 各种使用限制下蒸汽发生器的应力组合和评定结果满足 ASME B&PVC III 的相关要求。

同时, 本文归纳总结了可能影响蒸汽发生器结构完整性和安全运行的主要因素和结构薄弱部位。例如各种工况下的环境温度对断裂分析结果影响较大, 设备支撑刚度和抗振条设置对地震反应结果影响较大。此外, 蒸汽发生器中的万余根传热管处于一二回路边界, 既是设备关键部件也是薄弱部件, 易受流致振动、磨损、腐蚀、地震等影响而损坏。这些结论对后续蒸汽发生器的分析和设计具有一定的指导意义。

**关键词** - 核电站, 蒸汽发生器, 应力分析, 安全

### I. INTRODUCTION

Nuclear power plant (NPP) is the thermal power station in which the heat source is a nuclear reactor. As is typical in all conventional thermal power stations, the heat is used to generate steam which drives a steam turbine connected to a generator which produces electricity. Nuclear power is an important source of energy. As of 16 February 2014, the IAEA report there are 438 nuclear power reactors in operation operating in 31 countries [1]. Specially, about 75% country's electricity production is from nuclear power in France which is the highest nuclear power percentage country in the world. And about 50% new NPPs are being built in China now.

On the other hand, operating nuclear reactors contain large amounts of radioactive fission products which, if

dispersed, may pose a direct radiation hazard, contaminate soil and vegetation, and be ingested by humans and animals. Human exposure at high enough levels can cause both short-term illness and death and longer-term death by cancer and other diseases. Some famous accidents at nuclear power plants were the 2011 Fukushima nuclear disaster in Japan, 1986 Chernobyl disaster in Ukraine, and the 1979 Three Mile Island accident in the United States. Safety is one of the most important issues for Nuclear Power Plant, especially in post-Fukushima ages. The radioelement should be always kept in the Reactor Coolant System (RCS) safely.

Steam generators are heat exchangers used to convert water into steam by the heat produced in the nuclear reactor core. They are used in pressurized water reactors (PWR) between the primary and secondary coolant loops. The water flowing through the primary side of steam generator boils water in the shell side to produce steam in the secondary loop that is delivered to the turbines to make electricity. And steam generator is one of longest period production and heaviest equipments in NPP. The main components of SGs are Equipment Safety Class 1 or Class 2, Seismic Design Category I and ASME B&PVC III [2] NB components. Structure integrity of steam generator must be ensured to ensure the safety of NPP.

In this paper, stress analysis for steam generator of an abuilding nuclear power plant is performed to ensure the 60 years lifetime of the component with the FEM model. For example, seismic analysis, fatigue analysis, fracture analysis, flow-induced vibration (FIV) analysis and wear analysis are performed. And the analysis results of SG demonstrate that the stress combination and evaluation under each service level meet the requirement of the ASME B&PVC III [2]. In addition, the main factors affecting structure integrity and safe operation of SGs are summarized and proposed with the weak parts of SGs. For example, the environmental temperature of various conditions affects the fracture analysis results significantly. The seismic analysis results are sensitive to the stiffness of SGs' supports and the structure setting of anti-vibration bars (AVBs). Moreover, more than ten thousands of tubes, which are the key and weak components and are located between the primary and secondary coolant loops of NPP, are susceptible to flow induced vibration, wear, corrosion and seismic damage. These comments are expected to be significant for future analysis and design.

## II. GEOMETRY AND MATERIAL OF STEAM GENERATOR

The Steam Generator, shown in Fig.1, is a vertical shell and U-tube evaporator with integral moisture separating equipment. Its basic function is to transfer heat from the single-phase reactor coolant water through the U-shaped heat exchanger tubes to the boiling, two-phase steam mixture in the secondary side. The steam generator separates dry and saturated steam from the boiling mixture, and delivers the steam to a nozzle from which it flows to the turbine. In addition to its steady-state heat transfer function, the steam generator secondary side provides a water

inventory which is available as a heat sink to mitigate primary side high temperature transients and to accommodate accident conditions. The principal subcomponents of the steam generator include the channel head, tubesheet, lower shell, tube bundle, steam drum, and moisture separating equipment. The channel head, tubesheet, and tube bundle form the primary pressure boundary for the reactor coolant.

The material of the main subcomponents is SA-508, Grade 3 Class 2 per ASME code, such as channel head, tubesheet, lower shell, upper shell and so on. The material of tube is Alloy 690. The material strengths and physical properties can be obtained from the ASME Code [3].

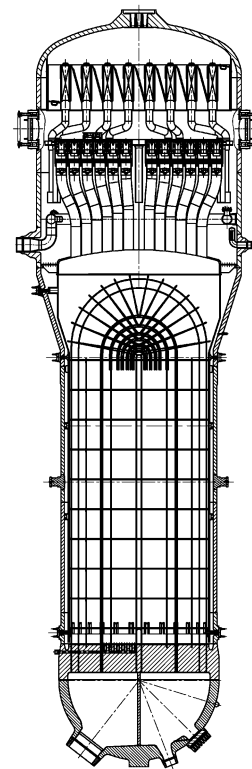


Fig.1, Structure drawing of Steam Generator

## III. LOADS REQUIREMENT OF ANALYSIS

The design basis of SG is sixty (60) years with 90 percent availability over the design life. Design temperature and design pressure of primary side is 350°C and 17.2 MPa, respectively. And design temperature and design pressure of secondary side is 320°C and 8.2 MPa. The steam generator shall be capable of satisfying functional and safety requirements under Design, Level A, Level B, Level C, and Level D conditions. The number of transient occurrences is based on a plant design life of 60 years. And the effects of pre-operational passive core cooling test transients shall be evaluated. The steam generator (including nozzles and supports) shall be analyzed using the load combinations. For example, internal design pressure, dead weight, Service Level A's design mechanical loads and external mechanical loads, such as the nozzle reactions associated with piping systems, are considered in design condition. And dynamic

load associated with Level A (Normal) service conditions, peak pressure, dead weight, and external mechanical loads are considered in Level A condition. Especially, the load of Safe Shutdown Earthquake (SSE), postulated pipe rupture events and locked rotor is considered in Level D (Faulted) condition.

#### IV. ANALYSIS AND EVALUATION FOR STEAM GENERATOR

##### 4.1 ANALYSIS AND CALCULATION

The analysis employs finite element methods using the ANSYS Computer Code for stress analysis mainly. The stress analysis of SGs is performed under various loads by finite element models, such as seismic analysis, fatigue analysis, fracture analysis, flow-induced vibration (FIV) analysis, wear analysis, and so on. The calculated stresses are compared to the allowable stress values calculated using  $S_m$ ,  $S_y$ , and  $S_u$  values.

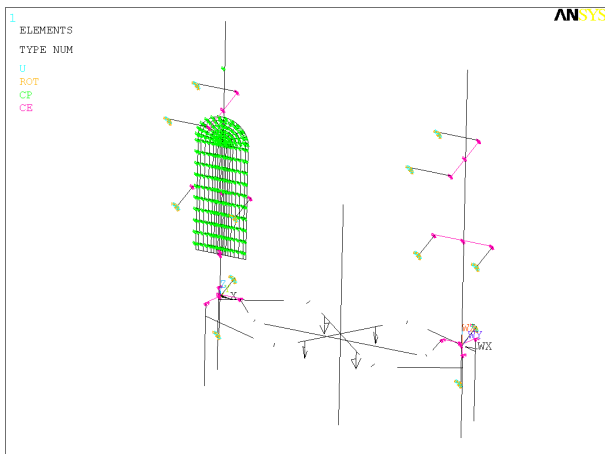


Fig.2, Seismic Model of SG with Reactor Coolant Loop (RCL)

The analysis model of SG is created with moisture separator assembly and tube bundle assembly. And the seismic analysis is performed with reactor coolant system RCS model with superelement element MATRIX50 under Safe Shutdown Earthquake. The seismic model of SG is shown in Fig.2 and Fig.3. The major structural components idealized in the finite element model include the steam generator shell (primary and secondary side pressure boundary), primary and secondary separators, wrapper, stayrods, deck plates, tube bundle, AVBs and tube support plates (TSPs). The model of the SG consists of a system of pipe elements PIPE16, beam elements BEAM4, and general matrix elements MATRIX27 (with both mass and stiffness options). The stiffness values of the lower, intermediate and upper supports are represented using one spring elements (COMBIN14). In Fig.2 and Fig.3, U is displacement constraints, ROT is rotation constraints. And CP defines a set of coupled degrees of freedom. CE defines a constraint equation relating degrees of freedom. The largest (purple) arrows mean the displacement constraints of the reactor pressure vessel support. The working plane shown by WX, WY, and WZ is an imaginary plane as the temporary modeling tool.

Moreover, LOCA Rarefaction Analysis and LOCA Shaking Analysis also apply this SG model without RCS model.

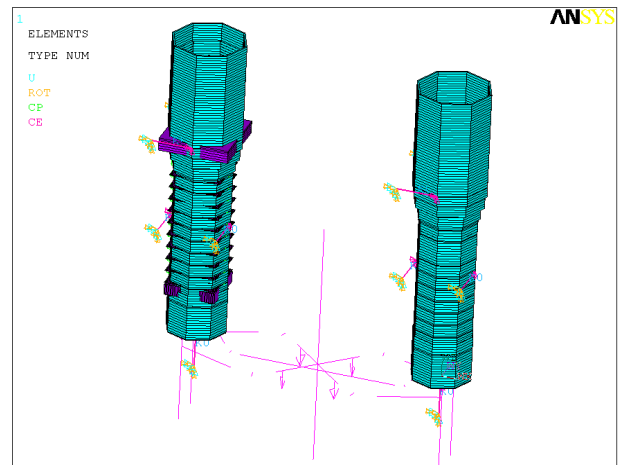


Fig.3, Seismic Model of SG (Display with elements shapes determined from the real constants [4])

Flow induced vibration analysis are perform to prevent the fluid-elastic instability (FEI) and obtains the vibration response of tubes, which is the input of wear analysis of SG. In wear analysis of SG tube, the Archard method is applied. To predict and evaluate fretting damage, the flow field in the equipment and flow-induced vibration response of SG tube is calculated and obtained. The Archard equation [5-6] is used to predict the wear as shown below.

$$\dot{V} = K \dot{W} \tag{1}$$

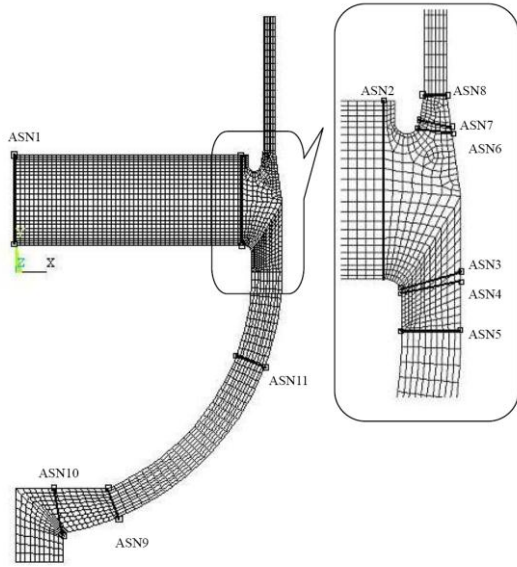
where  $\dot{V}$  is wear volume rate,  $\dot{W}$  is work rate, and  $K$  is wear coefficient to be measured by experiment. Work rate is defined as the normal component of contact force,  $F$ , integrated over the real sliding distance  $s$

$$\dot{W} = \frac{1}{t} \int F ds \tag{2}$$

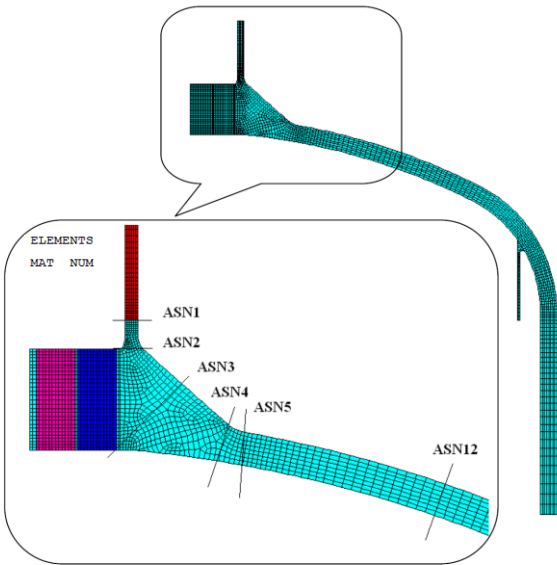
where  $t$  is time. The wear volume and wear depth is obtained in the design life of components. Enough thickness should be ensured by design. Predicted material loss over the design life of the steam generator due to flow-induced vibration and wear is calculated for steam generator components by relating material loss to local flow velocity through theoretical and empirical correlations. These predicted material losses, along with material loss due to corrosion, are considered in later analyses.

According to the load from former analysis, the strength analysis, fatigue analysis, and fracture analysis are performed using the axisymmetric model of components one by one. For example, analysis model and limiting stress locations of channel head (lower head), tubesheet, lower shell assembly and steam nozzle, elliptical head, upper shell, support ring assembly are shown in Fig.4, in which ASN is Analysis Section Number. And the different material types of elements are shown in Fig 4(b) with different colors. The calculation and analysis are performed for design, normal, upset, emergency, faulted and test condition. And primary

inlet nozzle, primary outlet nozzle, primary manway, tubes, cone, feedwater nozzle, et. al., are modeled respectively. The stresses due to the pressure loads, thermal loads and the external mechanical loads are obtained. Thermal loads are temperature gradients (distributions) due to the thermal transients in the components and are also obtained using these finite element analyses.



a) Channel Head, Tubesheet, and Lower Shell Assembly



b) Steam Nozzle, Elliptical Head, Upper Shell and Support Ring

Fig.4, Analysis Model and Limiting Stress Locations of some components

The fatigue evaluation is performed per ASME B&PVC III-1 NB-3222.4(e) [2]. The primary plus secondary plus peak stresses (total stresses) are used in determining the cumulated fatigue usage factor for each of the limiting locations. The design fatigue curves of ASME B&PVC III-1 [2] Appendix I is applied.

Non-Ductile failure evaluation is performed per ASME B&PVC III-1 NB-3211(d) [2] and Appendix G to prevent brittle fracture of components. WRCB 175 [7] “PVRC Recommendations on Toughness Requirements for Ferritic Materials” is applied by the guidance of ASME B&PVC III-1 Appendix G [2]. And  $K_{IC}$ , the lower bound static initiation critical  $K_I$  value, is applied for the evaluation of the postulated flaw size to ensure non-ductile failure does not occur.

#### 4.2 EVALUATION OF COMPONENTS

The stress results are evaluated per ASME B&PVC III [2]. The calculated stress intensities, the ASME Code allowable stress limits, the ratios of the stress intensities to the allowable limits, and the calculated fatigue usage factors for each location are calculated. Herein, the results of two typical locations ASN 2 of tubesheet and ASN 4 of elliptical head (upper head) are shown in Table 1, where  $P_m$  is general primary membrane stress intensity,  $P_L$  is local primary membrane stress intensity,  $P_b$  is primary bending stress intensity, and  $Q$  is secondary stress intensity. The stress category method refers to ASME B&PVC III-1 NB Tables NB-3217-1 [2]. The results demonstrate that the stress combination and evaluation under each service level meet the requirement of the ASME B&PVC III [2].

Further more, the results from the fracture mechanics assessment are obtained. The results of the most rigorous transient of typical locations ASN 4 of tubesheet are shown in Table 2, where N19 is primary to secondary side leak test, and T01 is primary side hydro test. The lowest temperature is chose for evaluation. In primary side hydro test, the method of WRCB 175 [7] is applied, and the critical flaw size 17.78 mm is obtained which are detectable by current inspection techniques and are therefore acceptable.

#### V. MAIN FACTORS AFFECTING SAFETY

The safety and function of SG depend on the structure integrity of the equipment. The design basis of the Steam Generator is 60 years with 90 percent availability over the design life. The main factors affecting structure integrity and safe operation of SGs are summarized and proposed with the weak parts of SGs. Particularly, more than ten thousands of tubes, which are the key and weak components and are located between the primary and secondary coolant loops of NPP, are susceptible to flow induced vibration, wear, corrosion and seismic damage. The main factors affecting structure integrity and safety of SG are as follows:

- 1) Earthquake. SG should keep the structure integrity under Safe Shutdown Earthquake. The engineering and society pay more attention on the seismic ability of equipment, especially in post-Fukushima ages. The stress of tubes under SSE is not small, which occupies about 50% of ASME allowable stress (stress limit). The parameter sensitivities of seismic analysis results are studied, such as the effect of another SG of RCS, support, anti-vibration bars (AVBs), and so on. The results indicate

TABLE 1, STRESS ANALYSIS RESULTS AND EVALUATION OF STEAM GENERATOR’S SOME TYPICAL LOCATIONS

Loading Condition	Stress Category	Tubesheet (ASN 2)			Elliptical Head (ASN 5)		
		Stress (MPa)	Allow (MPa)	Ratio	Stress (MPa)	Allow (MPa)	Ratio
Design	P <sub>m</sub>	22.16	207	0.11	/	/	/
	P <sub>L</sub>	/	/	/	189.19	310	0.61
	P <sub>m</sub> +P <sub>b</sub>	222.98	310	0.72	/	/	/
	Triaxial σ	28.39	827	0.03	380.96	827	0.46
Level B (Upset)	P <sub>m</sub>	25.22	228	0.11	/	/	/
	P <sub>L</sub>	/	/	/	198.08	341	0.58
	P <sub>m</sub> +P <sub>b</sub>	279.46	341	0.82	/	/	/
	Triaxial σ	33.62	827	0.04	398.30	827	0.48
Level A, B & Test (Normal, Upset & Test)	P <sub>m</sub> +P <sub>b</sub> +Q	479.03	740	0.65	546.45	621	0.88
	Fatigue Usage	/	1	0.23	/	1	0.84
Level C (Emergency)	P <sub>m</sub>	26.83	335	0.08	/	/	/
	P <sub>L</sub>	/	/	/	200.18	564	0.35
	P <sub>m</sub> +P <sub>b</sub>	321.51	557	0.58	/	/	/
	Triaxial σ	15.49	827	0.02	410.12	993	0.41
Level D (Faulted)	P <sub>m</sub>	28.86	434	0.07	/	/	/
	P <sub>L</sub>	/	/	/	242.80	652	0.37
	P <sub>m</sub> +P <sub>b</sub>	344.26	652	0.53	/	/	/
Test	P <sub>m</sub>	33.84	373	0.09	/	/	/
	P <sub>L</sub>	/	/	/	227.62	559	0.41
	P <sub>m</sub> +P <sub>b</sub>	423.93	560	0.76	/	/	/
	Triaxial σ	40.02	827	0.05	448.47	827	0.54

TABLE 2, NON-DUCTILE FAILURE EVALUATION RESULTS OF A TUBESHEET’S LOCATION

ASN Number	Section Thickness T(mm)	Transient No.	Transient Temperature (°C)	K <sub>I</sub>	K <sub>IC</sub>	K <sub>I</sub> /K <sub>IC</sub>	Postulated Flaw Size a (mm)
ASN 4	290.87	N19(Normal)	8	89.76	111.23	0.81	T/4
		U05-B(Upset)	215.01	155.27	219.78	0.71	T/4
		E06(Emergency)	170.33	178.99	219.78	0.81	T/4
		F02(Faulted)	127.50	157.17	219.78	0.72	T/4
		T01(Test)	8	-	-	0.99	17.78

that seismic results are sensitive to support stiffness and AVBs setting number.

- 2) Fatigue. The equipments of the third generation NPP with 60 years design life endures more cycles of transients than the equipments of the second generation NPP with 30~40 years design life. The fatigue results or equipments’ life depends on cycles of transients, stress of components and fatigue parameters of material mainly. Generally, the cumulated fatigue usage factor is large in high stress region and structural discontinuous region. Especially, life reduction of metal components due to the effects of the light-water reactor environment is the research focus in the world [8]. And fatigue monitoring system in service are being researched and

developed. Moreover, if the analysis results indicate that the fatigue results don’t meet the requirement of ASME code, there are some methods that can be tried to solve the problem, such as improvement of component structure, application of more accurate transients data, application of more accurate analysis method, and so on.

- 3) Fracture. Fracture mechanics is a main branch of modern mechanics, which studies the fracture strength of the material or component with defects to deal with the catastrophic low stress brittle fracture problem in many actual projects. A series of failures of several large structures occurred, including pressure vessels, storage tanks, ships, gas pipe lines, bridges, dams and many welded parts. There is relationship between reference nil

ductility temperature, fracture toughness, critical defect size and structural integrity. Particularly, the environmental temperature of various conditions affects the fracture analysis results significantly. If the nonconformance case about fracture occurs, some method can be applied to solve the problem, such as modification of service temperature, application of more accurate analysis method, and improvement of nondestructive examination capabilities. The actuality, which is worth noting, is that American Electric Power Research Institute (EPRI) knows its nondestructive examination capabilities, but Chinese companies do not know its NDE capabilities exactly.

- 4) Flow induced vibration. There are some flow induced vibration accidents of exchanger occurring. For example, after the replacement steam generators had been operating for approximately 11 months, San Onofre Nuclear Generating Station (SONGS) Unit 3 in American Southern California was brought into an unplanned shutdown due to primary to secondary leakage on January 31, 2012. NRC's preliminary analysis conclusion [9] was that the replacement steam generators were damaged by in-plane fluid-elastic instability (FEI) which is the first occurrence within the industry. Flow induced vibration may be relative to steam quality and flow velocity, natural frequency of structure, gap between tubes and AVBs, layout of AVBs, effective AVB contact force, and so on.
- 5) Fretting wear. EPRI's data showed that over 50% of PWR (Pressurized Water Reactor) world wide had reported some occurrence of Steam Generation (SG) tube fretting wear, which mainly resulted from flow induced vibration. Fretting wear of steam generator tube generally occurs between tube and anti-vibration bar (AVB) [10]. The fretting wear of tubes in the life time depends on the flow induced vibration response and the wear performance parameter of materials. About 50% new NPPs are being built in China. A lot of material and components are made in China for the first time. Fretting experiment is important and essential for domestic material and components, which is foundation and input of the analysis, prediction and evaluation of fretting failure.
- 6) Others. Operating experience shows there are some other types of tube degradation occurring in the SG tubes, such as corrosion. There are more than twelve thousands of tubes in one SG, which are the key and weak components and are located between the primary and secondary coolant loops of NPP. They may be susceptible to flow induced vibration, wear, corrosion, seismic damage. If there is a small quantity of tubes being damaged, the method of mechanical plugging can be applied for SGs.

## VI. CONCLUSIONS

The stress analysis of NPP's Steam Generator under various loads is performed by finite element methods using the ANSYS Computer Code, such as seismic analysis,

fatigue analysis, fracture analysis, flow-induced vibration (FIV) analysis, wear analysis, and so on. The results demonstrate that the stress combination and evaluation under each service level meet the requirement of the ASME B&PVC III. In addition, the main factors affecting structure integrity and safe operation of SGs are summarized and proposed. These comments are expected to be significant for future analysis and design to ensure the safety and function of equipment and NPP. And some methods can be applied to deal with the problem of Non Conformity Report (NCR) that occurs in fabrication of equipments. Some information should be paid more attention on during the operation period of NPP.

## REFERENCES

- [1] <http://www.iaea.org/pris/>
- [2] ASME Boiler and Pressure Vessel Code. Section III. Rules for Construction of Nuclear Facility Components. New York, 2007 Edition with Addenda through 2008.
- [3] ASME Boiler and Pressure Vessel Code. Section II. Materials. New York, 2007 Edition with Addenda through 2008.
- [4] ANSYS Computer Code, "Theory Reference Manual", Release 11.0, ANSYS Inc., August 2007.
- [5] "PWR Steam Generator Tube Fretting and Wear Characteristics", TR-103506, EPRI, 1998.
- [6] N.J. Fisher, A.B. Chow, M.K. Weckwerth, "Experimental Fretting-Wear Studies of Steam Generator Materials", *Transactions of ASME*, **117**, pp 312-320, 1995.
- [7] WRCB 175 (Welding Research Council Bulletin 175), PWR Recommendations on Toughness Requirements for Ferritic Materials [S], August 1972.
- [8] Regulatory Guide 1.207, "Guidelines for evaluating fatigue analyses incorporating the life reduction of metal components due to the effects of the light-water reactor environment for new reactors", U.S. Nuclear Regulatory Commission, March 2007.
- [9] "Root Cause Analysis Report for tube wear identified in the Unit 2 and Unit 3 Steam Generators of San Onofre Nuclear Generating Station", ML13065A097, U.S. Nuclear Regulatory Commission, March 2013.
- [10] "PWR Steam Generator Tube Fretting and Fatigue Wear", NP-6341, EPRI, 1989.

## ACKNOWLEDGMENTS

The authors thank our colleagues Chang Liu and Yuanrui Ma for some analysis data and results provided by them.

**Corresponding author:** QIAN Hao. Address: Department of Component Research and Design, Shanghai Nuclear Engineering Research and Design Institute, 29 Hongcao Road, Shanghai 200233, China (E-mail: qianhao@snerdi.com.cn)

**联系作者:** 钱浩 (1982-), 男, 上海, 工程力学硕士毕业。现从事的专业: 反应堆结构力学。职称: 高级工程师

师。单位：上海核工程研究设计院工程设备所；联系地  
址：上海虹漕路 29 号 B-908，200233。电话：（021）

61860906；手机：18601728362；E-mail：  
qianhao@snerdi.com.cn。



# The US shale energy boom and the price of fossil energy

## 美国页岩能热潮和化石能源价格

Paavo Suni

The Research Institute of the Finnish Economy, ETLA, Lönnrotinkatu 4 B 00120 Helsinki, Finland

paavo.suni@etla.fi

Accepted for publication on 2<sup>nd</sup> September 2014

**Abstract** – This paper describes the birth of the US shale energy boom and its implications for the US and global fossil energy prices. The substantial rise in US shale energy production has been spurred by two major changes in energy markets. First, a strong rise in energy demand in emerging markets and particularly in China lifted the real prices of fossil energy to record highs in the early 2000s. Second, hydraulic fracturing began to be used in conjunction with horizontal drilling, which increased the productivity of energy extraction from shale formations markedly. The most visible impacts of the boom in fossil prices were seen in declines of the US crude oil and natural gas prices in relation to their international counterparts due to limited arbitrage opportunities between domestic and international markets. The indirect impacts on world fossil energy prices have come indirectly through a decrease in US imports of natural gas and a decrease in US imports of crude oil combined with higher oil product exports and exports of coal.

**Keywords** – shale, gas, crude oil, price

### I. INTRODUCTION

Global energy markets were transformed substantially in the early 2000s as China developed rapidly into one of the key economies in the world. This rise, supported by the other emerging markets, generated such a strong increase in energy demand that fossil energy markets could be balanced only by historically strong price rises [1].

The price of oil peaked in June 3 2008 at almost 150 dollars per barrel, which is 5.1-fold higher than in 2000. However, the real price of crude oil was, on average, nearly 2.5-fold higher in 2008 than in 2000.

The US natural gas and the Australian thermal coal prices peaked in October 2005 and July 2009 at 13.52 USD/mmbtu and 180 USD dollars per tonne, respectively. The huge nominal price rises implied also strong real energy prices – i.e. energy prices deflated by manufactured goods’ export prices.

The real prices of crude oil, natural gas and coal rose by 2.7-, 1.9-, and 3.7-fold up to their peaks from the year 2000. In 2013, crude oil (Brent) and thermal coal real prices were still 2.7- and 2.4-fold higher compared to prices in 2000. The real price of the US natural gas was, however, decreased to only 65 per cent of the price in the year 2000 [2] [3].

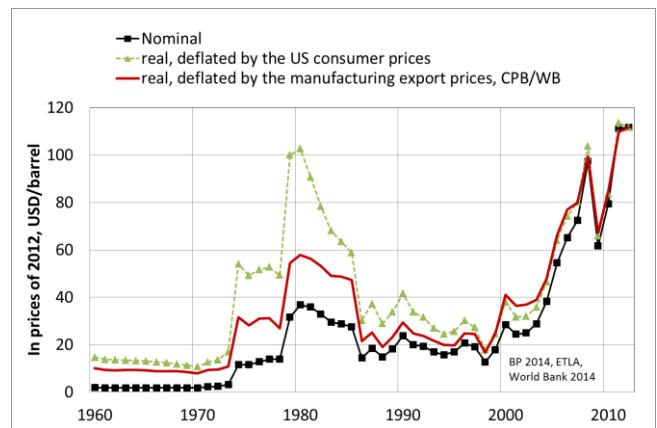


Fig.1, Real and nominal prices of crude oil (Brent)

The price rise of crude oil and natural gas in 2000-2007 was a necessary condition for the strong rise of shale production especially after 2008. Shale production took place already before the energy price rise, but in very small quantities. Rising prices and advances in drilling technology turned previously large, but unprofitable shale energy resources into profitable reserves [1]. Hydraulic fracturing combined with horizontal drilling – fracking – gives producers access to more shale oil or shale gas from relatively thin horizontal shale deposits.

There are also a number of other US-specific reasons why the shale energy boom started precisely in the US and in its neighbour Canada. Favourable geology, private land and mineral rights ownership, market structure, water availability, and pipeline infrastructure among others made the rapid rise in production possible [4].

Shale energy production is, however, expensive. The average break-even price of shale oil varies between US\$40/bbl –US\$90/bbl by resource plays [5]. The average break-even price for the shale gas production varies between \$4-5/mmbtu for the key plays [6]. Prices of WTI and natural gas were US\$102.1/bbl and 4.36 mmbtu (or per mcf) in April 2014. Shale oil is profitable with current oil prices. The case of natural gas is more complicated as much of the production is unprofitable at current prices [4].

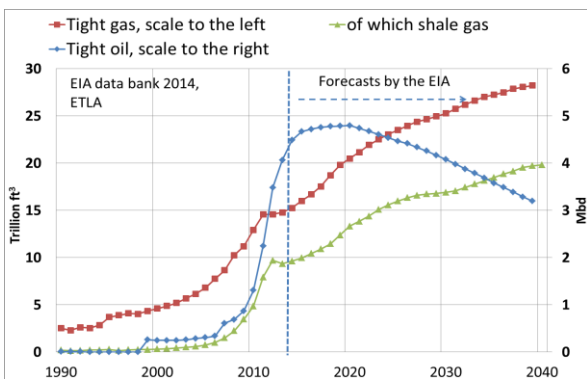


Fig.2, Tight energy production in the US

Shale energy production, i.e., tight oil production and shale gas production, picked up in the early 2000s in the US as a delayed supply response to the strong rise of the crude oil and natural gas as shown in Fig 1 and Fig 2. In this paper, we use the term ‘tight oil’ instead of ‘shale oil’ due to the statistical practice of the Energy Information Administration (EIA). The US tight oil is to a large extent shale oil, but shale gas is a separate statistical class.

TABLE 1, US SHALE ENERGY PRODUCTION

Year	Tight oil	Shale gas
	% of total crude oil production	% of total gas production
2000	4.5	1.7
2007	6.7	7.9
2008	12.3	9.8
2013	45.0	38.7
2040	42.8	52.8
Total 2013	3.48 mbd	9.35 trillion ft <sup>3</sup>
EIA 2014, ETLA		

In 2013, the US tight oil production rose 10.2- and shale gas production 6.1-fold since 2007. The production shares of total

oil and gas production of their respective total production rose to 45 and 38.7 per cent in 2013 from 6.7 and 7.9 per cent in 2007. The US technically recoverable oil and gas reserves rose by 35 and 38 per cent by the addition of tight oil and shale gas resources. [7], [8].

The shale boom has affected the US coal production indirectly due to a significant decrease of the price of gas. An increase of the relative price of coal to natural gas has led to a substitution of gas for coal in energy-consuming electricity, transportation and industrial sectors [9]. As result, the US coal exports doubled between 2007 and 2013.

These developments do not come without costs. Shale energy production techniques are not environment-friendly, which has raised a strong opposition to both production of unconventional fossil fuels and improving their logistics (e.g. the Keystone (pipeline) Project).

## II. US FOSSIL ENERGY PRICES STRONGLY AFFECTED BY SHALE ENERGY BOOM

The strong rise of production which took place in the US had a strong impact on the US oil and gas prices. The strict regulation of oil exports with a mismatch between domestic crude oil demand and supply and a lack of gas export capacity, together with a substantial rise in production, led to the overproduction in the US oil and gas markets.

The export ban of oil and gas was set in response to the oil crisis in the 1970s. The ban included countries which did not have a free trade agreement with the US. Export licensing of crude oil and especially that of natural gas are currently in the process of liberalization [10].

The US natural gas prices declined strongly in response to the very rapid rise of shale gas production Fig. 4. As a result imports also declined strongly, which has been over-compensated by the increase in domestic shale energy.

Natural gas obtained from the earth is a mixture of different hydro carbon gases, water, sand and some other minor elements. Natural gas containing primarily methane is called dry gas, while the liquefiable hydrocarbon portion is called wet gas.

The mechanics of the price development of the dry gas (Henry hub) base to a large extent on the joint production of methane and other hydro carbons. The prices of natural gas liquids (NGL) have traditionally been linked to crude oil, which has resulted in a significant price premium over pipeline-quality dry natural gas. In recent years, the relatively high value of NGLs has led producers to target wet gas, which has pushed the supply of dry gas upwards and its price downwards [11]. In addition, the dry gas producers obviously continue production in anticipation of better times [12].

The main US oils West Texas Intermediate (WTI), a marker for the US Midcontinent market, and Light Louisiana Sweet (LLS) in the Gulf coast are close substitutes for crude oil from Dubai and the global benchmark Brent. Before the shale energy boom, the price differences between these oils used to

stay close to each other with relatively small quality-based differences.

The usual price relations of the key crude oils changed markedly in response to rapidly rising US shale oil output and rising imports from Canada, which exports most of its oil and gas to the US. Before the shale boom, pipelines were usually built to carry the crude oil to Cushing in the midcontinent, but now there is a need to move the expanding shale oil flows to Gulf coast refineries.

Storage capacity and pipeline capacity were inadequate to swallow rising oil flows to land-locked Cushing, an important oil hub in the midcontinent. As result, an oversupply pushed the price of WTI to deviate from Brent and from the coastal price of the US LLS in the beginning of 2011. The price of LLS followed the price of Brent until the pipeline capacity was expanded to the Gulf coast after summer 2013 and in early 2014. Fig. 3, [13].

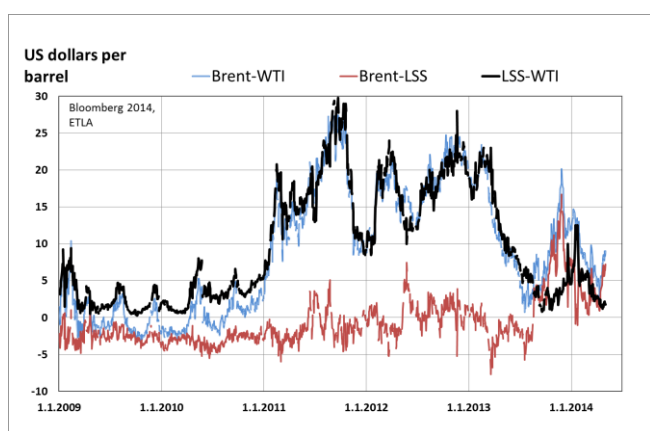


Fig.3, Brent, WTI and LLS price spreads

New transport capacity and reversals of the flows of some other pipelines to the Gulf coast shifted part of the oversupply to the coast in autumn 2013. As a result, the price differences of the US crude oils LLS and WTI were smoothed due to arbitrage and now both US prices deviated from the price of the world market benchmark Brent. This can be clearly seen in the evolution of price spreads of WTI and LLS crude oils in relation to the Brent crude. Fig. 3.

Strong decline of crude oil imports by 23 per cent from 2008 to 2013 was not able to counter the greater supply, which kept the markets oversupplied and the US prices from time to time well below the price of Brent.

The price development of the crude oil in the US is driven by the rising supply, given the decrease of imports and the demand from the US refineries for the exports of oil products and the effective export ban. The US refineries have a rather fixed configuration for the use of heavy imported oils, which restricts the decreases of imports and limits the use of domestic light oil. The US refineries have, however, benefitted from the difference of low US crude oil price and the high world market price of oil products as product exports are not banned. Exports are encouraged by implied “extra” benefits,

first for the midcontinent refineries and later, once the US prices were arbitrated close to each other, also for the other refineries.

A strong rise of the US coal exports, enabled by the substitution of gas for coal, is driven by a divergence of the US coal prices from gas prices since 2005. Fig 4. As a result, the US consumption has declined by 18 per cent in 2007-2013.

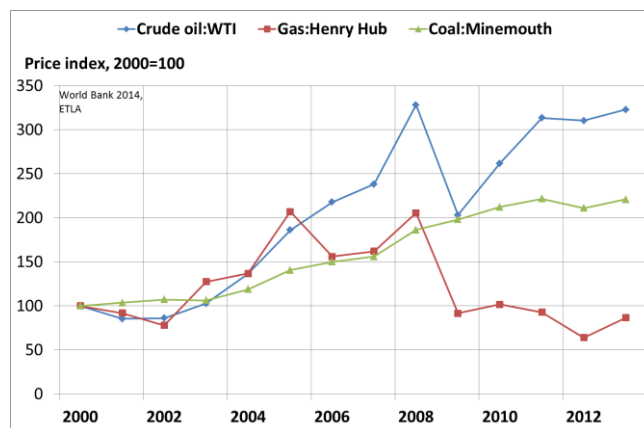


Fig 4, US fossil energy prices in the 2000's

### III. INTERNATIONAL IMPLICATIONS

The US shale energy boom took place after the dramatic price rise of global energy prices in the early 2000s. It is a good example of a reaction of global energy markets to higher prices. A supply reaction took place with a lag as oil finding, exploring and building of new sites is expensive and time-consuming. In addition, the oil producers were first cautious as the marginal costs of production in shale energy production are much higher than in conventional production.

A replication of the US shale boom is very tempting also globally as there are vast technically recoverable shale resources all across the world. The sizes of technically and economically recoverable so-called proven reserves have been estimated so far only in the US, where they cover 22 per cent of the US total crude oil proven reserves. The largest shale oil resources exist in Russia, the US, China, Argentina and Canada. The largest shale gas resources exist in China, Argentina, Algeria and the US [7] [14].

Commercially viable shale energy production, however, takes place so far notably only in the US and Canada. In China there is already some economically feasible shale gas production, but elsewhere shale energy production is mostly in a test phase. In Europe, France and Poland have the largest shale gas resources. France has, however, so far banned production due to environmental reasons, while the Polish production is still in a test phase. The main obstacle, in addition to the environmental reasons, is obviously the markedly higher marginal cost of production than in the US due to less favourable production conditions [15] [1].

So far it is the US and Canadian production which shapes the US and global energy markets. Canada is dependent on the US markets as most of its energy is exported to the US. The link between the US markets and world markets is indirect, however, as the price arbitrage is limited. Instead, a strong rise in US shale energy production affects international fossil energy prices through a decrease of the US crude oil and natural gas imports, an increase of US exports of oil products and a rise in coal exports.

Fig. 5 illustrates the evolution of world market prices of fossil energy in the 2000s. Brent crude, considered as a world benchmark, incurs downward pressure from the decrease in the US crude oil imports and higher crude oil product exports. The effect has not been strong enough to trigger a marked decrease in global oil prices. Instead the world market price of crude oil (Brent) has been remarkably stable as well since spring 2011 in spite of significant supply problems, e.g., in Iraq, Libya and Nigeria in recent years. Even the escalation of the Ukrainian crisis had only an insignificant effect on the price in spite of its potentially large effects. One of the main reasons behind the stability of the oil world market prices of crude oil is the strong rise of shale oil production in the US.

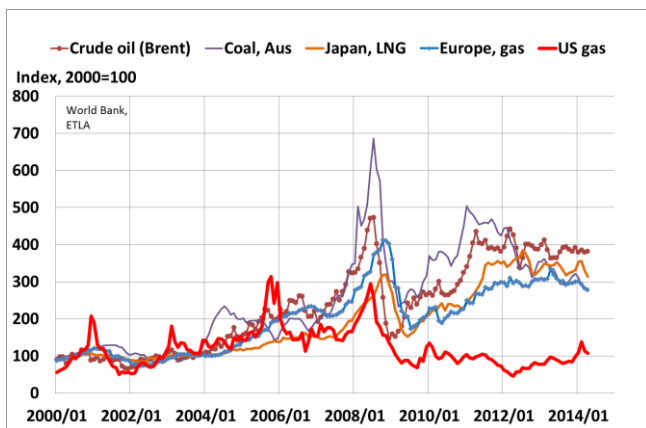


Fig 5. World energy prices in US dollars, indices, 2000=100

Obviously, in addition to the stabilization of oil prices, the shale boom, given a moderate supply policy of OPEC, has prevented a potentially sharp rise of oil prices, sparked by the recent supply problems [16].

A link between the US shale gas boom and the world markets is similar to the case of crude oil. The impact on the global markets has so far come only through rapidly decreasing imports. The global gas markets are fragmented by continent and the prices in Asia, Europe and in the US are weakly linked with a rather modest natural gas liquids (LNG) trade. The US LNG exports have been close to zero, while LNG and pipeline imports have decreased by close to 90 per cent between 2007 and 2013. Consequently, the world market share of the US LNG imports decreased to 1.5 per cent by 2012 [8] [2].

Weak world trade linkages between the continents have resulted in large price differences between the US, European and Japanese gas prices as shown in Fig. 5. In April 2014, the European import price (average) and Japanese (LNG) import price of gas prices were 2.3- and 3.2-fold higher compared with the US natural gas prices. The large differences will decline, but they are about to be rather persistent as a potentially strong increase in US export capacity is still underway and large transport costs between the continents will limit the convergence. In Europe, the average price is partly determined by the oil-linked gas from Russia.

The liberalization of the US crude oil and natural gas exports is in progress. By spring 2014, the US Department of Energy had approved five natural gas export applications and 24 more applications were in the pipeline to export gas to countries without a free trade agreement with the US. A liberalization of the US crude oil exports is still under discussion.

The liberalization of both the natural gas and crude oil exports would help in lowering the world prices of gas and crude oil. At the same time, it would obviously also raise the US prices. The liberalization would bring benefits for the US gas and crude oil producers and higher costs to the consumers, which makes decision-making politically difficult. The low profitability of gas producers and the mismatch of supply and demand of crude oil qualities - overproduction of light shale oil and a need to import heavy oil - and a potential threat of WTO procedures are pointing to more liberal policies.

#### IV. CONCLUSIONS

The US shale energy boom can be interpreted as a lagged supply response to the substantially higher energy prices of the early 2000s. A strong price rise together with a productive combination of horizontal drilling and hydraulic fracturing made shale oil and gas production profitable. The replication of the boom elsewhere has strong potential and it is under investigation. It is, however, much more challenging than in the US.

The very rapid rise of production had a strong impact on US natural gas and crude oil prices, pushing prices to diverge markedly from their foreign counterparts. The arbitrage opportunities for the deviations are limited. In the case of crude oil, the deviations depend on the difficulties to decrease US imports due to a mismatch of domestic supply and demand of crude oil qualities and the effective ban of crude oil exports.

In the case of natural gas, decreasing imports dampens the demand on the world markets, but exports to the world markets have been practically non-existent due to export controls and lack of LNG export terminals.

The substitution of cheap gas for relatively expensive coal has led to a strong rise of coal exports to alleviate coal demand outside the US.

The next move relating to the shale gas boom which affects world market prices is a relaxing of the US export controls of crude oil and natural gas. A number of licenses have already

been granted for gas exports. The effect will be seen later in full as export terminals are under construction. Also, the liberalization of crude oil export policy is under debate.

A rise of the US shale energy production and a successful liberalisation of the US energy trade will help in stabilizing the world price of energy. As a side effect, it will in a longer-run decrease the European dependency on the unreliable Russian energy supplies.

Energy will, however, stay expensive given the high marginal cost of shale energy, if the energy demand from China continues to grow and there will be no long-lasting stagnation in the world economy.

## REFERENCES

- [1] J. Chojna, M. Losoncz, P. Suni. "Shale energy shapes global energy markets", National Institute Economic Review 2013 226: F40, pp. F40-F45.
- [2] British Petroleum. "BP Statistical Review of World Energy" June 2013. Excel workbook.  
[http://www.bp.com/content/dam/bp/excel/Energy-Economics/statistical\\_review\\_of\\_world\\_energy\\_2013\\_workbook.xlsx](http://www.bp.com/content/dam/bp/excel/Energy-Economics/statistical_review_of_world_energy_2013_workbook.xlsx)
- [3] World Bank, "Pink sheets". April 2014.  
<http://go.worldbank.org/4ROCCIEQ50>
- [4] Z. Wang, A. Krupnick. "US shale gas development. What led to the boom?". Resources for the Future. Issue Brief 13-04. May 2013. pp. 1-2.
- [5] K. Mackenzie. "Is the shale forecast curve hyperbolic, or exponential?" FTAlphaville. August 21, 2013.  
<http://ftalphaville.ft.com/2013/08/21/1594492/is-the-shale-forecast-curve-hyperbolic-or-exponential/>
- [6] T. Saltvedt. "Energi och gas I vår omvard". Nordea. April 2014. p. 6.
- [7] EIA. "Technically Recoverable Shale Oil and Shale Gas Resources: An Assessment of 137 Shale Formations in 41 Countries outside the United States". June 2013.
- [8] EIA 2014 "Annual Energy Outlook 2014" Databank. Interactive data viewer.
- [9] A. Krupnick, Z. Wang, Y. Wang. "Sector Effects of the Shale Gas Revolution in the United States". Resources for the Future. RFF DP 13-20. July 2013. pp. 1-2.
- [10] T. Boersma, C. Ebinger. "Lift the Ban on U.S. Oil Exports". BIG BETS & BLACK SWANS - Memorandum to the President. January 23, 2014. Brookings. p. 1.  
<http://www.brookings.edu/research/papers/2014/01/lift-ban-us-oil-exports-boersma-ebinger>
- [11] M. Kopalek. High value of liquids drives U.S. producers to target wet natural gas resources. May 8, 2014  
<http://www.eia.gov/todayinenergy/detail.cfm?id=16191>.
- [12] M. Philips. "Is Natural Gas Too Cheap to Drill?" Bloomberg Businessweek. April 17, 2012.  
<http://www.businessweek.com/articles/2012-04-17/is-natural-gas-too-cheap-to-drill>
- [13] Green Car Congress. "EIA: planned capacity additions to US crude oil pipeline infrastructure should relieve Cushing bottleneck". February 14, 2013.  
<http://www.greencarcongress.com/2013/02/eiapipelines-20130214.html>
- [14] EIA. "Crude oil reserves at start of 2013 reach highest level since 1976". Today in Energy. April 10, 2014.  
<http://www.eia.gov/todayinenergy/detail.cfm?id=15791>
- [15] Energy Global. "A discussion of France's shale gas future". 2014.  
[http://www.energyglobal.com/news/shale-gas/articles/A\\_discussion\\_of\\_France\\_and\\_Poland\\_shale\\_gas\\_future.aspx#.U3X48Cgqg4I](http://www.energyglobal.com/news/shale-gas/articles/A_discussion_of_France_and_Poland_shale_gas_future.aspx#.U3X48Cgqg4I)
- [16] J. Hamilton. "Oil and gasoline prices: many still missing the big picture". Econbrowser April 27, 2014.  
<http://econbrowser.com/archives/2014/04/oil-and-gasoline-prices-many-still-missing-the-big-picture>



# Cytochrome c as an electron acceptor of nanostructured titania and hematite semiconductors

## 作为纳米二氧化钛和赤铁矿半导体电子受体的 细胞色素 C

Juliana C. Araújo-Chaves<sup>1</sup>, Aryane Tofanello<sup>1</sup>, César H. Yokomizo<sup>1,2</sup>, Waldemir M. Carvalho-Jr<sup>1</sup>, Flavio L. Souza<sup>1</sup> and Iseli L. Nantes<sup>1\*</sup>

<sup>1</sup>Laboratory of Nanostructures for Biology and Advanced Materials, Centro de Ciências Naturais e Humanas, Universidade Federal do ABC, Av dos Estados, 5001, Santo André-SP, Brazil

<sup>2</sup>INFAR, Departamento de Bioquímica, Universidade Federal de São Paulo, Rua 3 de Maio, 100, São Paulo-SP, Brazil.

*ihnantes@ufabc.edu.br*

Accepted for publication on 4<sup>th</sup> September 2014

**Abstract** - The use of hematite ( $\alpha$ -Fe<sub>2</sub>O<sub>3</sub>) to promote water splitting for the generation of hydrogen and molecular oxygen has gained particular interest due to its characteristics of stability, low cost, abundant precursors and a 2.1 eV band gap that allows absorption of visible light. However, some unfavorable characteristics such as fast charge recombination and band positions impairing unassisted water splitting have challenged researchers for the improvement of hematite photoanodes. In the present study, it was demonstrated that an alkaline protein, respiratory cytochrome c, interacts with the nanostructured semiconductor materials, TiO<sub>2</sub> and  $\alpha$ -Fe<sub>2</sub>O<sub>3</sub> NPs. The association of cytochrome c with the nanostructured semiconductors was corroborated by zeta potential measurements and scanning electronic microscopy. Cytochrome c is a good acceptor of the electrons promoted to the conduction bands of the semiconductors exposed to simulated sunlight. The photoreduction of cytochrome c by TiO<sub>2</sub> and  $\alpha$ -Fe<sub>2</sub>O<sub>3</sub> NPs are pH-dependent and favored at the pH range from 9-11. Despite the short lifetime of charge separation,  $\alpha$ -Fe<sub>2</sub>O<sub>3</sub> was able to promote photo-reduction of bulk and adsorbed cytochrome c detected by electronic absorption spectroscopy. Therefore, this is a model for the development of systems able to bypass the short lifetime of  $\alpha$ -Fe<sub>2</sub>O<sub>3</sub> charge separation by using efficient electron collectors as cytochrome c.

**Keywords** – cytochrome c, iron oxide, titanium oxide, electron transfer, nanostructure

## I. INTRODUCTION

Sunlight is an abundant energy ( $\sim 3 \times 10^{24}$  J yr<sup>-1</sup>) that directly and indirectly sustains the life on the Earth [1,2]. Living organisms have highly efficient apparatus to produce organic fuels by using solar energy. Photosynthesis is a redox process in which the thermodynamically unfavorable glucose synthesis by using water as the reducing agent is made feasible by collecting solar energy by chlorophyll and accessory pigments [3,4,5,6]. In the light step of photosynthesis, light energy is used for the non-spontaneous electron transport from water to reduce NADP<sup>+</sup> to NADPH. In the dark step, NADPH is recycled to NADP<sup>+</sup> and the energy is stored in the glucose molecules [3,4]. The biological fuel produced by autotrophic organisms is distributed to the heterotrophic organisms in the alimentary chain. The mimicking of photosynthesis process for the production of fuels is a challenge for a green sustaining of the global production and development. Apparatus constructed with pure and doped semiconductors placed on the surface of a conductive substrate able to absorb visible light have been largely used for sunlight harvesting [7,8]. In these mimetic apparatus, the water splitting is promoted by photoactive semiconductor materials such as TiO<sub>2</sub>, WO<sub>3</sub> and hematite. Hematite has gained particular interest due to the characteristics of high electrochemical stability, favorable band gap (2.1 eV) that allows absorption of visible light and low-cost due its abundance in Earth [9]. However some unfavorable characteristics such as short lifetime and low mobility of the photogenerated minority carriers (h<sup>+</sup>, hole) to

the liquid interface (hematite/water interface) increases the recombination rate and conduction band edge positions impairing unassisted water splitting have challenged researchers for the improvement of hematite photoanodes [9, 10, 11, 12, 13, 14, 15]. Considering the application not only in light harvesting but also in biosensing and hydrogen generation, the photo-induced redox process involving heme proteins and semiconductors has gained the interest of the researchers [16, 17, 18, 19, 20]. Interesting mechanisms involving dyes and aromatic compounds as sensitizers for hemeproteins have been described. The aromatic imide, N,N'-bis(2-phosphonoethyl)-1,4,5,8-naphthalenetetracarboxylic diimide (PNDI) and the well-known dye methylene blue are able to promote photoreduction of hemeproteins such as cytochrome c and horseradish peroxidase [13,21]. The photochemistry of systems composed of cytochrome c and titanium dioxide (TiO<sub>2</sub>), an n-type semiconductor material, has been studied using nanoporous TiO<sub>2</sub>, TiO<sub>2</sub> nanoparticles (NP) and nanotubes [22,23,24,25,26,27,28,29,30]. In a previous study, we have demonstrated the photo-induced electron transfer from water to cytochrome c promoted by two TiO<sub>2</sub> structures: P25 TiO<sub>2</sub> nanoparticles (NPs) and titanate nanotubes. P25 has low affinity for the hemeprotein but efficiently photoreduced bulk cytochrome c differently of the titanate nanotubes that exhibits high affinity for cytochrome c but photoreduced poorly the remaining non-adsorbed protein. In that study, some basic aspects leading the interaction, functional changes and the photochemistry of TiO<sub>2</sub>/cytochrome c systems were investigated by using two TiO<sub>2</sub> structures: TiO<sub>2</sub> NP and titanate nanotubes. It was demonstrated that TiO<sub>2</sub> NP and titanate nanotubes were able to promote the photo-reduction of cytochrome heme iron but with significant differences in molecular arrangements and efficiency [31]. However, due to the high costs, cheaper alternatives to the efficient semiconductors TiO<sub>2</sub> and WO<sub>3</sub> have been searched. This work describes a comparative study of the mechanisms underlying the photochemistry of cytochrome c associated to hematite and anatase.

## II. MATERIALS AND METHODS

The TiO<sub>2</sub> anatase used was the standard material Degussa P25 (Brunauer-Emmett-Teller (BET) surface area = 53.2 m<sup>2</sup> g<sup>-1</sup>), and herein, referred to as TiO<sub>2</sub> NPs (nanoparticles). All other chemicals were purchased from Sigma-Aldrich Co.. For hematite synthesis the reagents FeCl<sub>3</sub>·6H<sub>2</sub>O, NaNO<sub>3</sub>, and HCl, were of analytical grade and were not submitted to further purification.

All aqueous suspensions and solutions were prepared with deionized water (mixed bed of ion exchanger, Millipore®), and the pH was measured using a combined glass electrode (Orion Glass pH SURE-FLOW™). The reference electrode (ROSSTM, model 8102) was filled with Orion Filling Solutions (ROSSTM). The pH meter was calibrated using METREPAK pHydration standard buffer solutions (Brooklyn, NY) Chemicals.

Rat liver mitochondria were isolated by conventional differential centrifugation from the livers of adult Wistar rats. The homogenate was prepared in 250 mM sucrose, 1.0 mM EGTA, and 5.0 mM HEPES buffer (pH 7.2). The mitochondrial suspension was washed twice in the same medium containing 0.1 mM EGTA, and the final pellet was diluted in 250mMsucrose to a protein concentration of 80-100 mg/mL.[32,33,34] Mitoplasts (mitochondria devoid of the outer membrane) were prepared exactly as described by Pedersen et al. [23, 24] For spectrophotometric assays, mitochondria were incubated at 30 °C with 2.5 μM rotenone in a standard incubation medium containing 125mM sucrose, 65m MKCl, 10mM HEPES-KOH, 0.5mM EGTA, and 10 mM K<sub>2</sub>HPO<sub>4</sub> at pH 6.0 (maximal affinity of cytochrome c for cytochrome c-depleted mitoplasts.[31] Electronic absorption spectra of a mitoplast sample were obtained before and after the addition of 0.4 nmol of cytochrome c/mg of mitochondrial protein, determined according to ref. 31. The sample was placed in a bucket with a septum cap and purged with nitrogen before the first scanning and the addition of cytochrome c. After addition of cytochrome c new spectral acquisition was performed and the data loaded into the program Microcal Origin 8.5. The spectrum of cytochrome c-depleted mitoplasts was subtracted off the spectrum obtained after the hemeprotein addition.

Hematite nanoparticles were prepared by a chemical route using an aqueous solution controlled under hydrothermal conditions as previously reported.[35]

For adsorption of cytochrome c on TiO<sub>2</sub> NPs and hematite, a cytochrome c solution (10 μM (~0.125 mg mL<sup>-1</sup>) was used for direct adsorption of the protein on TiO<sub>2</sub> NPs and hematite (0.05 mg mL<sup>-1</sup>) suspension in 5 mM universal buffer, in the dark.

For irradiation of the samples, the sunlight conditions were simulated using a 450 W xenon lamp (Osram, ozone free) and an AM 1.5 filter. The light intensity was adjusted to the value of 100 mWcm<sup>-2</sup>. Here, all experiments were conducted using this fixed light intensity and the samples containing TiO<sub>2</sub> NPs and hematite were all irradiated concomitantly.

The spectra of the samples were obtained at each irradiation interval were recorded using a Thermo Scientific™ Evolution™ Array UV-Visible spectrophotometer (MA, USA). The optical path length was 0.1 cm for all measurements.

The zeta potential (ζ) measurements of zeta potential were carried out in a Zetasizer Nano ZS, Malvern Instruments, Ltd. (London, UK), at the temperature of 25 °C. The ζ is determined by the electrophoretic mobility, μ<sub>e</sub>, by the application of the Henry equation and calculated by using the Smoluchowski approximation. The ζ values are the average of 10 independent measurements that were calculated using a mono-modal model and time measurement was determined by the instrument.

The scanning electron microscopy (SEM) of the samples was carried out using a compact low vacuum electronic scanning microscopy JSM-6010LA, JEOL (Tokyo, Japan).

### III. RESULTS

Previously, it was demonstrated that TiO<sub>2</sub> (anatase) NPs adsorb cytochrome c and can promote efficient photoreduction of the protein that remained in solution [30]. Considering the crescent interest in hematite ( $\alpha$ -Fe<sub>2</sub>O<sub>3</sub>) due to the advantages described before, here, it was performed a comparative study with  $\alpha$ -Fe<sub>2</sub>O<sub>3</sub> (hematite) and TiO<sub>2</sub> (anatase). To compare the properties of hematite and anatase associated to cytochrome c, we previously investigated the effect of pH on the zeta potential ( $\zeta$ ) of bare and cytochrome c-covered semiconductor nanostructures analyzed in a 2.5 mM universal buffer adjusted to each desired pH value. Figure 1 A and B show respectively, the  $\zeta$  values of TiO<sub>2</sub> and  $\alpha$ -Fe<sub>2</sub>O<sub>3</sub> NPs, respectively. The experiments were carried out in the absence and presence of cytochrome c for both NPs.

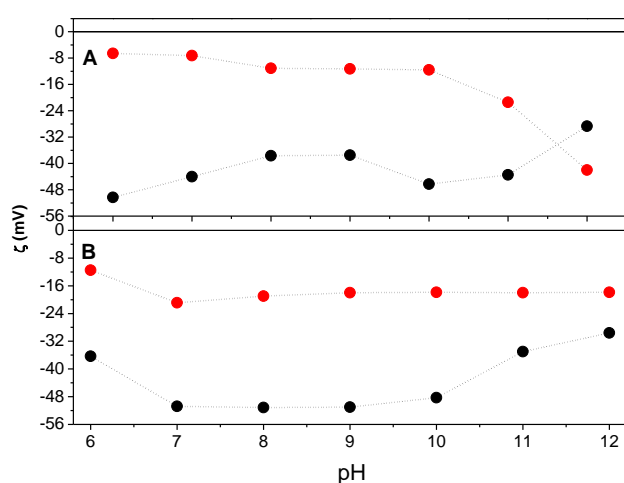
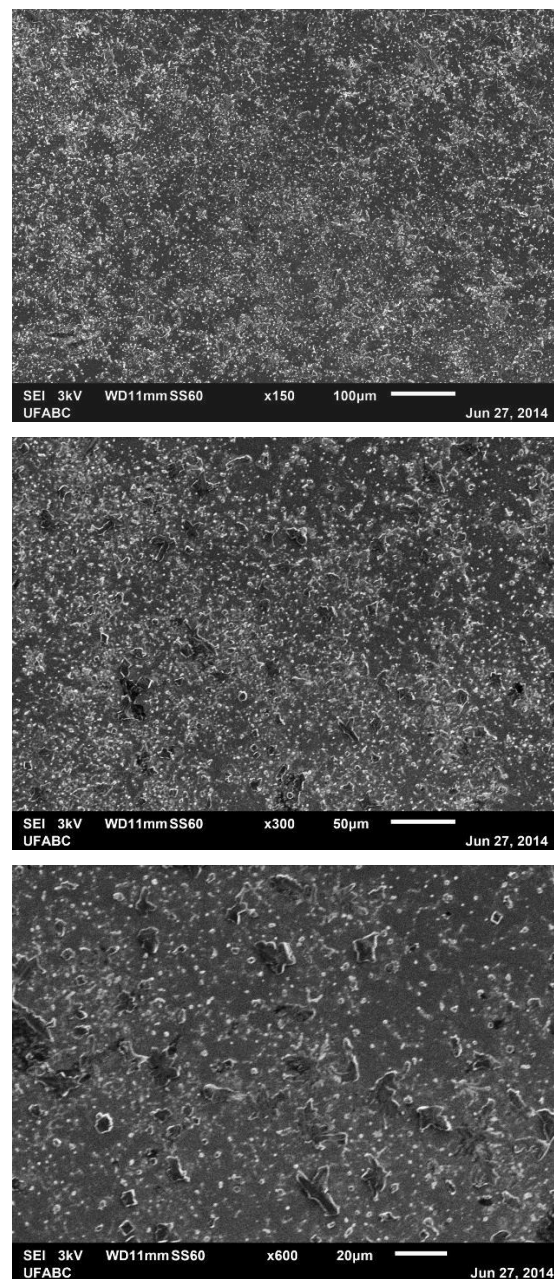


Fig. 1. The pH-dependent  $\zeta$  values of bare (black closed circles) and cytochrome c-capped (red closed circles) TiO<sub>2</sub> NPs (A) and hematite (B). The samples were prepared in 2.5 mM universal buffer (acetate, phosphate and borate).

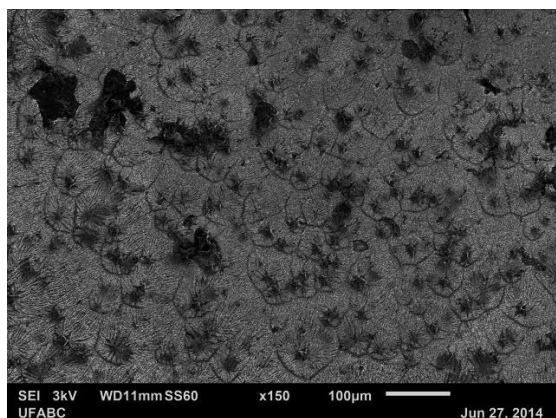
The pH-dependent curve of  $\zeta$  values, obtained for the bare oxide nanoparticles in universal buffer reflects the effects of polyprotic phosphate and boric acids present in the composition of a universal buffer. In a similar manner to that described for the use of citric acid as a buffer [36], phosphate and borate led to a negative zeta potential at the analyzed pH range. The highly negative  $\zeta$  obtained for bare TiO<sub>2</sub> at pH 6.0 suggests an effect of flocculation. Also, the significant increase of  $\zeta$  observed for bare TiO<sub>2</sub> NPs at high pH values may be assigned to disaggregation and decrease of phosphate and borate adsorption.[33] For bare  $\alpha$ -Fe<sub>2</sub>O<sub>3</sub> the  $\zeta$  values obtained at acidic pH values might reflect flocculation and even chemical modifications because the chemical instability of the material observed at pH < 7.0. Above pH 7.0, by increasing the pH,  $\alpha$ -Fe<sub>2</sub>O<sub>3</sub> gains stability and increasing  $\zeta$  values are observed at pH values  $\geq$  10.0. The pH-dependent  $\zeta$  values obtained for TiO<sub>2</sub> and  $\alpha$ -Fe<sub>2</sub>O<sub>3</sub> NPs incubated with cytochrome c are consistent with adsorption of the alkaline protein (pI = 10.2) leading to stabilization of the materials at

all the analyzed pH range [37]. The decrease of cytochrome c-treated TiO<sub>2</sub> NPs  $\zeta$  values at pH above 10 is consistent with decrease the adsorption of the hemeprotein above the pI. However, cytochrome c-treated  $\alpha$ -Fe<sub>2</sub>O<sub>3</sub> did not exhibit significant decrease of  $\zeta$  values even at pH > 10.0. This result suggests a strong interaction between the negatively charged surface of  $\alpha$ -Fe<sub>2</sub>O<sub>3</sub> and cytochrome c leading to an increase of the protein pI at the interface. Furthermore, the occurrence of other types of interactions such as hydrogen bonds between cytochrome c and  $\alpha$ -Fe<sub>2</sub>O<sub>3</sub> could not be discarded and deserves future investigations.

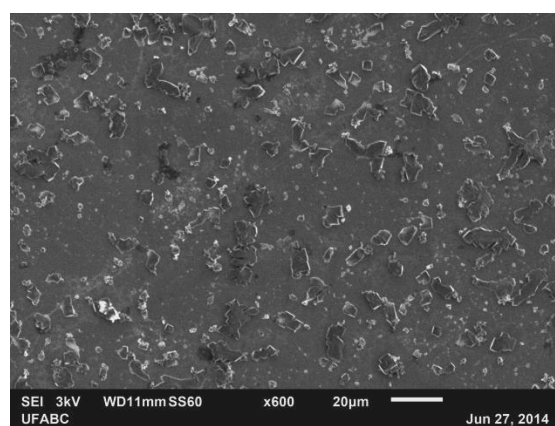
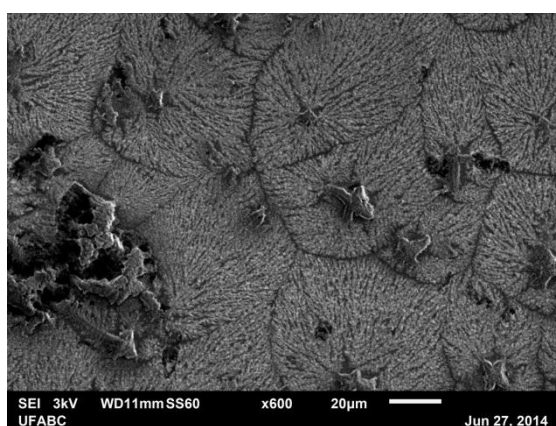
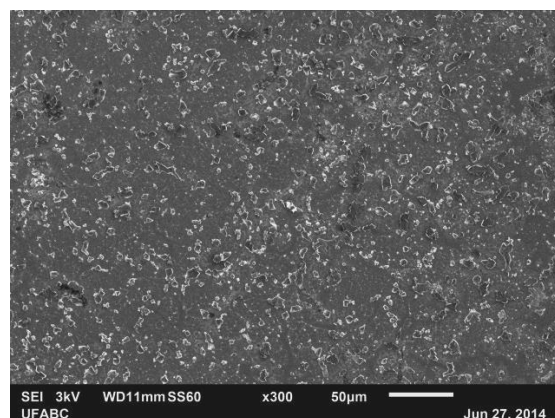
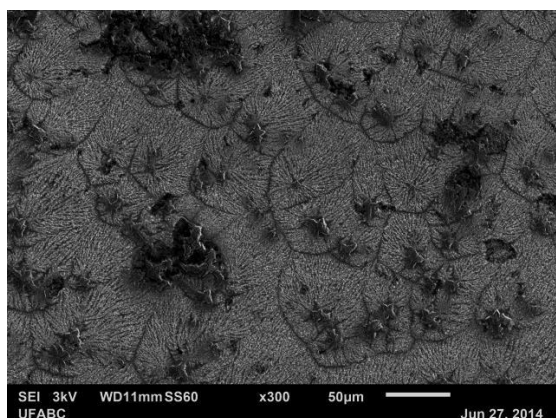
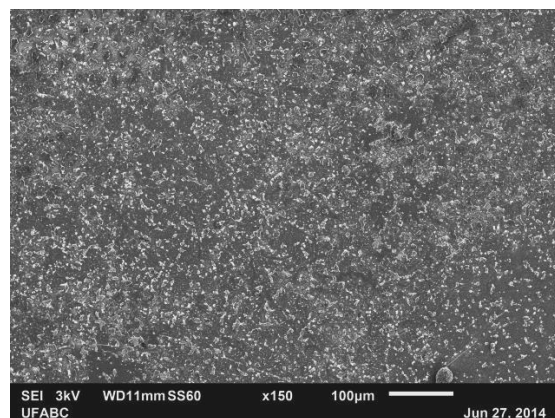
A



**B**



**C**



**D**

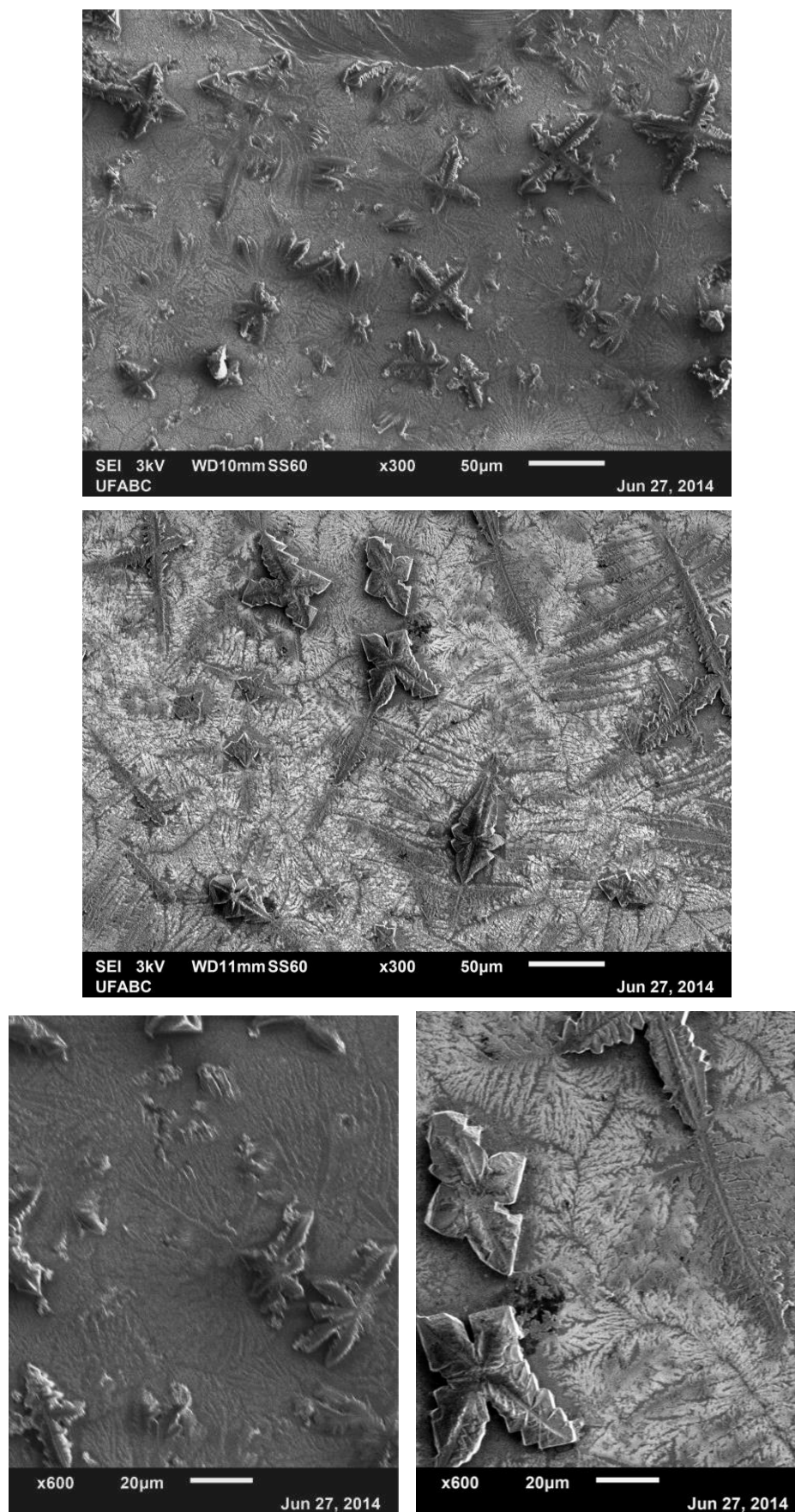


Fig. 2. SEM images of bare TiO<sub>2</sub> NPs (A) and cytochrome c-coated TiO<sub>2</sub> NPs; (B) and bare α-Fe<sub>2</sub>O<sub>3</sub>; (C) and cytochrome c-coated α-Fe<sub>2</sub>O<sub>3</sub>; (D). All the images are of the samples incubated at 2.5 mM universal buffer, pH 10.

The adsorption of cytochrome c on TiO<sub>2</sub> and  $\alpha$ -Fe<sub>2</sub>O<sub>3</sub> NPs was supported by SEM images obtained in the absence and in the presence of cytochrome c (Figure 2A, B, C and D).

SEM images of TiO<sub>2</sub> NPs, before and after incubation with cytochrome c in 5 mM universal buffer, pH 10 are shown in Fig. 2A and 2B, respectively. Figure 2A shows the presence of uneven aggregates of TiO<sub>2</sub> crystallites self-assembled and randomly distributed on the silicon surface. Fig. 2B shows that the adsorption of cytochrome c to TiO<sub>2</sub> NPs changes significantly the pattern of the material organization on the surface that may be related to the change of surface properties of the TiO<sub>2</sub> crystallites. In Fig. 2B it is shown a pattern of scales on which one can see structures with radial layout and ramification. Figure 2C shows the SEM images of hematite before incubation with cytochrome c, in 2.5 mM universal buffer, pH 10. In this condition, hematite exhibited also crystallite aggregates. Figure 2D shows that the interaction of cytochrome c on the surface of hematite particles led to extensive aggregation that creates images in relief that in some areas are similar to the branches of ferns. The ramified pattern obtained for TiO<sub>2</sub> and  $\alpha$ -Fe<sub>2</sub>O<sub>3</sub> NPs incubated with cytochrome c in 2.5 mM universal buffer at pH 10 was reproduced in the same buffer at pH 7 (not shown). However extensive aggregation and ramification were not observed for the cytochrome c-containing samples incubated in water titrated to the desired pH with HCl and NaOH (not shown). Therefore, these aggregated patterns are influenced by the ionic strength and the presence of polyprotic acids and deserves future investigations. Self-assembled aggregates of cytochrome c and titanate nanotubes had been previously demonstrated.[28] The anionic groups present on the surface of TiO<sub>2</sub> and  $\alpha$ -Fe<sub>2</sub>O<sub>3</sub> NPs promote the adsorption of the positively charged protonated amino groups of the alkaline cytochrome c [30,38,39,40]. In the case of the amino group moieties, hydrogen bonds can also be established between deprotonated group and the OH<sup>-</sup> groups on the surface of the semiconductor materials [28,37].

The effect of universal buffer (acetate, phosphate and borate) in promoting the extensive aggregation and ramified patterns for the cytochrome c TiO<sub>2</sub> and  $\alpha$ -Fe<sub>2</sub>O<sub>3</sub> aggregates is consistent with a study of Chusuei et al. [41] that described the adsorption of calcium ions on the surface of TiO<sub>2</sub> surface allowing subsequent adsorption of phosphate on the TiO<sub>2</sub>-calcium layer. Complexes of the positively charged calcium ion and phosphate with TiO<sub>2</sub> have also been described by other authors [42,43].

Considering that the interaction of cytochrome c with the semiconductor materials studied here was characterized, the next step was to investigate the behavior of the photoreduction processes in the both systems.

The capacity to accept electrons from the conduction bands of photoexcited TiO<sub>2</sub> and  $\alpha$ -Fe<sub>2</sub>O<sub>3</sub> was compared by analysis of UV-visible spectra of cytochrome c before and after irradiation in the presence of the semiconductors. Cytochrome c irradiated in the presence of TiO<sub>2</sub> and  $\alpha$ -Fe<sub>2</sub>O<sub>3</sub> NPs exhibits spectral changes typical of heme iron reduction [18]. The reduction of cytochrome c heme iron from the oxidation state

Fe<sup>3+</sup> to Fe<sup>2+</sup> is accompanied by Soret band red shift and increase of Q $\alpha$  band at 550 nm. Figure 3A shows a typical spectral change that accompanies cytochrome c reduction after 1h of exposure to UV-visible light in the presence of  $\alpha$ -Fe<sub>2</sub>O<sub>3</sub> NPs at pH 10. Similar spectral changes were obtained at similar conditions in the presence of the TiO<sub>2</sub> NPs (not shown). Figure 3B shows two differential spectra of cytochrome c obtained by subtraction of the spectrum after irradiation in the presence of  $\alpha$ -Fe<sub>2</sub>O<sub>3</sub> NPs of the initial spectrum before irradiation at pH values 10 and 11 (gray and light gray lines, respectively). Figure 3C shows the pH curve obtained from the differential spectra of cytochrome c submitted to irradiation in the presence of TiO<sub>2</sub> (blue balls) and  $\alpha$ -Fe<sub>2</sub>O<sub>3</sub> NPs (red balls) at pH 6, 7, 8, 9, 10, 11 and 12.

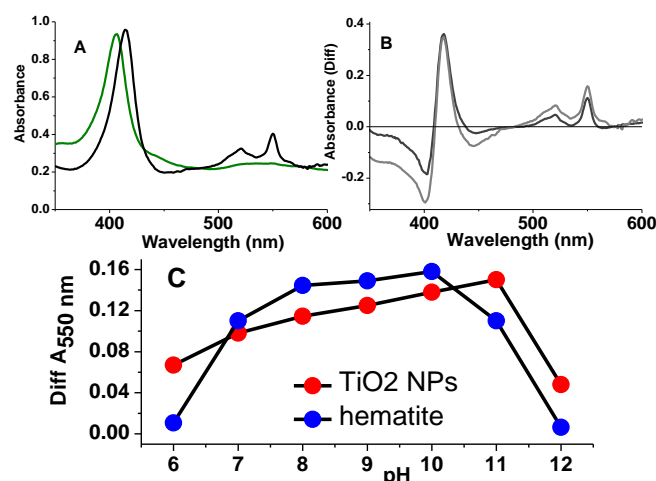


Fig. 3. Photoreduction of ferric cytochrome c by simulated sunlight simultaneous irradiation of TiO<sub>2</sub> NPs and hematite suspensions at different pH values. A- Spectra of ferric cytochrome c (olive line) and hematite-reduced cytochrome c (black line); B- Differential spectra of cytochrome c photoreduced by hematite at pH 10 (gray line) and at pH 11 (dark gray line); C- pH curves of cytochrome c photoreduction by TiO<sub>2</sub> NPs (red balls) and  $\alpha$ -Fe<sub>2</sub>O<sub>3</sub> (blue balls).

It is observed that pH 10 is the optimal pH for cytochrome c reduction by  $\alpha$ -Fe<sub>2</sub>O<sub>3</sub> NPs and pH 11, for the TiO<sub>2</sub>-promoted photoreduction. At the pH range from 8 to 10  $\alpha$ -Fe<sub>2</sub>O<sub>3</sub> NPs was able to reduce a higher amount of cytochrome c than TiO<sub>2</sub> NPs.

Previously, we have demonstrated that ferrous cytochrome c produced by titania photochemistry could be recycled to the ferric form by a solution of hydrogen peroxide [28]. In the present study ferrous cytochrome c produced by excited  $\alpha$ -Fe<sub>2</sub>O<sub>3</sub> NPs was added to a nitrogen purged suspension of cytochrome c-depleted mitoplasts. The spectrum of mitoplasts was recorded before and after ferrous cytochrome c addition (Fig. 4).

Figure 4 shows the electronic absorption spectrum obtained by subtracting the spectrum of cytochrome c-depleted mitoplasts of the spectrum obtained after addition of ferrous cytochrome c (0.4 nmol/mg mitochondrial proteins) reduced by hematite (black line). Figure 4 shows also the Soret band of ferric and ferrous cytochrome c solutions overlapped on the cytochrome c spectrum in mitoplasts. The spectrum of

cytochrome c obtained after addition to the mitoplast suspension demonstrated that the heme protein was oxidized after association to mitoplasts. The cytochrome c-depleted mitoplasts was not supplemented with succinate and nitrogen was purged in the suspension to avoid reoxidation of ferrous cytochrome c by solvated molecular oxygen. However, the possibility that ferrous cytochrome c was also oxidized by hydrogen peroxide produced by mitoplasts may not be discarded. However, even considering this possibility it was demonstrated the recycling of the heme protein by a biological system.

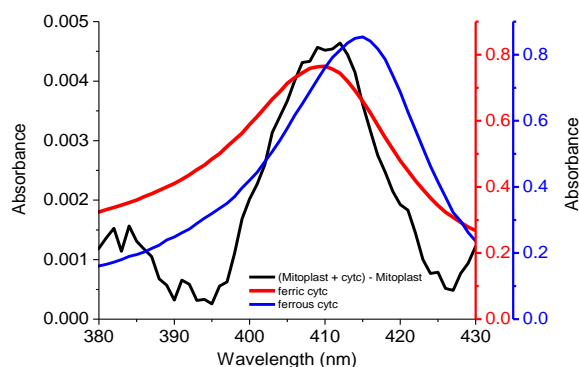


Fig. 4. Recycling of photoreduced cytochrome c. The black line is the spectrum of cytochrome c obtained after addition to a cytochrome c-depleted mitoplast suspension and obtained by subtracting the spectrum obtained before the addition of the heme protein. The red line corresponds to ferric cytochrome c before irradiation in the presence of  $\alpha\text{-Fe}_2\text{O}_3$  NPs (hematite) and blue line corresponds to the spectrum of cytochrome c after irradiation with simulated sunlight. One aliquot of the reduced cytochrome c peaking at 415 nm was added to mitoplast suspension for a final content of 0.4 nmol cytochrome c/mg mitochondrial protein. The experiments were done at pH 6.0 at 30 °C. The color of each y-axis refers to the line with the same color.

The data presented here show a piece of evidence supporting the capacity of  $\text{TiO}_2$  and  $\alpha\text{-Fe}_2\text{O}_3$  NPs to reduce ferric cytochrome c in a process that is analogous to some steps of the light step of photosynthesis. According to the redox potentials presented in Fig. 5, [44] the light absorption by the semiconductors made feasible that water acted as the reducing agent for the heme iron.

The redox potential for  $\text{TiO}_2\text{cb}$  and  $\alpha\text{-Fe}_2\text{O}_3\text{cb}$  are, respectively,  $-0.3\text{V}$  and  $-0.4\text{V}$  vs. SHE, which allows thermodynamically favorable electron transfer to ferric cytochrome c [45]. Therefore, the cytochrome/semiconductor systems are similar to the photosynthetic apparatus (left side of Fig. 4), because they use light energy to generate a high-energy electron donor for the heme iron of a cytochrome, the low energy electron acceptor. The potential values presented in Fig. 5 were extracted from literature data and may differ slightly according to the experimental conditions in which they

were determined [46]. The capacity of  $\text{TiO}_2$ , to photoreduce cytochrome c heme iron had been previously reported by our research group. However, hematite has the inconvenience of rapid charge recombination after electronic excitation and the efficient capacity to reduce cytochrome c is an advance favourable for the applicability of hematite. The  $\alpha\text{-Fe}_2\text{O}_3$  used in the present study is nanostructured, interacted with cytochrome c as demonstrated by the  $\zeta$  values and constitute a promisor system for photoelectrochemical applications.

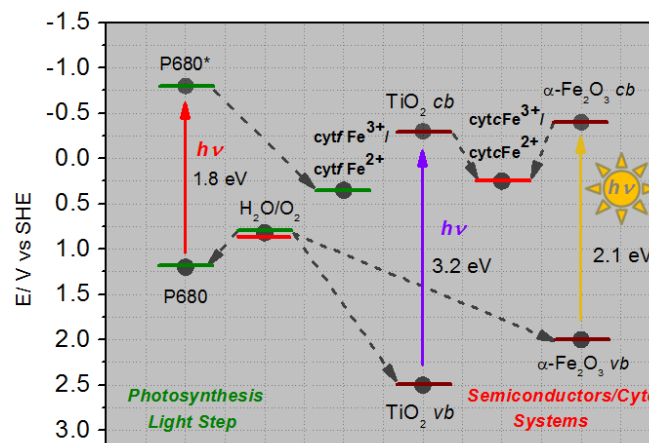


Fig. 5. Photo-reduction of cytochromes in biological and mimetic processes using semiconductors  $\text{TiO}_2$  and  $\alpha\text{-Fe}_2\text{O}_3$  NPs. The intermediate steps of the photoreduction of cytochrome f were omitted for clarity. This Figure was adapted from ref. 28.

#### IV. CONCLUSION

In this paper, it was demonstrated that an alkaline protein, respiratory cytochrome c, interacts with the nanostructured semiconductor materials,  $\text{TiO}_2$  and  $\alpha\text{-Fe}_2\text{O}_3$  NPs. Cytochrome c, in pH-dependent-manner, is a good acceptor of the electrons promoted to conduction bands of the semiconductors during exposure to simulated sunlight. Despite the short lifetime of charge separation, hematite could promote photo-reduction of bulk and adsorbed cytochrome c detected by electronic absorption spectroscopy. Therefore, this is a model for the development of systems able to bypass the short lifetime of  $\alpha\text{-Fe}_2\text{O}_3$  NPs (hematite) charge separation by using efficient electron collectors as cytochrome c.

#### ACKNOWLEDGMENTS

The authors would like to acknowledge the financial support from the Brazilian agencies FAPESP (2012/07456-7, 2013/05471-1, 2012/19926-8, and 2011/19924-2), CNPq, CAPES, CEM/UFABC and NBB/UFABC. J.C.A-C is Pos-doctoral fellow of FAPESP (2012/08322-4). The authors thanks David da Mata Lopes for the technical assistance.

#### REFERENCES

- [1] M. Gratzel. "Solar Energy Conversion by Dye-Sensitized Photovoltaic Cells," *Inorg. Chem.*, **44**, pp. 6841-6851, 2005.
- [2] M. Gratzel. "Photoelectrochemical cells," *Nature*, **414**, pp. 338-344, 2001.
- [3] R.E. Blankenship, D.M. Tiede, J. Barber, G.W. Brudvig, G. Fleming, M. Ghirardi, M.R. Gunner, W. Junge, D.M. Kramer, A. Melis, T.A. Moore, C.C. Moser, D.G. Nocera, A.J. Nozik, D.R. Ort, W.W. Parson, R.C. Prince and R.T. Sayre. "Comparing Photosynthetic and Photovoltaic Efficiencies and Recognizing the Potential for Improvement," *Science*, **332**, pp. 805-809, 2011.
- [4] P.M. Shih, J. Zarzycki, K.K. Niyogi and C.A. Kerfeld. "Introduction of a Synthetic CO<sub>2</sub>-fixing Photorespiratory Bypass into a Cyanobacterium," *J. Biol. Chem.*, **289**, pp. 9493-9500, 2014
- [5] P.G. Falkowski and J.A. Raven. *Aquatic photosynthesis*. Princeton: University Press, 2007
- [6] M. Graetzel, R.A.J. Janssen, D.B. Mitzi and E.H. Sargent. "Materials interface engineering for solution-processed photovoltaics," *Nature*, **488**, pp. 304-312, 2012.
- [7] H. Tada, M. Fujishima and H. Kobayashi. "Photodeposition of metal sulfide quantum dots on titanium(IV) dioxide and the applications to solar energy conversion," *Chem. Soc. Rev.*, **40**, pp. 4232-4243, 2011.
- [8] P.K. Santra and P.V. Kamat. "Mn-doped quantum dot sensitized solar cells: a strategy to boost efficiency over 5%," *J. Am. Chem. Soc.*, **134**, pp. 2508-2511, 2012.
- [9] S.D. Tilley, M. Cornuz, K. Sivula and M. Gratzel. "Light-Induced Water Splitting with Hematite: Improved Nanostructure and Iridium Oxide Catalysis," *Angew. Chem.*, **122**, pp. 6549-6552, 2010.
- [10] P. Dare-Edwards, J.B. Goodenough, A. Hamnett and P.R. Trevellick. "Electrochemistry and photoelectrochemistry of iron(III) oxide," *J. Chem. Soc. Faraday Trans. 1 Phys. Chem. Condensed Phases*, **79**, pp. 2027-2041, 1983.
- [11] J.B. Goodenough. "Bond-length fluctuations in the copper-oxide superconductors," *Prog. Solid State Chem.*, **5**, pp. 145-399, 1971.
- [12] C. Santato, M. Ulmann, and J. Augustynski. "Photoelectrochemical Properties of Nanostructured Tungsten Trioxide Films," *J. Phys. Chem. B.*, **105**, pp. 936-940, 2001.
- [13] W.M. Carvalho Jr., F.L. Souza. "Recent advances on solar water splitting using hematite nanorod film produced by purpose built materials", *J. Materials Research*, **29**, pp. 16-28, 2014.
- [14] V.A.N. Carvalho, R.A.S. Luz, B.H. Lima, F.N. Crespilho, E.R. Leite, and F.L. Souza. "Highly oriented hematite nanorod arrays for photoelectrochemical water splitting", *Journal of Power Sources*, **205**, pp.525-529, 2012.
- [15] L.C.C. Ferraz, W.M. Carvalho Jr., D. Criado, and F.L. Souza. "Vertically oriented iron oxide films produced by hydrothermal process: effect of thermal treatment on the physical chemical properties", *ACS Appl. Materials and Interface*, **4**, pp.5515-5523, 2012.
- [16] V.A. Soares, D. Severino, H.C. Junqueira, I.L.S. Tersariol, C.S. Shida, M.S. Baptista, O.R. Nascimento and I.L. Nantes. "Light-driven horseradish peroxidase cycle by using photo-activated methylene blue as the reducing agent," *Photochem. Photobiol.*, **83**, pp. 1254-1262, 2007.
- [17] M.J.B. Hauser, A. Lunding and L.F. Olsen. "On the role of methylene blue in the oscillating peroxidase-oxidase reaction," *Phys. Chem. Chem. Phys.*, **2**, pp. 1685-1692, 2000.
- [18] Carson and J. Walleczek. "Response of the peroxidase-oxidase oscillator to light is controlled by MB $\beta$ -NADH photochemistry," *J. Phys. Chem. B.*, **107**, pp. 8637-8642, 2003.
- [19] I.B. Campos, I.L. Nantes, F.A. Rodrigues and S. Brochsztain. "Photoinduced electron transfer in silica-supported self-assembled thin films containing a 1, 4, 5, 8-naphthalenetetracarboxylic diimide and cytochrome c," *J. Mater. Chem.*, **14**, 54-60, 2004.
- [20] K.M. Figueiredo, R.O. Marcon, I.B. Campos, I.L. Nantes and S. Brochsztain. "Photoinduced electron transfer between cytochrome c and a novel 1,4,5,8-naphthalenetetracarboxylic diimide with amphiphilic character," *J. Photochem. Photobiol. B*, **79**, pp. 1-9, 2005.
- [21] M.L. Estevam, O.R. Nascimento, M.S. Baptista, P. Di Mascio, F.M. Prado, A. Faljoni-Alario, M.R. Zucchi and I.L. Nantes. "Changes in the spin state and reactivity of cytochrome C induced by photochemically generated singlet oxygen and free radicals," *J. Biol. Chem.*, **279**, pp. 39214-39222, 2004.
- [22] E. Topoglidis, T. Lutz, J.R. Durrant and E. Palomares. "Interfacial electron transfer on cytochrome-c sensitised conformally coated mesoporous TiO<sub>2</sub> films," *Bioelectrochemistry*, **74**, pp. 142-148, 2008.
- [23] G.K. Mor, K. Shankar, M. Paulose, O.K. Varghese and C.A. Grimes. "Use of highly-ordered TiO<sub>2</sub> nanotube arrays in dye-sensitized solar cells," *Nano Letters*, **6**, pp. 215-218, 2006.
- [24] J. H. Park, S. Kim and A.J. Bard. "Novel Carbon-Doped TiO<sub>2</sub> Nanotube Arrays with High Aspect Ratios for Efficient Solar Water Splitting," *Nano Letters*, **6**, pp. 24-28, 2006.
- [25] E. Topoglidis, Y. Astuti, F. Duriaux, M. Gratzel and J.R. Durrant. "Direct electrochemistry and nitric oxide interaction of heme proteins adsorbed on nanocrystalline tin oxide electrodes," *Langmuir*, **19**, pp. 6894-6900, 2003.
- [26] Y. Astuti, E. Palomares, S.A. Haque and J.R. Durrant. "Triplet state photosensitization of nanocrystalline metal oxide electrodes by zinc-substituted cytochrome c: application to hydrogen evolution," *J. Am. Chem. Soc.*, **127**, pp. 15120-15126, 2005
- [27] E. Topoglidis, C.J. Campbell, E. Palomares and J.R. Durrant. "Photoelectrochemical study of Zn cytochrome-c immobilised on a nanoporous metal oxide electrode" *Chem. Commun.*, **14**, pp. 1518-1519, 2002.
- [28] E. Topoglidis, A.E.G. Cass, G. Gilardi, S. Sadeghi, N. Beaumont and J.R. Durrant. "Protein adsorption on nanocrystalline TiO films: a novel immobilisation

- strategy for bioanalytical devices”, *Anal. Chem.*, **70**, pp. 5111-5113, 1998
- [29] P. Cuendet and M. Gratzel. “Light-induced reduction of cytochrome c by colloidal TiO<sub>2</sub>,” *Bioelectrochem. Bioenerg.*, **16**, pp. 125-133, 1986.
- [30] E. Topoglidis, T. Lutz, R.L. Willis, C.J. Barnett, A.E.G. Cass and J.R. Durrant. “Protein adsorption on nanoporous TiO<sub>2</sub> films: a novel approach to studying photoinduced protein/electrode transfer reactions,” *Faraday Discuss.*, **116**, pp. 35-46, 2000.
- [31] C.F.B. Dias, J.C. Araújo-Chaves, K.C.U. Mugnol, F.J. Trindade, O.L. Alves, A.C.F. Caires, S. Brochsztain, F.N. Crespilho, J.R. Matos, O.R. Nascimento and Iseli L Nantes. “Photo-induced electron transfer in supramolecular materials of titania nanostructures and cytochrome c,” *RSC Advances*, **2**, pp. 7417-7426, 2012.
- [32] P.L. Pedersen, J.W. Greenalwalt, B. Reynafarje, J. Hullihen, G.L. Decker, J.W. Soper and E. Bustamante. “Preparation and characterization of mitochondria and submitochondrial particles of rat liver and liver-derived tissues,” *Methods Cell Biol.*, **20**, pp. 411–481, 1978.
- [33] R. Radi, K.M. Bush and B.A. Freeman. “The role of cytochrome c and mitochondrial catalase in hydroperoxide-induced heart mitochondrial lipid peroxidation,” *Arch. Biochem. Biophys.*, **300**, pp. 409–415, 1993
- [34] C. Kawai, F.S. Pessoto, T. Rodrigues, K.C.U. Mugnol, V. Tortora, L. Castro, V.A. Milicchio, I.L.S. Tersariol, P. Di Mascio, R. Radi, A.M. Carmona-Ribeiro and Iseli L. Nantes. “pH-Sensitive Binding of Cytochrome c to the Inner Mitochondrial Membrane. Implications for the Participation of the Protein in Cell Respiration and Apoptosis,” *Biochemistry*, **48**, pp. 8335–8342, 2009.
- [35] A.M. Xavier, F.F. Ferreira and F.L. Souza. “Morphological and structural evolution of one dimensional hematite nanorods” *RSC Advances*, **4**, pp. 17753-17759, 2014.
- [36] D. Hanaor, M. Michelazzi, P. Veronesi, C. Leonelli, M. Romagnoli, C. Sorrell. “Anodic Aqueous Electrophoretic Deposition of Titanium Dioxide Using Carboxylic Acids as Dispersing Agents,” *J. Eur. Ceram. Soc.*, **31**, pp. 1041-1047, 2011.
- [34] Moore and G.W. Pettigrew. *Cytochrome c*, Heidelberg: Springer-Verlag, 1990.
- [38] H.-C. Chang. “Adsorption and Immobilization of Cytochrome c on Nanodiamonds,” *Langmuir*, **20**, pp. 5879-5884, 2004.
- [39] M. Meot-Ner. “The ionic hydrogen bond and ion solvation. 1. NH<sup>+</sup>···O, NH<sup>+</sup>···N, and OH<sup>-</sup>···O bonds Correlations with proton affinity. Deriations due to structural effects,” *J. Am. Chem. Soc.*, **106**, pp. 1257-1264, 1984
- [40] M. Meot-Ner, L.W. Sieck, J.F. Liebman and S. Scheiner. “Complexing of the Ammonium Ion by Polyethers. Comparative Complexing Thermochemistry of Ammonium, Hydronium, and Alkali Cations,” *J. Phys. Chem.*, **100**, pp. 6445–6450, 1996
- [41] C.C. Chusuei, D.W. Goodman, M.J. Van Stipdonk, D.R. Justes, K.H. Loh and E.A. Schweikert. “Solid-Liquid Adsorption of Calcium Phosphate on TiO<sub>2</sub>,” *Langmuir*, **15**, pp. 7355-7360, 1999.
- [42] T.K. Ronson and A.J. McQuillan. “Infrared spectroscopic study of calcium and phosphate ion coadsorption and of brushite crystallization on TiO<sub>2</sub>,” *Langmuir*, **18**, pp. 5019-5022, 2002.
- [43] H. Jézéquel and K.H. Chu. “Enhanced adsorption of arsenate on titanium dioxide using Ca and Mg ions,” *Environmental Chemistry Letters*, **3**, pp. 132–135, 2005.
- [44] A. Grimes, O.K. Varghese and S. Ranjan. *Light, Water, Hydrogen: The Solar Generation of Hydrogen by Water Photoelectrolysis*, US, Springer, 2008.
- [45] A. Fujishima, T.N. Rao and D.A. Tryk. “Titanium dioxide photocatalysis,” *J. Photochem. Photobiol. C: Photochemistry Reviews*, **1**, pp. 1–21, 2000.
- [46] P. Wardman. “Reduction Potentials of One-Electron Couples Involving Free Radicals in Aqueous Solution,” *J. Phys. Chem. Ref. Data*, **18**, 1637-, 1989.



# Design and development of proton exchange membrane fuel cell using open pore cellular foam as flow plate material

## 采用开孔多孔泡沫作为导流板材料设计与开发 质子交换膜燃料电池

A. Baroutaji<sup>1\*</sup>, J. G. Carton<sup>1</sup>, J. Stokes<sup>1</sup>, A. G. Olabi<sup>2</sup>

<sup>1</sup>Manufacturing and Mechanical Engineering, Dublin City University, Dublin 9, Ireland

<sup>2</sup>Faculty of Science & Technology, University of the West of Scotland, Paisley, Scotland

[ahmad.baroutaji2@mail.dcu.ie](mailto:ahmad.baroutaji2@mail.dcu.ie)

Accepted for publication on 6 September 2014

**Abstract-** This paper reports the design and development of a Proton Exchange Membrane (PEM) fuel cell using open pore cellular metal foam as the flow plate material. Effective housing designs are proposed for both hydrogen and oxygen sides and through the application of Computational Fluid Dynamic (CFD) modelling and analysis techniques the flow regime through the open pore cellular metal foam flow plate are identified.

Based on the CFD results the best anode housing design was selected and manufactured. The fuel cell was assembled and tested and the findings are reported.

**Keyword-** Proton Exchange Membrane, Fuel Cell, Open Pore Cellular Foam, Flow Plate.

### I. INTRODUCTION

Fuel cells are devices that produce electricity through a chemical reaction between a fuel and an oxidant. Their high efficiency and low environmental impact have made them a promising alternative to conventional power sources. Fuel cells already have applications in, but are candidates to revolutionise, the transport, stationary power, and electronic industries. Different types of fuel cells have been developed over the last few decades such as Alkaline fuel cell (AFC), Direct Methanol fuel cell (DMFC), Phosphoric Acid fuel cell (PAFC), Molten Carbonate fuel cell (MCFC), Solid Oxide fuel cell (SOFC) [1,2], and Proton Exchange Membrane (PEM) fuel cell. PEM fuel cells are low temperature fuel cells that use a solid polymer in the form of a solid phase proton conducting membrane as an electrolyte. PEM fuel cells have many advantages over the other fuel cell types; including low temperature operation, high power

density, fast start up, system robustness, flexibility of fuel type (with reformer) and reduced sealing, corrosion, shielding or leaking concerns [3]. A conventional PEM fuel cell consists of a Membrane Electrode Assembly (MEA), which contains a proton exchange membrane, an electrically conductive porous Gas Diffusion Layer (GDL) and an electro-catalyst layer, sandwiched between two flow plates. A conventional flow plate has flow channels that distribute the fuel and oxidant to the reactive sites of the MEA. One of the key strategies for improving the performance of the PEM fuel cell is the effective design of the flow plate. The efficient distribution of the fuel and oxidant to the catalyst layer, can increase the utilization of catalyst, improve the water management through the cell and provide effective collection of the produced current [23]. Various designs for the flow field were proposed by the researchers including pins, straight channels, serpentine channels [4], integrated channels, interdigitated channels [5, 6] and bio-inspired flow fields [7]. A detailed review for all flow field configurations was introduced by Manso et al. [8]. The various types of flow channels have common drawbacks such as; large pressure losses, high cost of manufacturing and low mechanical strength; which increase the weight and volume of the fuel cell. In addition, the flow channels can cause unequal distribution of the electrochemical reactions which lead to irregular utilization of the catalyst [9].

As an alternative to conventional flow plates, researchers [9-12] have identified that Open Pore Cellular Foam (OPCF) materials can provide several advantages over the conventional flow plates such as better gas flow through the fuel cell, lower pressure drop from inlet to outlet.

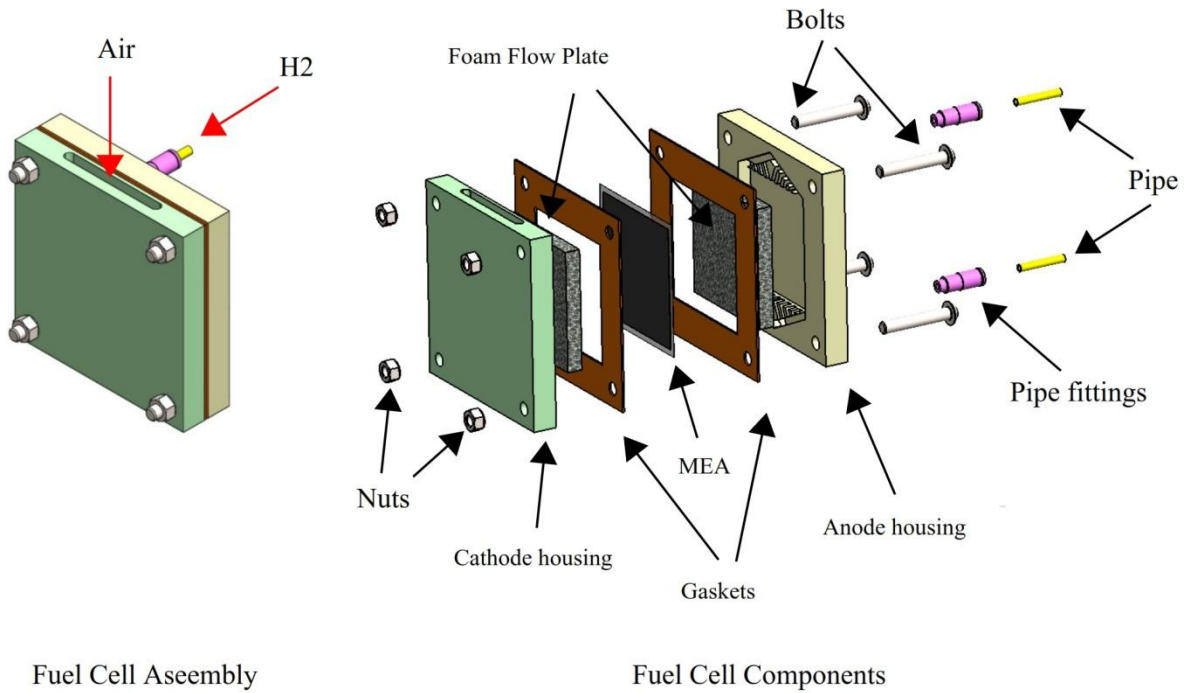


Fig 1: PEM fuel cell components and assembly

It was identified by Tsai et al. [10] that the flow field with metal foam has an impact on the performance of the PEM fuel cell. The authors completed an experimental programme to study the effect of flow field design on the performance of a PEM fuel cell. The authors concluded that the flow field can play a key role in the design and development of PEM fuel cells with either conventional or foam flow plates. In many experiments however, researchers have placed foam materials in the channels of conventional flow plates, as completed by Kumar & Readdy [21]. This retrofitting of a flow plate is crude and may not allow for the full benefits of OPCF materials to be exploited.

In spite of these advantages an effective flow plate design has not been well enough developed to allow foam materials to be effectively housed inside PEM fuel cells. New tailored housings with the required data, such as pressure analysis, flow regimes and velocity profiles have not been gathered.

In conventional flow plates the flow behaviour of oxygen and hydrogen inside the fuel cell and through the flow plates can be effectively predicted and analysed by employing the Computational Fluid Dynamic (CFD) modelling tool. Many researchers [13-20] employed the CFD tool in their studies to develop and optimize the bipolar flow plates. Detailed information about the flow regime is provided by the CFD simulations such as flow distribution, pressure pattern, and pressure drop. This information can aid in the geometric design of flow plates and flow fields and their suitability for a PEM fuel cell.

Generally speaking, the uniform flow distribution of oxygen or hydrogen and pressure over the GDL is an essential requirement in the PEM fuel cell to insure the balanced use of catalyst and thus achieving a better cell performance. The conventional flow plates deliver and distribute the hydrogen and oxygen/air to the reactive sites of the MEA via channels. The flow distribution across these channels can easily be identified using the CFD analysis and through inspecting the pressure and velocity field along the flow plate as completed by [15, 19-20].

In the present paper, a PEM fuel cell with using an OPCF flow plate, with suitable manifolding was designed and developed. Several manifold designs were proposed and tested numerically using CFD analysis. The most effective design is identified to improve the fuel cell performance. The fuel cell is prepared and tested, with the experimental results and performance reported.

## II. MODELLING AND SIMULATIONS

### 2.1 Fuel cell design

In the current study, the conventional flow plates are replaced with metal foam flow plates. Two different housings were designed to accommodate the foam flow plates on the anode and cathode sides.

The OPCF on the cathode side is air breathing allowing air convection from the surrounding atmosphere. The OPCF on the anode side is supplied with pressurised hydrogen through appropriate fittings, and gaskets are used to seal the cell. All components are assembled together using bolts

with nuts. The use of metal foam eliminated the need for some supplementary components such as current collectors which used with the conventional flow plate. Fig 1 shows the fuel cell components and final assembly.

### 2.2 3-D CFD modelling

Many designs of the anode housing were suggested in the current study to provide the adequate flow of hydrogen to the OPCF and the MEA. All of the proposed housing designs have manifold channels to deliver the hydrogen to OPCF as shown in Fig 2.

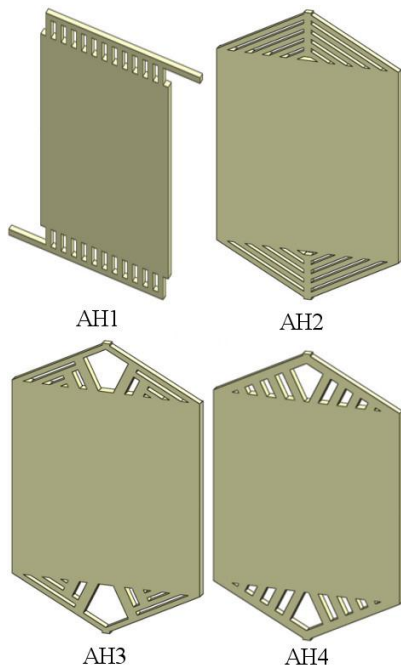


Fig 2: Anode housing flow configurations.

Computational Fluid Dynamic (CFD) techniques through FLUENT software were used to analyse effective housing designs. Since the electrochemical reaction in a PEM fuel cell requires low flow rates of oxygen and hydrogen in the flow plates, the single-phase, steady state, laminar flow module in FLUENT was used to perform the flow simulations. The laminar flow module was also used by researchers [15, 20, and 22].

The model was imported into the commercial software and boundary conditions, as shown in

Table 1, were applied. The mesh used hybrid elements by specifying the minimum edge length, Fig 3. The final models contained between 30,000 and 50,000 elements course enough not to exceed the limit or computational power or time available but fine enough to give acceptable results, clarified by grid independence analysis.

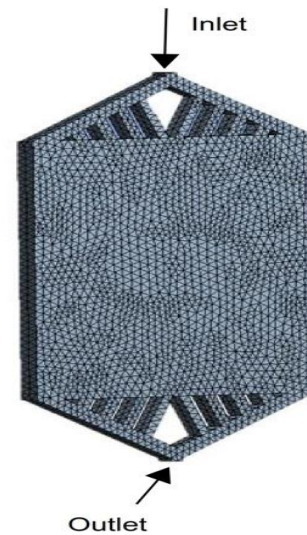


Fig 3: The CFD model mesh with flow region

TABLE 1: SIMULATION PARAMETERS & BOUNDARY CONDITIONS

Modeller	Ansys DM
Mesher	Ansys Meshing
Mesh	Mixed Tet & Quad
Size function	Fixed
Smoothing	Medium
Transition	Slow
Elements	37,997
Solver	Fluent 3-D Double Precision
Solver type	Pressure based
Model flow	Laminar
Fluid	Hydrogen
Solid (walls)	Aluminium
Temperature	Constant
Porous GDL	N/A
Inlet velocity (m/s)	1
Pressure outlet (Pa)	0 (relative)
Scheme	Simple
Gradient	least squares cell based
Pressure	Standard
Momentum	Power law
Compute from	Inlet
Monitors	Mass flow Continuity Velocity
Iterations	150

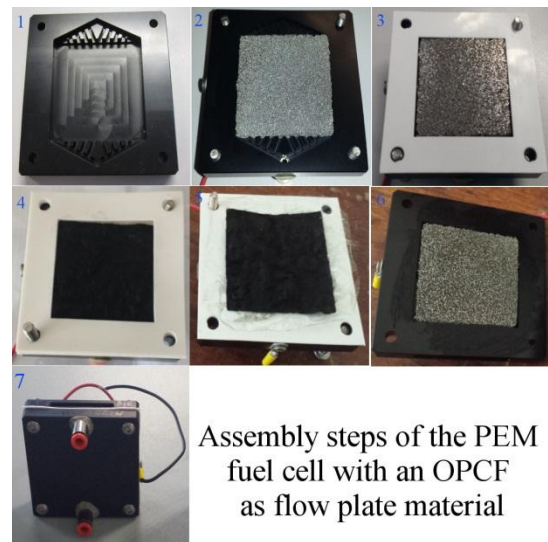
### III. EXPERIMENTS

#### 3.1 Material and assembly

Table 2 summarises the material properties of the fuel cell components used in this study and Fig 4 shows the assembly steps of the PEM fuel cell. The optimised OPCF flow plate housing was machined and wiped thoroughly using isopropyl alcohol to ensure that the housing is clean and no dust or grease present. The flow plate housing is placed horizontally in a flat position. OPCF was polished using silicon carbide grinding paper on a polishing wheel. The OPCMF is placed inside the housing and bolts are placed through the housing as shown in Fig 4, photo 2. A gasket is then placed into position as shown in Fig 4, photo 3. The MEA is positioned onto the housing as shown in Fig 4, photo 4. A second gasket is then placed onto the MEA as shown in Fig 4, photo 5. A second OPCF flow plate is placed into a second housing as shown in Fig 4, photo 6. The second housing is then placed onto the bolts of the first housing. The MEA and gasket positions are checked and both housings are closed. Nuts are placed on the bolts and they are tightened. The push-in fittings for hydrogen pipes are placed in their positions. The final assemble fuel cell is shown in Fig 4, photo 7.

TABLE 2: MATERIAL PROPERTIES OF THE FUEL CELL COMPONENT

Fuel cell component	material	Properties
OPCF housing	Acetal	Supplier: Impact Ireland
MEA	Nafion 212	active area: 5×5 (cm*cm), Catalyst loading: 0.4mg/cm <sup>2</sup> Pt/C, GDL: Sigracet SGL 24BC, 0.55g.cm <sup>-3</sup> Bulk density. Supplier: EES ltd UK
Flow plate	OPCMF	24 Pores/cm , thickness: 6.35 (mm)
Gaskets	Silicon	Thickness: 0.8 (mm)



Assembly steps of the PEM fuel cell with an OPCF as flow plate material

Fig 4: Assembly steps of the PEM fuel cell

#### 3.2 Experimental set-up and procedure

The experimental setup is similar to Carton & Olabi [23]. The reactant gas, hydrogen, is stored in a compressed cylinder. A specialised hydrogen pressure controls the hydrogen gas flow pressure. The gas then passes through volumetric flow meters. The flow controllers are calibrated for the hydrogen gas and air. The flow controllers are controlled by the data acquisition (DAQ) software (Lab View). Both air and hydrogen gases were humidified as stated by the manufacturer of the MEA. The open circuit voltage and the fuel cell operating voltage are detected by the DAQ hardware and analysed through the software. The open circuit voltage reading is also double checked at the anode and cathode using a multimeter (Fluke 8808A digital multimeter). The fuel cell current is measured using a multimeter (Fluke 8808A digital multimeter) in series with the external load.

Every effort was made to keep parameters constant during the experiments to ensure that the values of resistance, pressure and flow were not changed from one experiment to the next. These parameters were checked throughout the experiment to identify any unwanted errors. The only effect on the performance was that of the flow plate design.

IV.RESULTS AND DISCUSSION

4.1 Analysis of the anode housing configurations

As mentioned in the introduction, the optimisation and analysis of various flow field configurations can be carried out through the analysis of velocity, flow regimes and pressure distribution. The optimal design should provide an even flow and pressure distribution over the GDL and minimised pressure drop from inlet to outlet.

4.2 Anode housing design 1 (AH1)

The AH1 configuration is shown in Fig 2. This design was created to allow flow spread over the OPCF through many channels which are perpendicular to the main inlet channel. The downstream collector was designed similarly to upper collector.

Fig 5(a) shows the pressure distribution through the AH1 model, which indicates that there is a high inlet pressure and low out put pressure but even pressure distribution along the central region of the flow plate, corresponding to where the OPCF is housed. This even pressure is promising but the fluid flow velocity in Fig 5(b) may be an issue for this flow plate design. Fluid flow is confined by the channels and therefore there may be an increased possibility that low flow regions exist to the right and left side of the flow plate. This can cause possible dead zones and water accumulation as shown by Carton et al. [24]. This could dramatically reduce the performance of the fuel cell as only about one third of the active area of the cell would have convective air flow.

4.3 Anode housing design 2 (AH2)

The AH2 configuration is shown in Fig 2. The main inlet and outlet are aligned to the center of the design. The flow is designed to spread through the OPCF through many channels which are diagonal to the main inlet channel. Fig 6(a) shows the pressure distribution through the AH2 model. The pressure distribution is even with only a low pressure drop from inlet to outlet.

The velocity profile through this housing is shown in Fig 6(b). A low velocity is noticed at the inlet when compared to other designs, as flow travels straight through this design with few restrictions by the channels. Large eddy currents are also noticed while the edges of the flow plate have minimal flow, that may correspond to stagnant flow areas where water may accumulate and the effective active area of the MEA could be reduced. This could dramatically reduce the performance of the fuel cell.

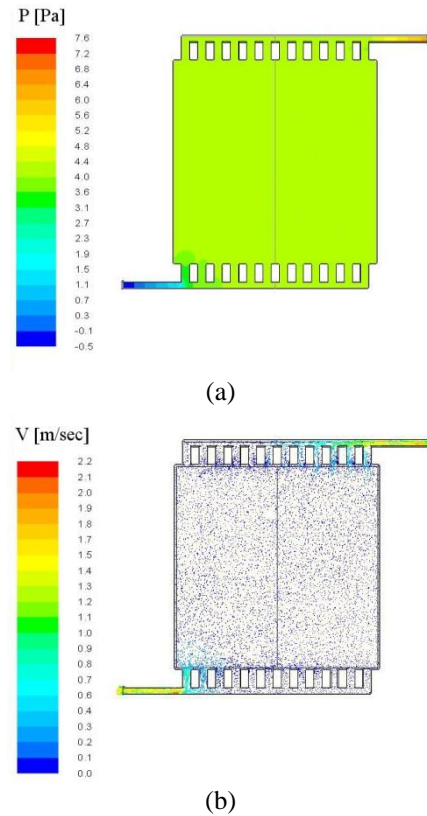


Fig 5: Numerical simulation results of AH1: (a) - Pressure distribution (pa), (b) - Velocity vectors (m/s)

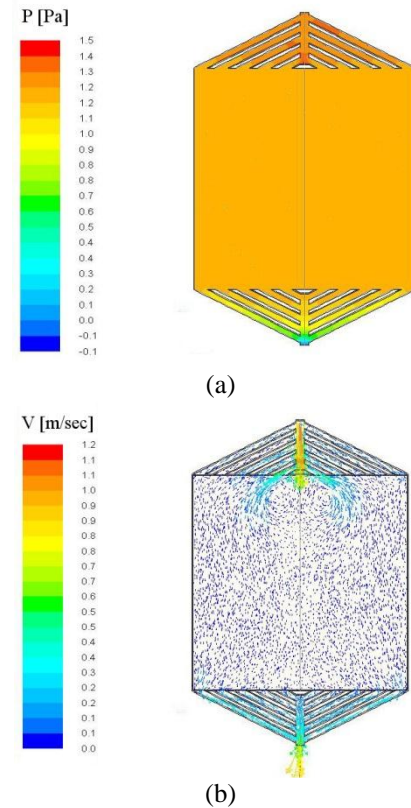


Fig 6: Numerical simulation results of AH2: (a) - Pressure distribution (pa), (b) - Velocity vectors (m/s)

4.4 Anode Housing Design 3 (AH 3)

The AH3 configuration is shown in Fig 2. This design has an obstruction placed close to the inlet which aims to split the flow into two branches. The design is aimed to then split that flow and spread over the foam material.

Fig 7 (a) shows the pressure distribution through the AH3 model. The pressure distribution is even with only a low pressure drop from inlet to outlet. The velocity profile through this housing is shown in Fig 7(b). The distribution of velocity flow is more even than previous models however large eddy currents are also noticed creating dead zones, that may correspond to stagnant flow areas where water may accumulate as demonstrated by Carton & Olabi [24], reducing the effective active area of the MEA. This design was unsuccessful and could dramatically reduce the performance of the fuel cell.

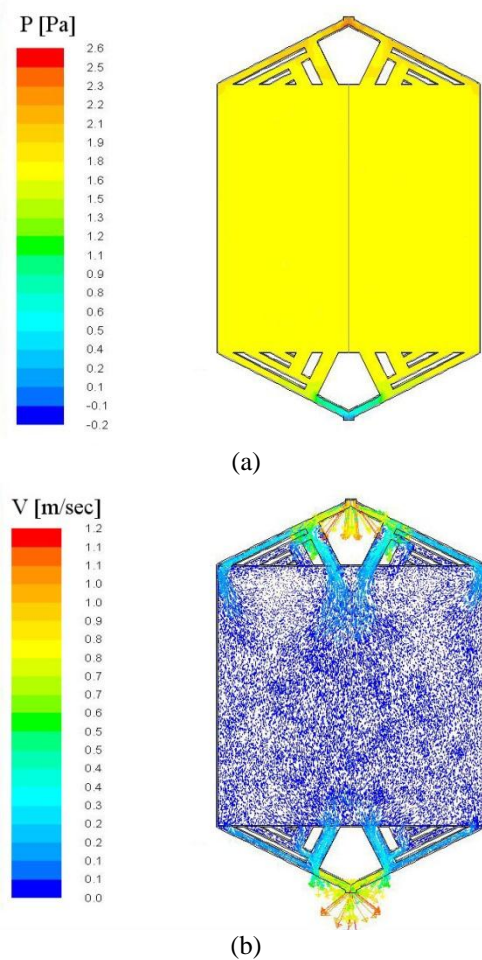
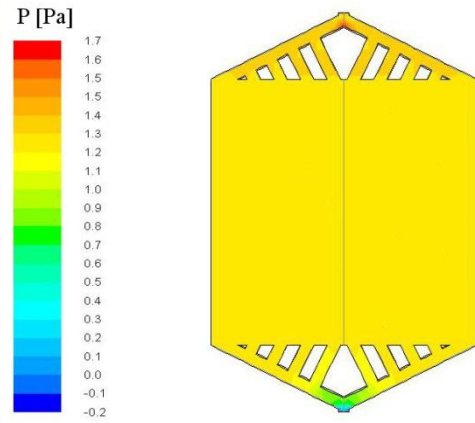
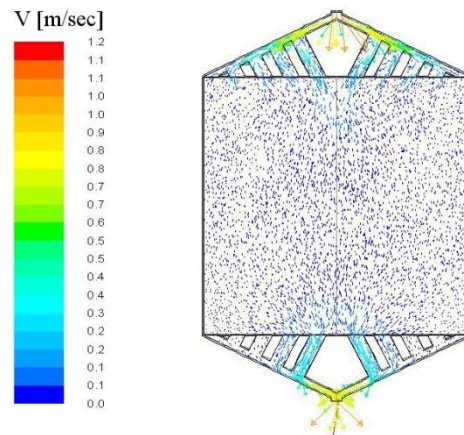


Fig 7: Numerical simulation results of AH3: (a) - Pressure distribution (pa), (b) - Velocity vectors (m/s)



(a)



(b)

Fig 8: Numerical simulation results of AH4: (a) - Pressure distribution (pa), (b) - Velocity vectors (m/s)

4.4.1 Anode housing design 4 (AH 4)

The AH4 configuration is shown in Fig 2. This design is similar to the previous design (AH3), however the flow is diverted evenly into two branches and then sub channels which are perpendicular to the main channels direct the flow over the OPCF. The width of main channels is larger than the sub channels with the objective of capturing and directing the flow evenly across all channels.

Fig 8 (a) shows the pressure distribution, which indicates there, is a high inlet pressure and low out put pressure and even pressure distribution along the entire housing but most importantly across the central region of the flow plate, corresponding to where the OPCF is housed. The velocity flow is shown in Fig 8(b). The modified housing channel design directs the flow evenly across the entire flow plate, with no eddy currents noticed which would significantly reduce stagnant areas in the PEM fuel cell. This Anode Housing Design (AHD 4) has the flow regime and pressure results required by the fuel cell.

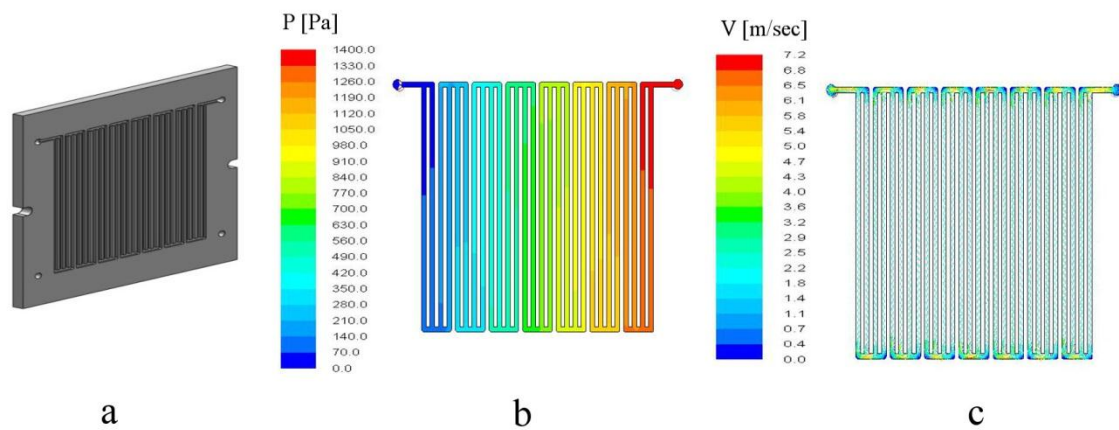


Fig 9: Numerical simulation results of the conventional flow plate: (a) - 3D Model, (b) - Pressure distribution (pa), (c) - Velocity vectors (m/s)

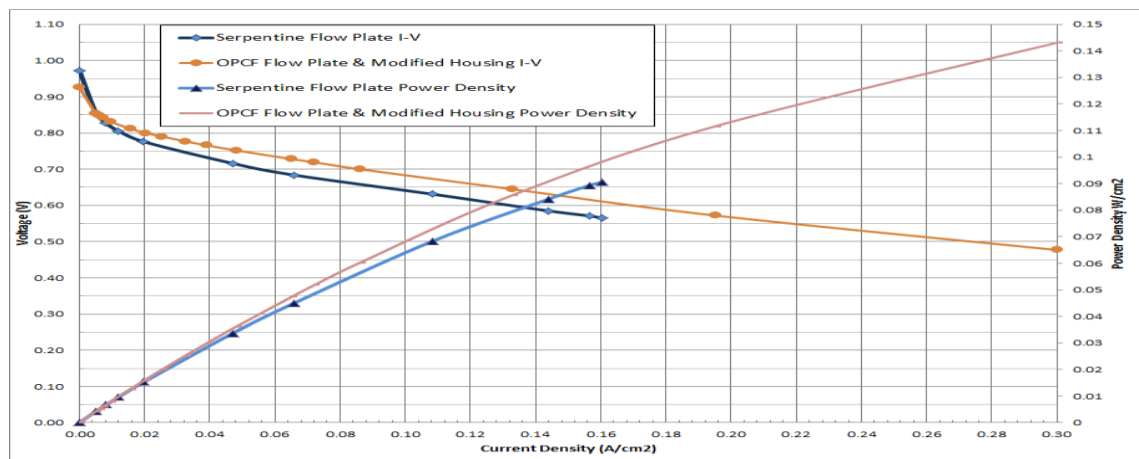


Fig 10: Polarisation curve comparison for serpentine flow plate and OPCF flow plate.

#### 4.5 Comparison of conventional and foam flow plate

#### V.CONCLUSION

To prove the advantage of using OPCF flow plate, CFD analysis was also carried out on the conventional flow plate design, as shown in Fig 9. It can be seen that large pressure drops are viewed with serpentine flow plates. Velocity disturbances at the bends can affect flow. Boundary layers of lower velocity fluid flow are noticed at the bends & channel edges.

In contrast the OPCF Anode housing design 4, as shown in Fig 8, low pressure drops are viewed and velocity disturbances are minimal with an even flow regime visible. The I-V and power density curves of the conventional and OPCF flow plate are shown in Fig 10. It is clear that OPCF flow plates outperformed the conventional serpentine flow plate, recording 0.7 (V) at 0.09 (A/cm<sup>2</sup>). While approximately 0.7 (V) was recorded at 0.05 (A/cm<sup>2</sup>) for the standard double serpentine flow plate.

In this paper, Open Pore Cellular Foam (OPCF) materials were evaluated and tested as a potential material to replace conventional flow plates.

Through a combination of mechanical and Computational Fluid Dynamic (CFD) modelling and analysis effective flow plate designs, flow field configurations and materials are analysed and new cell designs are proposed.

It was found that a suitable OPCF housing design was required to ensure increased support and effective fluid flow through the OPCF. With an optimised design OPCF materials can ensure better gas flow through the fuel cell, lower pressure drop from inlet to outlet and increased PEM fuel cell performance.

The ultimate goal of this body of work is to improve the performance of PEM fuel cells by simplifying their design, allowing fuel cells to offer a promising, possibly green, alternative to traditional power sources, in many applications, without air polluting issues [25, 26].

## VI. REFERENCES

- [1] V. Lawlor, S. Griesser, G. Buchinger, A.G. Olabi, S. Cordiner and D. Meissner, "Review of the micro-tubular solid oxide fuel cell: Part I. Stack design issues and research activities", *J. Power Sources*, 193 (2), pp 387-399, 2009.
- [2] S. K. Dong, B. T. Yun and D. K. Lee, "Design and numerical study for 1 kW tubular SOFC APU system", Anonymous Fuel Cell Seminar, San Antonio; TX; United states: Electrochemical Society, Inc, October, pp 701-706, 2007.
- [3] X. Li and I. Sabir, "Review of bipolar plates in PEM fuel cells: Flow-field designs", *Int J Hydrogen Energy*, 30 (4), pp 359-371, 2005.
- [4] X.D. Wang, Y.Y. Duan, W.M. Yan and X.F. Peng, "Local transport phenomena and cell performance of PEM fuel cells with various serpentine flow field designs", *Journal of Power Sources*, 175(1), pp 397-407, 2008.
- [5] A. D. Le and B. Zhou, "A generalized numerical model for liquid water in a proton exchange membrane fuel cell with interdigitated design", *J. Power Sources*, 193 (2), pp 665-683, 2009.
- [6] A. Kazim, H. T. Liu and P. Forges, "Modelling of performance of PEM fuel cells with conventional and interdigitated flow fields", *J.Appl.Electrochem*, 29 (12), pp 1409-1416, 1999.
- [7] J.P Kloess, X. Wang, J. Liu, Z. Shi and L. Guessous, "Investigation of bio-inspired flow channel designs for bipolar plates in proton exchange membrane fuel cells", *J. Power Sources*, 188(1), pp 132-140, 2009.
- [8] A.P. Manso, F. F. Marzo, J. Barranco, X. Garikano and M.G. Mujika, "Influence of geometric parameters of the flow fields on the performance of a PEM fuel cell. A review", *International Journal of Hydrogen Energy*, 37 (20), pp 15256-15287, 2012.
- [9] Tseng, Chung-Jen, et al. "A PEM fuel cell with metal foam as flow distributor", *Energy Conversion and Management* 62, pp 14-21, 2012.
- [10] C.J. Tsang, B.T. Tsai, Z.S. Liu, T.C. Cheng, W.C. Chang and S.K. Lo, "Effects of flow field design on the performance of a PEM fuel cell with metal foam as the flow distributor", *International Journal of Hydrogen Energy*, 37 (17), pp 13060-13066, 2012.
- [11] A. Kumar and R.G. Reddy, "Materials and design development for bipolar/end plates in fuel cells", *J Power Sources*, 129 (1), pp 62-67, 2004.
- [12] A. Kumar and R.G. Reddy, "Modeling of polymer electrolyte membrane fuel cell with metal foam in the flow-field of the bipolar/end plates", *J Power Sources*, 114 (1), pp 54-62, 2003.
- [13] H. Liu and P. Li, "Even distribution/dividing of single-phase fluids by symmetric bifurcation of flow channels" *International Journal of Heat and Fluid Flow*, 40, pp 165-179, 2013.
- [14] H. Liu, P. Li and J.V. Lew, "CFD study on flow distribution uniformity in fuel distributors having multiple structural bifurcations of flow channels", *International Journal of Hydrogen Energy*, 35 (17), pp 9186-9198, 2010.
- [15] G.M. Imbrioscia and H.J. Fasoli, "Simulation and study of proposed modifications over straight-parallel flow field design", *International Journal of Hydrogen Energy*, 39 (16), pp 8861-8867, 2014.
- [16] A. Kumar and G.R. Reddy, "Effect of channel dimensions and shape in the flow-field distributor on the performance of polymer electrolyte membrane fuel cells", *Journal of Power Sources*, 113 (1), pp 11-18, 2003.
- [17] E. Hontanon, M. J. Escudero, C. Bautista, P. L. Garcia-Ybarra and L. Daza, "Optimisation of flow-field in polymer electrolyte membrane fuel cells using computational fluid dynamics techniques", *Journal of Power Sources*, 86(1), pp 363-368, 2000.
- [18] M. Mohammadi, G.N. Jovanovic and K.V. Sharp "Numerical study of flow uniformity and pressure characteristics within a microchannel array with triangular manifolds" *Computers & Chemical Engineering*, 52, pp 134-144, 2013.
- [19] A. Lozano, L. Valiño, F. Barreras and R. Mustata, "Fluid dynamics performance of different bipolar plates: Part II. Flow through the diffusion layer", *Journal of Power Sources*, 179 (2), pp 711-722, 2008.
- [20] F. Barreras, A. Lozano, L. Valiño, C. Marín and A. Pascau, "Flow distribution in a bipolar plate of a proton exchange membrane fuel cell: experiments and numerical simulation studies", *Journal of Power Sources*, 144 (1), pp 54-66, 2005
- [21] A. Kumar and R.G. Reddy "Application of Metal Foam in the Flow-Field Distributor of Polymer Electrolyte Membrane Fuel Cell Stack". 1060, 204th Meeting, The Electrochemical Society, Inc, 2003. <http://www.electrochem.org/dl/ma/204/pdfs/1060.pdf>
- [22] B. Ramos-Alvarado, A. Hernandez-Guerrero, F. Elizalde-Blancas and M.W. Ellis, "Constructural flow distributor as a bipolar plate for proton exchange membrane fuel cells", *International Journal of Hydrogen Energy*, 36 (20), pp 12965-12976, 2011.
- [23] J.G. Carton and A.G. Olab, "Design of experiment study of the parameters that affect performance of three flow plate configurations of a proton exchange membrane fuel cell", *Energy*, 35 (7), pp 2796-2806, 2010.
- [24] J. G. Carton, V. Lawlor, A. G. Olabi, C. Hochenauer and G. Zauner, "Water droplet accumulation and motion in PEM fuel cell mini-channels", *Energy*, 39 (1), pp 63-73, 2012
- [25] J.G. Carton and A.G. Olabi, "Wind/hydrogen hybrid systems: Opportunity for Ireland's wind resource to provide consistent sustainable energy supply", *Energy*, 35 (12), pp 4536-4544, 2010.
- [26] H. Achour, J.G. Carton and A.G. Olabi, "Estimating vehicle emissions from road transport, case study: Dublin City", *Applied Energy*, 88 (5), pp 1957-1966, 2011.



# Strategic orientation for the ocean energy market roll-out: Coherent technology learning by system dynamics modelling of trans-organisational expert knowledge

## 为海洋能源市场的推出作战略定位：通过跨组织专家知识系统动力学建模进行相干技术学习

Ralf Bucher<sup>1\*</sup>, Ian Bryden<sup>2</sup>

<sup>1</sup>University of Edinburgh, Institute for Energy Systems, Mayfield Road, Edinburgh, EH9 3JL, UK

<sup>2</sup>University of the Highlands and Islands, Ness Walk, Inverness, IV3 5SQ, UK

[r.bucher@sms.ed.ac.uk](mailto:r.bucher@sms.ed.ac.uk)

Accepted for publication on 9<sup>th</sup> September 2014

**Abstract** – The development of an alternative power generation method requires, apart from long-term political support, strong commitment on the technology and financing side. Tidal stream and wave energy presently move from full-scale prototype testing to the implementation of first multi-device arrays. With the intention to gain comprehensive insight into present ocean energy activities and plannings, a diversified interview series was conducted by which 44 experts from 13 stakeholder groups provided their knowledge in the form of 2,129 individual replies. To master the amount and complexity of the multi-level information received, all interview data were systematically consolidated and formed as such the input for the configuration of representative cause-effect relationship diagrams and detailed system dynamics computer models. Based on the calculated ranking of the top-level driving factors for the ocean energy commercialisation process and the subsequent allocation of representative interview statements, balanced propositions for the strategic orientation of technology-driving stakeholders can be made.

**Keywords** – Ocean energy commercialisation, semi-structured expert interviews, system dynamics modelling, competitive collaboration, technology convergence.

### I. INTRODUCTION

The UK is currently the global leader in ocean energy, with more wave and tidal devices installed than the rest of the world combined [1]. Marine renewables form an integral part of the UK energy system transformation and are expected to make a meaningful contribution to the nation's energy mix from around 2025 [2]. After significant technological advances in the last years, the industry now moves from full-scale prototype testing to the implementation of first tidal arrays ranging from 10 to 86 MW [3-5].

To efficiently pass the present pre-profit phase and to head towards regular commercial-scale project implementations, coordinated interaction within and between the stakeholders is required. A conclusive strategy to orientate the ocean energy development process must be capable to integrate the dynamic and complex interplay between all stakeholders. To ensure efficient interaction and long-term collaboration, continuous learning and adaptation efforts are required. Systematically conditioned wide-range expert knowledge provides the best basis herefore.

### II. OBJECTIVE OF THE RESEARCH

The academic objective of the research is on the systematic transposition and refinement of expert interview statements by means of system dynamics (SD) modelling in order to de-risk and accelerate the ocean energy commercialisation process.

The research is oriented around the hypothesis:

*The right strategic orientation of the stakeholders engaged in ocean energy is crucial for efficiently reaching the goal of market-competitive electricity generation. The essential top-level drivers can be determined in a holistic and transparent manner by operating system dynamics computer models based on refined trans-organisational expert interview data.*

The hypothesis acknowledges the importance of having access to different expert knowledge bases and emphasises the need of processing multi-level data. The term “strategic” shall underline the long-term focus of 5 to 10 years and the holistic research concept by integrating the technology, policy and financing sectors. By systematically analysing the wide

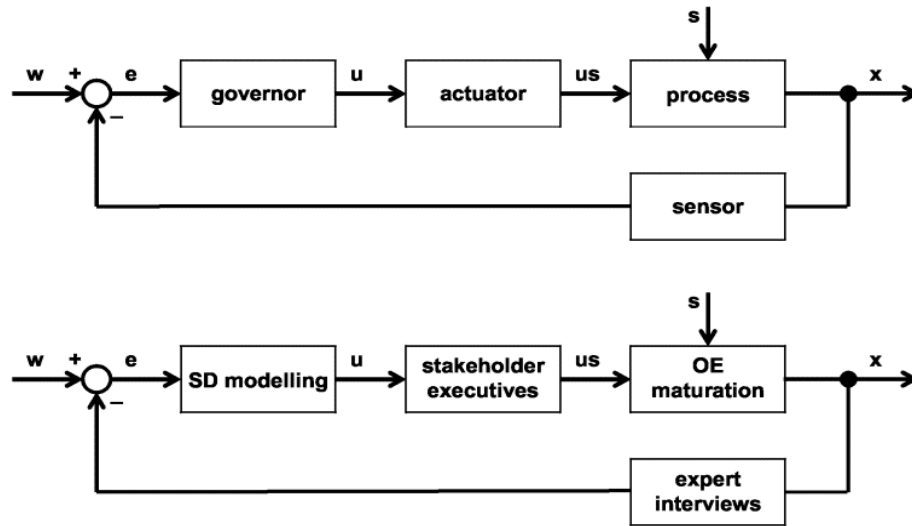


Fig. 1, Closed-loop block diagrams (top part: with ISO control theory terms / lower part: adapted to the present research context).

spectrum of stakeholder-individual strategies and concerns, potential misinterpretations and coordination deficits come to surface at time and viable superordinate strategies can be elaborated.

### III. RESEARCH PRINCIPLE AND METHODOLOGY

The basic principle applied in this research is to create new insight by compiling different sources of knowledge for the elaboration of an optimum strategy towards achieving market competitive generation. New knowledge is generally created through a process of applying multiple perspectives to the same information, as outlined in a study in the field of experimental behavioural science by Okhuysen & Eisenhardt [6]. In order to follow this principle of multiple perspectives, experts from all stakeholder groups were invited to contribute with their individual experience and know-how. Based on this multi-disciplinary attempt, an all-encompassing appraisal becomes possible by avoiding concentrating in a limiting manner on stakeholder-specific views or interests only.

The use of system dynamics modelling techniques assures the envisaged open-integrative instead of detailed-specialist character of the research. The methodology applied considers the long-term and dynamic development of the ocean energy sector by continuous information gathering and data processing oriented at feedback control principles. To master the amount and complexity of the cross-category information and to systematically identify the fundamental interview statements, all data were uniformly consolidated and formed as such the basis for the configuration of detailed cause-effect relationship diagrams<sup>1</sup>. The final system dynamics models emerged from “iterative cycles of data gathering, feedback analysis, implementation and evaluation” as described by Formentini & Romano [7] in a knowledge management context.

The research principle of data collection, information compression, system dynamics modelling and the creation of strategic propositions can be outlined by referencing to the closed-loop control model. In Fig. 1, one standard and one adapted block diagram are shown which comprise all elements defining a dynamic and complex process to be controlled – either of technical or organisational nature. The respective analogies between the terms and concepts in control theory and the present research context are shown in Table 1.

TABLE 1, ANALOGIES BETWEEN TERMS AND CONCEPTS IN CONTROL THEORY AND THE PRESENT RESEARCH CONTEXT

Control theory	Ocean energy commercialisation
Reference $w$	Full commercial power generation
Deviation $e$	Remaining development progress
Governor	System dynamics (SD) modelling
Actuating signal $u$	Calculated top-level driving factors
Actuator	Stakeholder executives
Actuating value $us$	Management decisions and actions
Process	Ocean energy (OE) maturation
Disturbance $s$	Setbacks, difficulties, risk impacts
Actual value $x$	Actual status of ocean energies
Sensor	Periodic cross-category interviews

The following chronological steps were necessary: (i) conduction of 44 expert interviews; (ii) analysis and sorting of replies; (iii) compression of information by introduction of ordering terms; (iv) configuration of system dynamics computer models; (v) calculated ranking of impact factors and definition of top-level driving factors; (vi) allocation of representative interview statements; and (vii) elaboration of recommendations for the strategic orientation of the technology, policy and financing sectors.

<sup>1</sup> System dynamics software used: Process Modeller, Consideo, Germany.

#### IV. SEMI-STRUCTURED EXPERT INTERVIEWS

For the survey, a four-page questionnaire with a total of 90 questions was elaborated out of which 48 were yes/no questions and 42 of qualitative character asking for stakeholder-specific experience or assessment. By contacting 136 selected representatives from 15 stakeholder groups, we received 71 feedbacks out of which originated 11 personal and 15 telephone interviews as well as 20 filled-out questionnaires. 2 received questionnaires had to be discarded because they were greatly incomplete. As a result, the knowledge of 44 managers, experts and specialists from 13 stakeholder groups was ultimately retained for the analysis, corresponding to an effective return rate of 32.4 % which is more than usual for studies of this nature [8]. A total number of 2,129 individual replies had to be grouped in order to formulate higher-level correlations as basis for the computer-based SD-modelling.

Table 4 lists stakeholders that finally participated in the interviews or sent back filled-out questionnaires.

#### V. SURVEY RESULTS AND STATISTICAL FINDINGS

##### A) Virtual reference project

With the aim to harmonise and to uniformly direct the research, the interviewees were asked to give a prognosis on the development prospects of ocean energy. Utility-scale generation is expected in 2021 for tidal stream and 2024 for wave power. The average array rating is given for tidal stream at 36 MW and for wave power at 38 MW with investment cost of 102 m€ (2,900 €/kW) respectively 118 m€ (3,100 €/kW).

##### B) Interview-based ranking of selected risks

The interview participants provided estimations for risk levels focussing on the realisation of the virtual reference project (~40 MW, ~2025, ~100 m€) as follows:

- (i) Top risks: achieving funding, keeping budget, reliability.
- (ii) High risks: supply chain, time schedule, regional grid.
- (iii) Medium risks: sea use license, marine flora/fauna, conflict of interest, capability of shipyards/ports, feed-in tariff, insurance cost, extreme weather, health and safety.

Apart from financial aspects, the key risk in ocean energy is related to uncertainty in device performance or reliability.

#### VI. SYSTEM DYNAMICS MODELLING

##### A) Referenced basic model: "Full commercial power generation by marine energy"

In total 3 system dynamics models were elaborated. For the basic model explained in [9], all positive (reinforcing) and negative (countervailing) influences on the final objective of full commercial power generation by ocean energy were grouped and inter-correlated.

Out of 234 individual replies, 16 top-level driving factors essential for achieving commercial power generation were systematically identified and concentrated into 3 milestone terms:

- (i) Government support: The long-term commitment from government represents the fundament for the further progress of the sector. Early stage developments depend on coordinated funding mechanisms and fiscal measures as well as an efficient consenting process.
- (ii) Array-scale success: The 2<sup>nd</sup> ranked top-level driving factor (showcase commercial-scale projects / successful demonstrators) forms the essential element of this interim milestone that triggers the further development.
- (iii) Cost reduction: After having successfully demonstrated the array-scale success, LCOE<sup>2</sup> will decline due to serial manufacturing and technology convergence processes.

As the singular characteristics of governmental support are outside the range of this contribution, the context around achieving the interim milestone "array-scale success" was examined in detail by identifying the respective reinforcing and countervailing impact factors.

##### B) Reinforcing model: "Showcase commercial-scale projects / successful demonstrators"

In this higher focussed model, the 2<sup>nd</sup> ranked top-level driving factor identified by the basic model of showcasing commercial-scale projects or successful demonstrators serves as new target factor. In the right hand middle area in Fig. 2 we find it being fed via 3 main nodes: (i) knowledge transfer and learning from neighbouring sectors; (ii) top-priority tasks in the work the government agencies; and (iii) having costs under control. These nodes correspond to the cornerstone elements for harnessing the potential of ocean energy presented by McSweeney as: technology, policy, financing [10].

The SD-model was configured one-on-one to the interview replies so that it directly reflects the first-hand experience and projections of all interviewed stakeholders. Based on the questionnaire, 11 representative group terms (i.e. "lessons learnt in the oil/gas industry") were pre-formulated. Out of 671 individual replies, 26 generic terms (i.e. "device operation experience") were defined. The number of replies received under a specific aspect defines the relative impact onto a node and finally on the target factor. The inter-correlation between the generic and group terms is determined by the distribution of the expert interview replies. Calculated weighting factors define the intensity of a correlation link and are displayed as normalised values. The simulation runs showed that the most important generic term (or impact factor) is "technology learning" being interconnected by strong causal links.

The elaborated cause-effect relationship diagram enables a factual representation and analysis of multi-level data.

<sup>2</sup> Levelised cost of electricity are defined as the ratio of the net present value of total capital and operating costs of a generic plant to the net present value of the net electricity generated by that plant over its operating life.

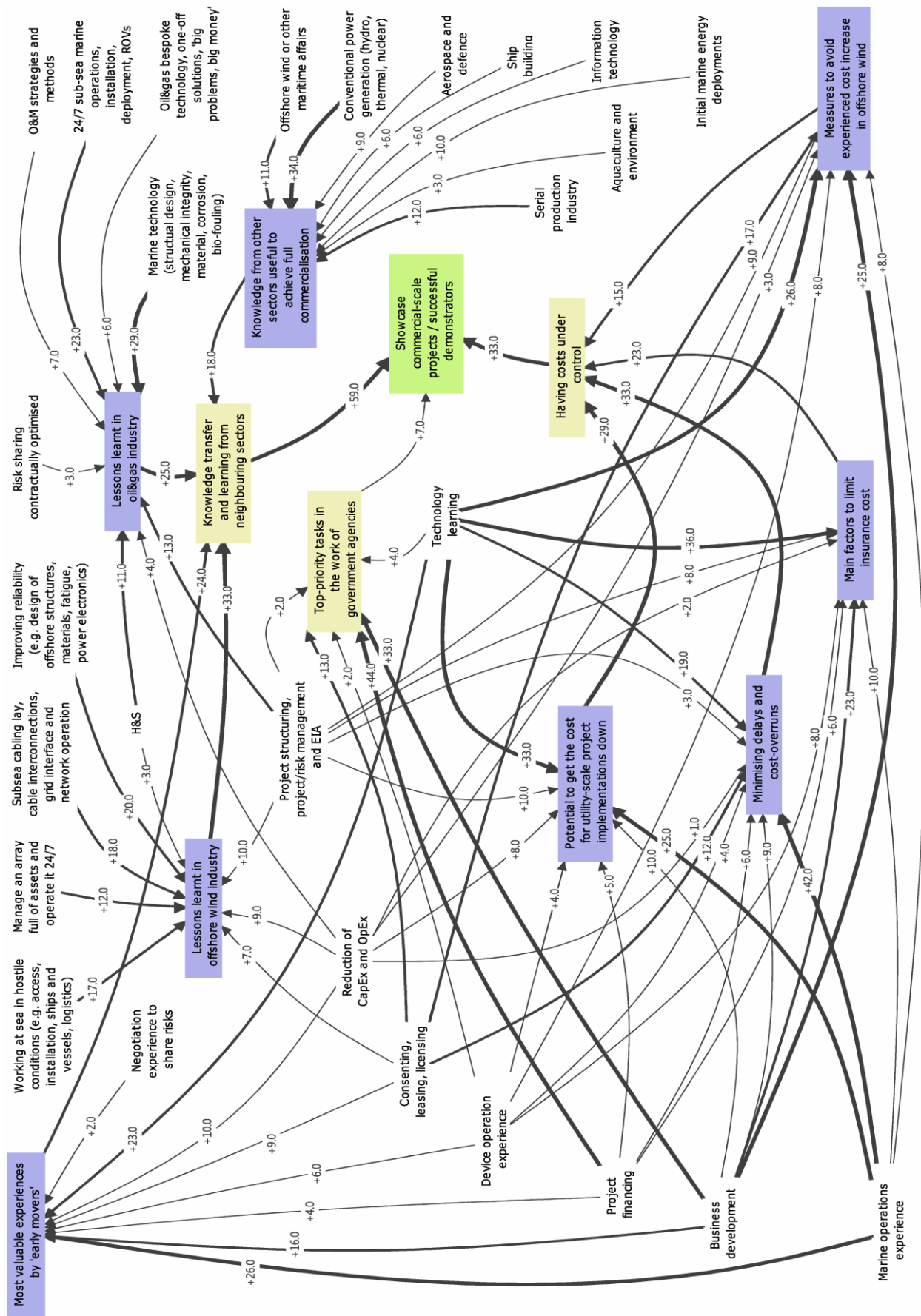


Fig. 2, Reinforcing system dynamics model: "Showcase commercial-scale projects / successful demonstrators".

C) *Countervailing model: “Negative impact on the development of ocean energy”*

To make full use of the insight gained in the interviews, in a further system dynamics model exclusively negative, delaying or countervailing impacts (generated from 1,712 individual replies) on the development of ocean energy were considered.

D) *Simulation results and grouping of impact factors*

In Fig. 3 the simulation results of the two in-depth system dynamics models described under B) and C) are shown in combined manner in the so-called “insight matrix”. On the left hand side, the impact factors with negative effect on reaching the target of full commercial power generation by ocean energy are located and on the right hand side the ones with positive effect. The y-axis indicates the impact intensity behaviour on the target over time. The greater the distance from the axes of coordinates, the more significant a factor is. As the axis scales in both examined system dynamics models are identical, the impact values can be directly compared.

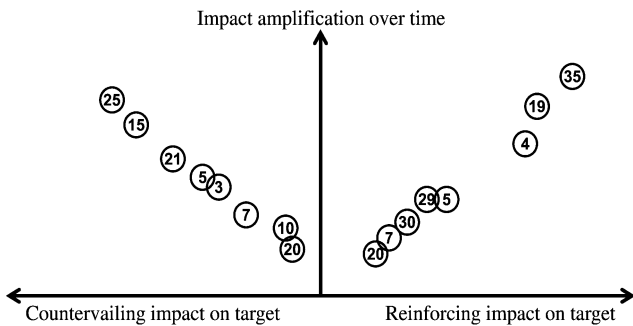


Fig. 3, Combined insight matrix showing countervailing and reinforcing impact factors on commercialising ocean energy.

Following the results of the system dynamics calculation runs on “showcase commercial-scale projects / successful demonstrators” and “negative impact on the development of ocean energy”, in Table 2 the identified countervailing (–) and reinforcing (+) impact factors are grouped and ranked according to their summarised impact levels. The item numbering (#) refers to Fig. 3.

TABLE 2, GROUPED IMPACT FACTORS (WITH IMPACT LEVELS)

–	<b>Technology</b> (summarised impact: 551)	+
#25	Technology learning (83+100)	#35
#15	Marine operations experience (74+86)	#19
#21	Project/risk management, EIA (61+44)	#29
#7	Device operation experience (36+27)	#7
#20	Marine technology (21)	
	Project management (19)	#20
–	<b>Policy</b> (summarised impact: 100)	+
#5	Consenting, leasing, licensing (51+49)	#5
–	<b>Financing</b> (summarised impact: 59)	+
	Reduction of CapEx and OpEx (35)	#30
#10	Funding requirement (24)	

The by far strongest impact on the objective to showcase commercial-scale projects or successful demonstrators identified by the reinforcing system dynamics model is correlated to “technology learning” (for calibration purposes defined with an impact level of 100) followed by “marine operations experience” (impact: 86). The most significant “negative impacts on the development of marine energy” are similarly related to “technology learning” (impact: 83), “marine operations experience” (impact: 74) and in third place “project/risk management and EIA (environmental impact assessment)” by an impact level of 61. The high relevance of business development (#3 & #4) as the intermediary element between technology, policy and financing is underlined by a significant impact level of 123 (46+77).

E) *Compilation of corresponding interview statements*

In Table 3 the most relevant recommendations and strategy options for the sector-specific orientation are given. They are based on the calculated prioritisation by the system dynamics simulation software and correlated expert statements.

VII. STRATEGIC ORIENTATION (TECHNOLOGY)

A) *Systems engineering approach*

When asking for significant potential to get the cost for utility-scale project implementations down, the CEO of an Irish wave energy converter manufacturer emphasised the clear recognition to orientate the development and research strategies at the US space-/aircraft industry and here especially on the systems engineering principles. The vice president of a multi-national engineering conglomerate underlined in similar manner the importance to prove that systems work reliably and to focus on end user requirements. This statement correlates with the central objective in systems engineering as to consider the finally envisaged functionality already in early project stages. An important element in the design and implementation process of complex technological systems is to perform regular system functionality checks. Finally, the ocean energy converters have to operate on the long term in open sea grid-connected multi-device arrays.

B) *Multi-applicable technologies and joint concepts*

According to the opinion of a utility’s ocean energy project manager, one of the top-priority tasks in the work of academia & research should be to concentrate on multi-applicable technologies and standardised devices and components (e.g. moving parts, cable connector systems, control interfaces). The benefit by working along a robust engineering plan targeting on serial production and large-scale manufacturing was underlined. To finally ensure identical component design and delivery, effective supply chain management and leveraging logistics is required. Referencing to offshore wind, in [11] it is pointed out that joint installation and maintenance concepts for adjacent wind farm locations significantly increased installation and operating efficiency.

C) *Standardisation (look at volume manufacturing)*

The reply of a project developer’s head of offshore when asking for the most valuable experience gained by the early

TABLE 3, STRATEGIC ORIENTATION FOR THE TECHNOLOGY, POLICY AND FINANCING SECTORS

<p><b>Technology</b> with reference to interview replies under “technology learning, marine operations experience, project/risk management and EIA, device operation experience, marine technology, project management”</p> <ul style="list-style-type: none"> <li>▪ Adopt systems engineering principles inspired by the space-/aircraft industry</li> <li>▪ Consider that extreme engineering is required with a focus on survivability and reliability</li> <li>▪ Reduce the number of technological concepts (technology convergence)</li> <li>▪ Develop multi-applicable technologies (standardisation of components) and joint concepts</li> <li>▪ Design for installation and maintenance purposes</li> <li>▪ Minimise the lack of collaboration and improve knowledge sharing</li> <li>▪ Gain offshore deployment experience with full-scale devices</li> <li>▪ Move from device testing towards array-scale activities under open sea conditions</li> <li>▪ Integrate risk management into project management</li> <li>▪ Consider the need to restructure and commit to the supply chain</li> </ul>
<p><b>Policy</b> with reference to interview replies under “consenting, leasing, licensing”</p> <ul style="list-style-type: none"> <li>▪ Facilitate consenting, leasing, licensing (i.e. with a single point of handling the process)</li> <li>▪ Promote cross-interaction between renewables</li> <li>▪ Stimulate appropriate risk sharing between the stakeholders</li> <li>▪ Encourage initiatives to bring in expertise from offshore oil &amp; gas marine operations</li> <li>▪ Focus on availability of qualified personnel and heavy marine services</li> <li>▪ Underline the importance of knowledge sharing (central bottleneck)</li> <li>▪ Improve collaboration and alignment between industry, utilities, academia, device manufacturers and project developers</li> <li>▪ Support grid-connected test facilities and pilot zones</li> <li>▪ Support strategies for grid operation with significant wave and tidal power in-feed</li> <li>▪ Simplify access to the international (out of Europe) market</li> </ul>
<p><b>Financing</b> with reference to interview replies under “reduction of CapEx and OpEx, funding requirement”</p> <ul style="list-style-type: none"> <li>▪ Recognise that pilot projects with availability records provide confidence in the performance of the core technologies</li> <li>▪ Support technologies with declared synergies towards off-shore wind</li> <li>▪ Consider the likelihood of early-stage failures and the failing in unexpected parts of project</li> <li>▪ Keep in mind that realism is required when it comes to the (global) scale of the industry</li> <li>▪ Focus on cost of energy and not on CapEx</li> <li>▪ Consider that the cost of energy production is dependent on the capacity deployed</li> <li>▪ Evaluate the insurability of projects</li> <li>▪ Recognise differences to offshore oil &amp; gas with regard to design, manufacturing and logistics</li> <li>▪ Realise the advantage of working with the already existing companies in the market</li> <li>▪ Encourage contract structuring and contract standardisation as in onshore wind</li> </ul>

movers, was the “experienced negative impact by missing standardisation”. Considering the urgent need for consensus over standardisation, one interviewee referred to the detected over-engineering in oil & gas standards (with regard to marine energy purposes). A marine renewables engineer employed with an energy consulting firm identified “consensus over standardisation” as a target that appeared more difficult to reach in the last years than originally planned. One interviewee summed up the situation as “no standards, no results”. The overall importance of standardisation in ocean energy was emphasised by several interviewees when highly appreciating the published results by the standardisation group within one of the top three certification companies. The date of publishing new technical standards and the level of detail need to be carefully discussed with manufacturing companies to avoid early-stage limitations on non-published but promising R&D projects and unnecessary cost increase. A senior contracts

expert of an international UK law firm mentioned the need for contract standardisation and collaborative contracts (contracts that allow purchasing goods, services and works collectively to achieve favourable contract terms). Contract splitting (e.g. in turbines, fundament, transformer station, inner-park cabling) as in offshore wind was recommended.

#### D) Technology convergence

According to a senior principal surveyor of a global offshore classification society, a top-priority task in their work is towards technology consolidation. A utility’s representative underlined the potential to get the cost for commercial-scale project implementations down by the positive impact of technology convergence. Augustine et al. [12] concentrate in their research on technology convergence and concept evaluation processes in industrial product development. They emphasise that rather than selecting the better among available

alternatives, the progression towards better solutions by combining the strengths of all available concepts is a more robust approach for concept improvement. It is expected that the presently high number of technological concepts in ocean energy will be reduced in the course of competitive project implementations. Considering the dynamic development in wind power, it is noteworthy that since the beginning in the 1980ies until today the rotor diameter has increased from 15 to 124 m and the nameplate rating from 50 to 5,000 kW [13]. The next development step in offshore wind is expected to be the introduction of 7 or even 10 MW turbines [14].

#### *E) Knowledge sharing and knowledge transfer*

The limited knowledge sharing in industry is seen by the strategy manager of a public-private partnership and the head of energy of UK's innovation agency as a main reason why the ocean energy sector has not developed more rapidly. A senior policy officer of the Scottish government emphasised the need to transfer lessons learnt in the offshore wind industry to ocean energy in order to avoid duplication of time and effort. According to the vice-chair of the largest private R&D group in Spain, the transfer of knowledge from other sectors (under consideration of the specific aspects of ocean energy) is identified as a top-priority task in the commercialisation process. The project manager for the implementation of the world's first commercial breakwater wave power plant outlined that the need to improve the sharing of bad (!) experience and testing data is key. According to his commissioning experience, sometimes unspectacular and cheap items created unexpected difficulties. To support progress, his position is to inform (as far as possible) about such complications at conferences, to explain why things went wrong and to display the finally implemented solution.

#### *F) Maximising collaboration and minimising competition*

In line with the findings on limited sharing of knowledge, a lack of collaboration of the industry was reported. Apart from improving cooperation, a strengthening of interaction between the device manufacturers and the engineering consultancies companies was called for. The head of policy of a major UK developer emphasised the expectable benefits by enhanced collaboration between individual project developers. With regard to academia, he mentioned the need to intensify international collaboration. The artificial competition with on-/offshore wind was criticised by an Irish ocean energy development manager as negatively influencing an uninterrupted progress. A chance to improve cross-interaction between the renewable energies is seen in identifying prospective synergy effects by inter-coupling different kinds of carbon-free generation methods. The interviewed head of development of a wave energy device manufacturer – which recently entered into a research and development collaboration with a major offshore wind developer – underlined the attractiveness of exploring the prospects by combining wave and wind power. Seeking synergies with other manufacturers considering the use of similar technology is seen as a natural process. The experienced increasing involvement and interaction with major industrials in the ocean energy sector is seen as positive and will help to restructure the supply chain.

#### *G) Offshore deployment experience*

With the aim to demonstrate the viability of electricity generation by ocean energy, it is required to provide transparency to investors and to focus on “bringing some 10 MWs in the water” as the programme director of a leading UK centre of sustainable energy expertise and pioneering project delivery outlined. Especially the importance to design for installation and maintenance purposes was emphasised by the representative of a wave energy converter manufacturer. As lessons learnt in the offshore oil & gas industry to be transferred to ocean energy, a senior manager at a Canadian utility mentioned their focus on reliability and survivability.

#### *H) Competitive collaboration and inter-firm alliances*

Ocean energy needs to assert its position in the competitive renewable energy market. Regular commercial projects will finally be realised under established international procurement principles for which a number of similarly competent industrial bidders is required. In case natural competitors accept the high significance of jointly achieving the identified intermediate milestone “array-scale success”, the motivation for inter-firm alliances will rise. Exemplary strategic alliances on how to develop new products and to penetrate new markets can serve as references. The benefits by inter-firm co-operations need to be individually examined in the course of risk/reward assessments. In a recently published paper from the European Ocean Energy Association [15], clear reference was given towards Airbus which was classified as a prime example of a successful venture that would not have taken off without transnational collaboration between industry and governments. Amanatidou & Guy [16] emphasise the increasing importance of knowledge-based industries and focus on aligning existing perceptions by maximising collaboration and minimising competition. As described by [17] cooperative relationships between firms in high technology can bring to market new innovations that neither firm alone could have accomplished. Especially for firms which are not part of the group of ocean energy front-runners, new inter-firm collaborations offer potential to prepare for global competition. The term “competitive collaboration” was introduced by [18] for strategic alliances that strengthen companies against outsiders (i.e. other renewables) even as they weaken each partner vis-à-vis the other.

#### *I) Strategic risk management*

Conventional risk management procedures are mainly tailored for stakeholder-specific duties or project-related functions. When opening risk management towards accompanying an energy system transformation project – for which the development and grid-integration of ocean energy is a good example – the usually considered time frame and the grade of complexity increase. Frigo & Anderson [19] explain that strategic risk management encompasses the interdisciplinary intersection of strategic planning, risk management and strategy execution. The development manager of a wave energy converter firm explained that their company approach towards risk management is to collaborate with a multi-national oil & gas exploration corporation. He generally stressed the requirement to share risk by

collaboration and to integrate risk management into project management. Modern strategy-based and life-cycle oriented management incorporates real-time management of risks. Risk sharing shall be contractually optimised to identify the most appropriate risk owners.

*J) Adjusting the “installed capacity / capacity factor”-ratio*

The principal scientist of UK wave power developer underlined that the cost of energy production is dependent on the capacity deployed. In Bucher [20] this relationship was examined for an envisaged 600 MW tidal array in Korea. Based on a full lunar cycle 3D tidal regime model, detailed statements on optimising the “installed capacity / capacity factor”-ratio and consequently limiting the financial risk could be made. The possibility to select a preferred ratio of capital investment to profit widens the circle of potential investors and helps to effectively de-risk early-stage project initiatives.

*K) Detail complexity and dynamic complexity*

When asking for measures to increase equipment reliability, a renewable energy consultant recommended to “design out complexity/failure points”. For managing complexity, the differentiation between detail (or combinatorial) and dynamic complexity as in the complex systems theory [21] is helpful:

- (i) Detail complexity is characterised by many elements and a large number of combinatorial possibilities. Groesser [22] explained that in detail-complex situations methods to reduce complexity might be useful. In the present context potential to reduce detail complexity is seen in applying systems engineering, standardising components and using multi-applicable technologies. When taking a look at the wider picture, a reduction of detail complexity can be achieved in commercial project implementations in the course of a “competitive technology qualification routine” (as described further below). The long-term best-performing device or system would be identified in a transparent process.
- (ii) Dynamically complex systems contain non-linear feedback, time delays and accumulations. Cause and effect are subtle and obvious interventions can produce non-obvious consequences. It might arise even in simple systems and can usually not be reduced but managed. Dynamic complexity is characteristic for large-scale engineering and construction projects with multiple feedback-processes, non-linear relationships and the need to integrate hard and soft data [23,24]. The process of commercialising ocean energy comprises high dynamic complexity because of the continuously varying interaction between heterogeneous stakeholders over a decade’s long period of time. In order to improve project success rates, Groesser [22] recommends qualitative feedback modelling as a method to analyse and manage dynamic complexity. In the ocean energy context, potential to handle the high dynamic complexity is seen in the “interview/modelling/action”-approach in Fig. 1.

Research revealed that in conventional project management mainly aspects of detail complexity are considered [25]. Senge [26] underlines that the real leverage in most management

situations lies in understanding dynamic complexity. According to his research, most established planning tools and analysis methods are designed to handle detail complexity but are not equipped to deal with dynamic complexity.

*L) Competitive technology qualification routine*

The interview participants identified reliability concerns as the top-ranked non-commercial risk and on the opposite side poor liability was mentioned as key operational risk. The widespread perception of high cost and unproven reliability was mentioned by the strategy manager of a public-private partnership as negatively influencing the sector. A US academic named the need for longer baselines for systems reliability and an R&D vice-chair emphasised that (currently) reliability is more important than efficiency. The managing director of a UK financial firm and the vice president of a Canadian project developer emphasised that concerns for delays and cost-overruns mainly relate to reliability, durability and performance of ocean energy converters. According to a Scottish government employee, the failure of devices was the fundamental and greatest single reason for projects being delayed or cost increase. Reasons why the ocean energy sector has not developed more rapidly were repeatedly identified in the uncertainty of device performance and reliability. The requirement to demonstrate equipment reliability at utility-scale devices was formulated by the machinery manager of a global maritime classification society. The division head of an Irish state agency replied to the question on where research is most required to accelerate the development of marine energy that reliability and integrity of devices are essential.

When asking for measures by which the experienced cost increase in offshore wind can be avoided in ocean energy, a marine energies project manager of a large utility recommended to compromise cost and reliability. As main factors for reaching commercial generation, two senior members of classification societies stressed uncertainty about reliability and the need to focus on it. To achieve a satisfactory technology reliability record, experts recommended to put more focus on reliability in system design and to introduce reliability modelling.

In all above listed interview statements the key importance of technology reliability was uniformly emphasised. As years will pass until full technology maturity will be reached, Bucher [27] proposed for early commercial project implementations a competitive technology qualification routine to achieve the required safety for investment. The principal idea is to extend the execution of utility-scale projects by a qualification procedure in the course of which different manufacturers' power conversion devices are deployed and operated in real-sea conditions in the final project area for a defined period of time. The individual device performance is independently assessed and the manufacturer of the best-ranked system is awarded the principal supply contract. Non-successful competitors are compensated.

The competitive technology qualification routine represents a transparent and evidence-based selection procedure to identify most suitable technology for a site. In a carefully selected project environment, the approach might apply.

### VIII. CONCLUSIONS AND RECOMMENDATIONS

The principal objective of this research is to create strategic knowledge to orientate the ocean energy (technology) learning processes towards reaching commercial power generation. Considering the dimension and potential of ocean energy, elaborate measures to coordinate the development of the sector are necessary. The inherent high dynamic complexity of such an undertaking makes it necessary to apply tools and methods that are capable to reflect the entire process and to identify top-level driving factors in a holistic but systematic manner.

In order to rapidly overcome the present pre-profit phase, the clearing of the interim milestone “array-scale success” represents a key target, which will pave the way towards the envisaged market roll-out. To safely identify the decisive technical-organisational principles to be applied, the unbiased inclusion of trans-organisational expert knowledge is required. The use of cross-category interview data to configure system dynamics computer models is seen as the adequate basis to comprehensively assess the prevailing situation and to provide effective recommendations for the stakeholders’ medium- and long-term strategy planning and adjustment.

Referencing to the initial hypothesis, the paper makes the following contribution:

*The top-ranked risks for utility-scale ocean energy projects (achieving funding, uncertainty in device performance) are directly intercorrelated as investor confidence mainly depends on track records of continuous device operation. Clearing the identified interim milestone “array-scale success” will create confidence and de-risk investments. Intensified technology learning is seen as determinant for the development of the sector. It comprises strategic principles such as applying systems engineering, strengthening standardisation and minimising competition by competitive collaboration. System dynamics computer modelling provides the tools to master the complexity of multi-level interview data and to impartially identify top-level drivers. Representative expert interview statements can be directly allocated based on the calculated ranking of priority and subsequently be analysed in detail.*

With the presented principles, specific experience can be integrated for the benefit of a coordinated way towards commercially viable electricity generation by ocean energy.

The paper shall conclude with a convincing statement given by one interviewee:

*“Generally, if device developers can successfully operate their demonstration devices at a high level of availability for an extended period of time (at least 3 years) then most of the other desirable outcomes, such as investment, takeovers by large companies, grid upgrades and so on, would follow automatically”.*

#### ACKNOWLEDGEMENT

The study is part of a PhD research into strategic risk management for marine energy projects at the Institute for Energy Systems, University of Edinburgh, UK. The author is

grateful to the interviews participants and Prof Bryden for his continuous support and inspiring discussions. Thanks to the anonymous reviewers for providing helpful suggestions.

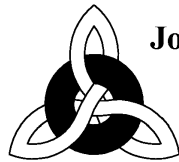
TABLE 4, LIST OF PARTICIPATING STAKEHOLDERS

<b>Government (associations) &amp; trade organisation:</b> The Scottish Government (UK), Marine Scotland (UK), Energy Technologies Institute (UK), Carbon Trust (UK), Department of Energy and Climate Change (UK), The Crown Estate (UK), Scottish Natural Heritage (UK), Centre for Environment, Fisheries & Aquaculture Science (UK), RenewableUK (UK), Technology Strategy Board (Ireland).
<b>Certifying authorities:</b> Det Norske Veritas (UK), Lloyd’s Register (UK).
<b>Investors &amp; lenders:</b> Green Giraffe (UK).
<b>Law firm:</b> Eversheds International (UK).
<b>Academia &amp; research:</b> University of Washington (USA), University of Edinburgh (UK), National Taiwan Ocean University (Taiwan), Irish Marine Institute (Ireland).
<b>Engineering consultancies:</b> Natural Power (UK), Xodus Group (UK), Tecnia Research & Innovation (Spain), South West Renewable Energy Agency (UK), Royal Haskoning (UK).
<b>Project developers:</b> Emera (Canada), EDF (France), Electricity Supply Board (Ireland), Iberdrola (Spain).
<b>Owners &amp; operators:</b> ScottishPower Renewables (UK), Ente Vasco de la Energía (Spain).
<b>Transmission system operator:</b> Scottish and Southern Energy Renewables (UK).
<b>Device manufacturers:</b> Marine Current Turbines (UK), Pelamis Wave Power (UK), Wavebob (Ireland), Siemens (Germany), Wave Star (Denmark), Ocean Renewable Power Company (USA).
<b>Offshore contractors:</b> 6 contacted (no feedback).
<b>Test site operators:</b> European Marine Energy Centre (UK), Fundy Ocean Research Centre for Energy (Canada), National Renewable Energy Centre (UK), Minas Basin Pulp & Power (Canada), France Energies Marines (France).
<b>NGO:</b> Greenpeace (UK).
<b>Offshore wind industry:</b> Dong Energy Power (UK).
<b>Oil &amp; gas industry:</b> 4 contacted (no feedback).

#### REFERENCES

- [1] RenewableUK (2013) Wave & tidal energy, [www.renewableuk.com](http://www.renewableuk.com) [13/02/2013]
- [2] Low Carbon Innovation Co-ordination Group (2012) Marine energy summary report: Technology innovation needs assessment, UK
- [3] Scottish Government (2013) Major boost for wave and tidal industry, <http://news.scotland.gov.uk> [09/11/2013]
- [4] ScottishPower Renewables (2013) Sound of Islay, [www.scottishpowerrenewables.com](http://www.scottishpowerrenewables.com) [10/05/2013]

- [5] MCT (2013) Skerries Tidal Array secures consent, [www.marineturbines.com](http://www.marineturbines.com) [10/05/2013]
- [6] Okhuysen, G.A. & Eisenhardt, K.M. (2002) Integrating knowledge in groups: How formal interventions enable flexibility, *Organisation Science* 13 (4), pp370–386
- [7] Formentini, M. & Romano, P. (2011) Using value analysis to support knowledge transfer in the multi-project setting, *International Journal of Production Economics* 131, pp545–560
- [8] Masini, A. & Menichetti, E. (2012) The impact of behavioural factors in the renewable energy investment decision making process, *Energy Policy* 40, pp28–38
- [9] Bucher, R. (2013) Strategic risk management in ocean energy: A system dynamics approach to the evaluation of 40+ expert interviews, *Proceedings of the 10th European Wave and Tidal Energy Conference*, Aalborg, Denmark
- [10] McSweeney, J. (2012) Ocean energy: Harnessing the potential, *Proceedings of the 4th International Conference on Ocean Energy*, Dublin, Ireland
- [11] Cost Reduction Potentials of Offshore Wind Power in Germany, *The German Offshore Wind Energy Foundation*, [www.offshore-stiftung.de](http://www.offshore-stiftung.de) [18/02/2014]
- [12] Augustine, M. et al. (2010) Concept convergence: A framework for improving product concepts, *Computers & Industrial Engineering* 59, pp367–377
- [13] Oceans of Opportunity, *Harnessing Europe’s largest domestic energy resource*, A report by the European Wind Energy Association, [www.ewea.org](http://www.ewea.org) [26/07/2010]
- [14] Jensen, D. & Könemann, D. (2010) *Alpha Ventus operation offshore*, ISBN: 978-3870734794
- [15] Industry vision paper 2013, *European Ocean Energy Association*, [www.oceanenergy-europe.eu](http://www.oceanenergy-europe.eu) [20/02/2014]
- [16] Amanatidou, E. & Guy, K. (2008) Interpreting foresight process impacts: Steps towards the development of a framework conceptualising the dynamics of foresight systems, *Technological Forecasting & Social Change* 75, pp539–557
- [17] Hull, F. & Slowinski, E. (1990) Partnering with technology entrepreneurs, *Research Technology Management* (November–December), pp16–20
- [18] Hamel, G. et al. (1989) Collaborate with your competitors and win, *Harvard Business Review* 133
- [19] Frigo, M.L. & Anderson, R.J. (2009) Strategic risk assessment: A first step for improving risk management and governance, *Strategic Finance*, pp25–33
- [20] Bucher, R., Couch, S.J. (2013) Adjusting the financial risk of tidal current projects by optimising the “installed capacity / capacity factor”-ratio already during the feasibility stage, *International Journal of Marine Energy*, <http://dx.doi.org/10.1016/j.ijome.2013.05.008>
- [21] Sterman, J.D. & Booth Sweeney, L. (2002) Cloudy skies: Assessing public understanding of global warming, *System Dynamics Review* 18(2), pp207–240
- [22] Groesser, S. (2011) Projekte scheitern wegen dynamischer Komplexität: Qualitative Feedbackmodellierung zur Komplexitätsbewältigung, *Bern University of Applied Sciences*, [www.bfh.ch](http://www.bfh.ch) [10/03/2013]
- [23] Sterman, J.D. (1992) System dynamics modelling for project management, *Sloan School of Management, Massachusetts Institute of Technology, Cambridge*
- [24] Cooper, K. & Lee, G (2009) Managing the dynamics of projects and changes, *Proceedings of the International System Dynamics Conference*, Albuquerque
- [25] Sterman, J.D. (2010) Does formal system dynamics training improve people’s understanding of accumulation? *System Dynamics Review* 26(4), pp316–334
- [26] Senge, P. (1990) *The fifth discipline: The art and practice of the learning organization*, ISBN 978-0553456349, Crown Publishing Group, New York
- [27] Bucher, R. (2012) De-risking utility-scale marine energy investments by extending the regular project implementation by a competitive technology qualification routine, *Proceedings of the 4th International Conference on Ocean Energy*, Dublin, Ireland



**Journal of Energy Challenges  
and Mechanics**

ISSN 2056-9386

<http://www.nscj.co.uk/JECM/>

**Editor:**

Dr. Henry Tan  
University of Aberdeen, Scotland, United Kingdom

**Scope:**

Since James Watt, a Scottish inventor, improved efficiency of the steam engine, human civilization relies more and more on a steady supply of energy. Today we are at a transitional age. On the one hand, we see technology advances in the exploration and development of oil and gas, a depleting resource; we see growth in handling aging and decommissioning. On the other hand, we see ideas and plans for new energy infrastructure. This journal is about energy challenges and the underlying mechanics, involving multiple disciplines in science, technology, management and policy-making. Mechanics, fundamentally, is about force and the related behaviours, where force is about relationships, including those physical, human and social. For mechanics, the journal covers interactive boundaries with many other disciplines. For energy, topics include both fossil fuels and many different forms of renewable energy; also, issues related to energy economy, energy policy, efficiency, safety, environment and ecology will also be covered.



Cove Bay, Aberdeen, Scotland, United Kingdom